

國立交通大學

光電工程研究所

博士論文

低溫氧化物半導體及有機半導體之電晶體及感測器研究

Low Temperature Transistors and Sensors based on Oxide

Semiconductor and Organic Semiconductor Materials

研究生：蔡武衛

指導老師：冉曉雯 教授

中華民國一百年十一月

低溫氧化物半導體及有機半導體之電晶體及感測器研究

Low Temperature Transistors and Sensors based on Oxide

Semiconductor and Organic Semiconductor Materials

研究生：蔡武衛

Student : Wu-Wei Tsai

指導老師：冉曉雯

Advisor : Hsiao-Wen Zan

國立交通大學



Submitted to Institute of Electro-Optical Engineering

National Chiao Tung University

in partial Fulfillment of Requirements

for the Degree of

Doctor of Philosophy

in

Electro-Optical Engineering

November 2011

Hsinchu, Taiwan, Republic of China

中華民國一十年十一月

低溫氧化物半導體及有機半導體之電晶體及感測器研究

研究生：蔡武衛

指導教授：冉曉雯 博士

國立交通大學光電工程研究所

摘 要

軟性電子與顯示器的開發在近年來是新世代在電子領域之研究的重要方針，目前具有潛力的電晶體如有機半導體電晶體與無機氧化物半導體電晶體，兩者相較於傳統非晶矽(a-Si)電晶體元件有以下幾項優勢，如較低的製程成本及較低製程溫度(<200°C)，且易於大面積液態製程，所以近年來被許多專家學者廣泛的研究及探討。然而，後者的載子遷移率相較於前者具有更好的表現，所以在應用層面上較為廣泛如在高頻電路上等。

首先，在論文第二章節裡，提出一個簡易的製程技術，在元件的通道做處理，製作出許多的短通道，且利用電漿處理大幅提通道與通道間的載子濃度，進而改善元件的載子遷移率從 4 到約 $80 \text{ cm}^2 / \text{V s}$ 。相較於傳統的銦化鎵氧化物半導體，大多數的研究都是利用電漿處理元件的源極及汲極介面，以去降低元件的接觸電阻，進而提升元件的特性，且一般傳統的載子遷移率往往都是小於 $40 \text{ cm}^2 / \text{V s}$ ，除了一些研究團隊利用一些特殊的技術，如雙層的氧化物半導體層(IGZO/ITO)，或是利用高介電常數(Ta_2O_5)的絕緣層，去提升元件的載子遷移率為 $60\sim 100 \text{ cm}^2 / \text{V s}$ 。在此，我們的研究中也討論到奈米點摻雜的數量以及電漿處理的時間都會影響到元件的特性。由於元件目前製程尚未把元件封裝，且通道孔洞化的結構受到外界水、氧分子的影響使得元件的穩定性較差，未來我們會覆蓋保護層(passivation layer)於元件之通到處，且期望搭配一些規則陣列的圖案取代現有的製程技術，以達到元件的最佳特性。在本論文中，我們也討論到了有機光(章節三、四)和氣體感測器。此兩種光的偵測器，如光偵測器二極體及光偵測器電晶體，在章節三提到的光偵測器二極體中，我們首先發現，垂直式元件於垂直方向的載子遷移率會影響元件對光偵測的頻寬的大小，在此我們利用富勒烯(C_{60})當作光偵測器的受體(acceptor layer)，並改變元件在垂直方向的電洞之載子遷移率從 2.3×10^{-5} 到 $2.8 \times 10^{-4} \text{ cm}^2 / \text{Vs}$ ，可以提升元件偵測的頻寬從 10 到 80 MHz(元件的操作偏壓為 4 伏特)。本論文在第三章節有詳細的討論。另外，在章節四提到的垂直式光電晶體上，為了方便光載子的拆解，我們將我們現有的(p-type)垂直式電晶體中摻雜少許的(n-type)材料，且在照光下的反應，我們發現外部量子效率(EQE)可以提升至 360%在 620 奈米下。在此，我們推斷為元件在照光下屏蔽了基極的控制所以大幅提升 EQE，且本論文在第四章節有進一步的討論。最後，在氣體感測器上，在本論文第五章節裡有討論到利用水平式並五苯環

(pentacene)有機薄膜電晶體當作氨氣感測器，我們在此利用紫外光(UV)處理元件的絕緣層(PMMA)，為了去修飾絕緣層表面的形成氫氧官能基進而提升元件的反應靈敏度，且在有處裡的絕緣層最低可以偵測到的氨氣濃度為 0.5ppm。此偵測的範圍剛好可以判斷一般病人是否患有肝病(健康病人呼出的氨氣含量為 0.745ppm；肝硬化病人呼出的氨氣含量為 0.278ppm)。因此非侵入式有機電晶體當氣體感測器在未來電子產品的發展是相當具有潛力的。本論文最後章節為垂直式有機電晶體的開發，此項工作為本人與趙宇強博士、陳俊宇博士、姜鈞銘、姜淑玲、古明哲共同完成，垂直式有機電晶體相較於傳統的水平結構電晶體有幾項優勢：(1)可以不利用到黃光微影技術就能使通道長度縮至小於 1(微米)等級，(2)低的操作電壓，(3)高輸出電流。在此章節裡，我們有改變不同的半導體材料製作不同的空間電荷限制垂直式電晶體，並探討其工作原理與元件特性。在我們的研究之中，高分子垂直式電晶體具有較好的操作特性，如其操作電壓在為 1 伏特下最大輸出電流為 0.14 mA/cm^2 ，元件的開關比為 24310，電流增益為 10^4 個數量級，另外我們的半導體層也有嘗試利用蒸鍍的方式成膜，但得到的成果不盡理想，再本論文中會再加以討論其原因。



Low Temperature Transistors and Sensors based on Oxide Semiconductor and Organic Semiconductor

Materials

Student : Wu-Wei Tsai

Advisor : Dr. Hsiao-Wen Zan

Institute of Electro-Optical Engineering
National Chiao Tung University

ABSTRACT

The development of flexible electronics and displays are crucial for next generation electronics. Metal-oxide thin-film transistors (TFTs) and organic TFTs have higher potential than a-Si TFTs because of the following advantages : 1) low-cost; 2) solution fabrication process on a large area array system; 3) low fabrication temperature ($< 200\text{ }^{\circ}\text{C}$); and 4) the applications are on a flexible substrate.

In the **Chapter 2** of this dissertation, we proposed a high performance amorphous In-Ga-Zn-O (a-IGZO) thin film transistor with nano-dot doping (NDD). The nano dot structure creates many short channel and high concentration region in the channel region. Also, the performance of a-IGZO TFT can be controlled by the dots concentration and the Ar plasma treatment time. The proposed nano-dot doping reduces the effective channel length, lowers down the energy barrier, and enhances the effective field-effect mobility 19 times larger than that of the control sample without NDD. The proposed device is promising for the development of low-cost, lithography-free, and high-performance flexible electronics. In the **Chapter 3** and **Chapter 4** of the dissertation, we introduce the two organic photodetectors, including photodiode and phototransistor. In the **Chapter 3**, bilayered organic photo diodes with controllable carrier mobility in the p-type donor are demonstrated. Vertical carrier mobility of pentacene is demonstrated to be increased while the deposition rate is high. With C60 as the acceptor material and pentacene deposited at high deposition rate as donor material, the detection of 80-MHz signals is demonstrated. Using high mobility pentacene in stead of poly(3-hexylthiophene) (P3HT) to serve as the hole transport layer effectively improves the hole mobility over 1 orders and hence enlarges the operation bandwidth. The results enable the development of low-cost large-area organic image sheets for the detection of high-frequency signals. In the **Chapter 4**, we introduce a vertical polymer phototransistor with low operational voltage (-1.5 V). A blended polymer layer with both acceptor and donor materials was used as a

channel material in the vertical space-charge-limited transistor (SCLT). Under illumination, we obtained external quantum efficiency (EQE) as high as 360% at 620 nm. We propose the effects of base-field shielding as a means to explain high EQE. This proposition has been supported by two-dimensional simulation of the device. Moreover, we also study the pentacene-based organic thin film transistor (OTFT) as ammonia sensor in the **Chapter 5** of this dissertation. Non-invasive ammonia sensors are attractive alternatives for the diagnoses of a variety of chronic diseases such as liver cirrhosis and renal failure. A low cost pentacene-based organic thin film transistor (OTFT) fabricated by a novel and simple process was demonstrated to be highly sensitive and specific for ammonia gas. Various measurement parameters that reflected OTFT device characteristics for ammonia detection were investigated. Significant variations of the turn-on current, intrinsic mobility, and threshold voltage (V_{th}) were observed while subthreshold swing ($S.S.$) was almost unchanged to the alteration of ammonia concentration. The OTFT device detected 0.5~5 ppm concentration ammonia gas at room temperature, which is in the critical range that can distinguish between healthy person and patients with liver cirrhosis and renal failure. The sensitivity of the device was further enhanced following a simple UV irradiation treatment to modify the functional groups on poly(methyl methacrylate) (PMMA) dielectric layer. Possible interference for ammonia detection such as humidity effect and selectivity among nitrogen, alcohol, carbon dioxide, acetone, methane and ammonia were also examined. We concluded that the proposed pentacene-based OTFT is a promising device for the future application in non-invasive medical diagnoses. In the **Chapter 6** of this dissertation, an organic vertical transistor is investigated. In this work, I was cooperating with Dr. Yu-Chiang Chao, Dr. Chun-Yu Chen, Shu-Ling Jiang, Chun-Ming Chiang, and Ming-Che Ku. In the **Chapter 6**, the operation mechanism of vertical transistor is introduced. The turn-on current, on-off current ratio, current gain, and operation voltage of P3HT-based vertical transistor is 0.14 mA/cm², 24310, 10⁴, and 1 V. In order to improve the controllability and solve the accumulation of polystyrene spheres problems, the nano-imprint technology is used to replace the polystyrene spheres fabrication process and to form the grid structure.

Acknowledgement

能夠順利完成學業是令人開心的一件事情，碩博這五年多以來讓我學會了很多解決事情的能力，且這一路走來要感謝非常多人的幫助。首先，我要感謝我的指導老師冉曉雯老師，您處理事情的細心以及面對解決分析實驗上問題的能力，真是令我非常欽佩以及是需要學習的地方；也要感謝孟心飛老師、洪勝富老師、蔡娟娟老師在實驗上給予我很多的意見及支持，讓我的博士研究能夠更加的完整。另外要感謝實驗室學長國錫、志宏、育敏、文馨、光明、廷遠、皇維、德倫、睿志、芸嘉、宇強、士欽，給予我很多研究上的意見，且當我在面臨困難的時候，你們都很樂意幫助我開導我讓我度過種種難關，希望你們未來都會非常順遂。也要感謝當初一起修課努力的同學們，權陵、俊傑、志宇、旻君、和璵，謝謝你們讓我的學生生涯更加地多采多姿，也希望你們的工作能一切順利。此外要感謝當初與我一起熬夜打拼準備資格考試的伙伴，上傑、凌曉。還要感謝實驗室可愛的學弟妹們：感謝長紘，常常陪我一起聊天，祝你發表 Science 的夢想能夠實現；感謝鈞銘、淑玲、玉玫、明哲，當初一起努力打拼分享實驗心得，也恭喜你們都已順利畢業找到很好的工作；感謝家新，跟我一起努力奮鬥，讓我博士生涯畫下完美的句點，也希望你在海陸部隊一切都能夠順利、平安；感謝王辰、培修，你們的搞笑，真是實驗室的開心果；此外也希望認真的洪正、凱瑞、季遠、永軒、建豪、茂家等實驗室所有成員們，祝你們都能夠順利畢業。也感謝助理明嫵、欣鳳，幫忙處理實驗室大小事務，你們真的辛苦了，謝謝。也要謝謝我的女友蚊子，常常聽我訴說我的實驗上的甘苦談，有了妳的傾聽，也讓我減輕了很大的壓力，真是謝謝妳了。最後我要感謝我最親愛的父母，蔡日通先生、宋秋琴女士，給予我最大的支持，在我幾次挫折時，都能給我很大的力量讓我有勇氣繼續走下去，使得能夠成就今日的我，真是謝謝您們了。

Table of Contents

Chinese Abstract	I
English Abstract	III
Acknowledgement	V
Table of Contents	VI
List of Figures	IX
List of Tables	XIV

Chapter 1. Introduction	1
1.1. Overviews of Metal-Oxide Semiconductor	1
1.1.1. Fundamental Transport Mechanism of Metal-Oxide Semiconductor	2
1.1.2. Oxygen Vacancy on a-IGZO Films	3
1.1.3. Argon Plasma Treatment on a-IGZO Films	4
1.2. Overviews of Organic Semiconducting Materials	5
1.2.1. Polymers	6
1.2.2. Small molecular weight materials	9
1.3. Overviews of Organic Sensors	11
1.3.1. Organic Photodetector	11
1.3.2. Ammonia Sensors	14
1.4. Overviews of Organic Transistors	19
1.4.1. Organic Field-Effect Transistors	19
1.4.2. Organic Vertical Transistors	22

Chapter 2. Effective Mobility Enhancement by Using Nanometer Dot Doping in amorphous IGZO Thin-Film Transistors	37
2.1. Introduction	37
2.2. Experiment	38
2.2.1. Device Fabrication Process	38
2.3. Results and Discussions	43
2.3.1. The Resistivity Variation of a-IGZO Thin Film after Ar Plasma Treatment	43
2.3.2. The Influence of Ar Plasma Treatment Time on a-IGZO TFT	46
2.3.3. The Influence of Dots Concentration on a-IGZO TFT	49
2.3.4. The Plausible Mechanism of Increased Mobility	53
2.4. Conclusion	60

Chapter 3. Increasing Organic Vertical Carrier Mobility for the Application of High Speed Bilayered Organic Photodetector	64
3.1. Introduction	64
3.2. Experiment	65
3.2.1. Device Fabrication Process	65
3.2.2. Measurement Instrument.....	68
3.3. Results and Discussions	68
3.4. Conclusion.....	76
Chapter 4. Vertical Polymer Phototransistor featuring Photomultiplication due to Base-field Shielding	79
4.1. Introduction	79
4.2. Experiment	80
4.2.1. Device Fabrication process	80
4.2.2. Illumination System	85
4.3. Results and Discussions	86
4.4. Conclusion.....	97
Chapter 5. Pentacene-based Organic Thin Film Transistors for Ammonia Sensing	100
5.1. Introduction	100
5.2. Experiment	102
5.2.1. Device Fabrication Process	102
5.2.2. Gas Sensing System	104
5.3. Parameter Extraction	106
5.3.1. Field Effect Mobility.....	106
5.3.2. Threshold Voltage.....	107
5.3.3. Subthreshold Swing	107
5.4. Comparisons of Ammonia-Sensing Phenomenon in STD-OTFTs and UV-OTFTs.....	108
5.4.1. Electrical Properties of STD-OTFTs and UV-OTFTs.....	108
5.4.2. Gas Diffusion Model.....	110
5.4.3. Ammonia Concentration Effect	114
5.4.4. Sensing Phenomenon of UV-OTFTs	115
5.4.5. Selectivity of Gas Sensing	117

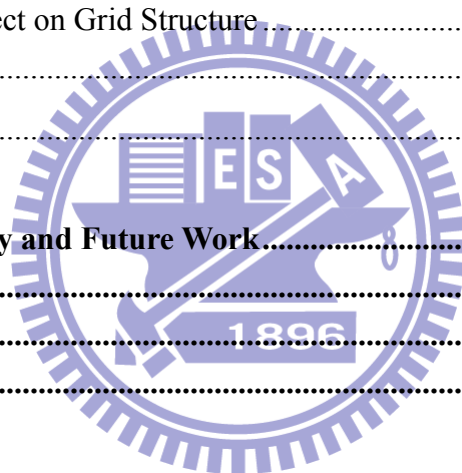
5.4.6. Phenomenon of Recovery	119
5.4.7. Humidity Effect.....	120
5.5. Conclusions	122

Chapter 6. Low Operated Polymer Vertical Transistors with High On/Off Current Ratio128

6.1. Introduction	128
6.2. Experiment	130
6.2.1. Device Fabrication Process	130
6.3. Result and Discussions	135
6.3.1. Dielectric Characteristics	135
6.3.2. Output Current Characteristics of SCLT	135
6.3.3. Operation Mechanism of SCLT	141
6.3.4. Morphology Effect on Grid Structure	146
6.4. Conclusion.....	147
6.5. Future Work.....	147

Chapter 7. Summary and Future Work.....154

Vita	160
Publication lists	161
Patents	164



List of Figures

1.1	The carrier transport paths in covalent semiconductors.....	2
1.2	The carrier transport paths in amorphous oxide semiconductors.	3
1.3	Molecular structure of widely used conjugated polymers.	8
1.4	Molecular structure of widely used small molecular weight materials.	10
1.5	The operation mechanism of photo diode.....	12
1.6	(a) The current density as a function of voltage ($J-V$), inset of Figure 1.7(a) is the device structure. (b) The frequency response of device.....	13
1.7	Schematic of the bottom-gate organic field-effect transistors with (a) top contact or (b) bottom contact structures. (c) Schematic diagram of a (c) top-gate with bottom contact transistor using a standard TFT device structures.	20
1.8	Molecular and crystallographic structures.....	22
2.1	The schematic device structures of (a) STD (standard) and (b) NDD (nano-dot doping) top gate (TG) a-IGZO TFTs.	39
2.2	The SEM image of the cross sectional view of the TG-NDD a-IGZO TFTs in the channel region.....	39
2.3	(a) The processes flow of the TG-NDD (top-gate with nano-dot doping) a-IGZO TFT. The SEM images of the PVP substrate adsorbed with (b) 0.2 wt % and (c) 0.8 wt % polystyrene spheres. The diameter of the sphere is 200 nm. By counting the PS spheres on SEM images in Figures 6.3(b) and 6.3(c), the concentration of dots per area is estimated to be $6.8 \times 10^6 \text{ mm}^{-2}$ for 0.8 wt % PS spheres and is $4.8 \times 10^6 \text{ mm}^{-2}$ for 0.2 wt % PS spheres, respectively.....	42
2.4	Resistivity of the a-IGZO thin film as a function of the Ar plasma exposure time.. ..	44
2.5	(a) and (b) are O_{1s} XPS spectra for IGZO without and with Ar plasma treatment films, respectively.. ..	45
2.6	The transfer characteristics of TG-STD devices with different Ar plasma treatment time on source/drain electrodes.. ..	47
2.7	The transfer characteristics of TG-NDD devices with high density dots (0.8 wt % PS spheres) with different Ar plasma treatment time.	48
2.8	The output characteristics of TG-NDD devices (PS spheres: 0.8 wt %) with the optimal Ar plasma treatment time (3 mins).	49
2.9	The transfer characteristics and the root square of the drain current plotted as a function of gate bias for three devices:.....	50
2.10	(a)The top view of device structure in the work and (b) top view of the device	

structure in reference 13.....	52
2.11 Effective field-effect electron mobility of this work and of other reports from 2006 to 2010.	52
2.12 The SEM images of different dots concentration.	54
2.13 The transfer characteristics of TG-NDD devices when we repeating the measurement for seven times.	56
2.14 The schematic device structures of (a) standard (STD) and (b) nano-dot doping (NDD) bottom gate (BG) a-IGZO TFTs. (c) Four typical parameters (threshold voltage, on/off ratio, mobility, and subthreshold swing) of BG-STD and BG-NDD devices are extracted and plotted as a function of Ar plasma treatment time.	58
3.1 Schematic device structure of the bilayered photodetector.....	66
3.2 The energy band diagrams of sample A and sample B under reverse voltage biases.	69
3.3 The incident photon-to-electron conversion efficiency of sample A and sample B under various reverse voltage biases.....	69
3.4 The absorption spectra of pentacene and P3HT. The thickness of pentacene and P3HT is 100 nm.	69
3.5 The current density–voltage characteristics of organic diodes with C60, P3HT, pentacene deposited at 0.1 Å/s, and pentacene deposited at 1 Å/s.	70
3.6 The electrical frequency responses of pentacene diodes and P3HT diode.....	71
3.7 The rectifier circuit	71
3.8 The frequency characteristics of PDs made by pentacene and P3HT.	72
3.9 The schematic measurement setup.....	73
3.10 AFM images of 100 nm, 1.5 nm, and 3 nm pentacene films deposited at (a) 0.1 Å/s and (b) 1 Å/s, (c) 0.1 Å/s and (d) 1 Å/s, and (e) 0.1 Å/s and (f) 1 Å/s on PEDOT:PSS covered ITO glass, respectively.	75
3.11 X-ray diffraction (XRD) pattern of pentacene deposited on ITO surface.	76
4.1 Schematic illustration of the structure of P3HT or P3HT:PCBM-SCLT.	80
4.2 The defined emitter pattern with the ITO electrode.....	81
4.3 The chemical structure of insulator (a) PVP (poly(4-vinylphenol)) cross-linked with (b) PMF (poly(melamine-co-formaldehyde) methylated).	82
4.4 The scanning electron microscopy (SEM) image when the PS is removed by the tape.....	83
4.5 The PVP at sites without Al coverage were removed through plasma treatment of 150 W O ₂ for 13 min to open the channel region.	83
4.6 The chemical structure of (a) Polythiophene (P3HT) and (b) Phenyl-C61-butyric acid methyl ester(PCBM).	84
4.7 The processes flow of device fabrication.....	85

4.8	The illumination system and the vertical transistor. The organic active layer is P3HT or P3HT:PCBM. The thickness of the active layer is 350-nm.	86
4.9	(a) Output characteristics of P3HT SCLT. The V_{CE} is sweep from 0 to - 3V and the V_{BE} is step from - 0.9 to 1.5 V. (b) The on/off current ratio of the P3HT SCLT.	86
4.10	Transfer characteristics of a P3HT-SCLT in total darkness and under illumination. The light intensity is from 0 to 11 mW/cm ²	87
4.11	A simulated potential distribution at the central vertical channel.	88
4.12	The 2-dimensional electron distribution of P3HT-SCLT with a photo generation rate = 10 ¹⁰ cm ⁻³ and a V_{BE} = 2 V. Electron concentration is denoted by n	89
4.13	(a) Output characteristics of P3HT:PCBM (1 : 0.1) (wt : wt) SCLT. The V_{CE} is sweep from 0 to - 3V and the V_{BE} is step from - 0.9 to 1.5 V. (b) The on/off current ratio of the P3HT:PCBM (1 : 0.1) (wt : wt) SCLT.	90
4.14	(a) Output characteristics of P3HT:PCBM (1 : 0.5) (wt : wt) SCLT. The V_{CE} is sweep from 0 to - 3V and the V_{BE} is step from - 0.9 to 1.5 V. (b) The on/off current ratio of the P3HT:PCBM (1 : 0.5) (wt : wt) SCLT.	90
4.15	Transfer characteristics of a P3HT:PCBM SCLT in total darkness and under illumination. The light intensity is from 0 to 11 mW/cm ²	91
4.16	The off current density of P3HT:PCBM-SCLT as a function of collector to emitter voltage.	93
4.17	The J_{ph} of planar diode of P3HT:PCBM=1:0.1 (Diode-A), planar diode of P3HT:PCBM=1:1 (Diode-B), and EC diode in P3HT:PCBM-SCLT(P3HT:PCBM=1:0.1) plotted as a function of bias voltage..	94
4.18	The EQE of P3HT:PCBM-SCLT. The V_{BE} is fixed at 1.5 V.	95
4.19	The (a) EQE of P3HT/PCBM SCLT and (b) EQE of device EC diode as a function of frequency response.....	96
4.20	Off current density of P3HT:PCBM SCLT monitored under pulsed illumination of 1 Hz frequency.....	97
5.1	Device structure of (a) STD-OTFT and (b) UV-OTFT.	103
5.2	(a) The flowchart for the fabrication processes and (b) for the measurement characterization.	104
5.3	The gas sensing system.....	105
5.4	The transfer characteristics of STD and UV-OTFTs.....	108
5.5	Energy-band diagram of (a) STD-OTFTs and (b) UV-OTFTs.	109
5.6	The AFM images of pentacene film deposited on PMMA and UV-treated PMMA, respectively.	110
5.7	The transfer characteristics of (a) STD-OTFTs and (b) UV-OTFTs under 1 ppm NH ₃ condition with period time of 500 sec.	111
5.8	Ammonia sensing responses of OTFTs with multi-parameters.....	112

5.9	When ammonia molecules diffuse into the active layer through grain boundaries, the decrease in mobility may result from the increase of scattering centers or the increase of energy barrier for charge transport.....	113
5.10	The hole-traps, which were attributed to the NH_3 or NH_4^+ near dielectric interface and caused lower concentration of gate-induced mobile carriers.....	114
5.11	Concentration dependent ammonia sensing response.....	115
5.12	Concentration dependent ammonia sensing response.....	117
5.13	Target dependent OTFT responses.	118
5.14	Recovery dependent ammonia sensing response. Mobility variation of (a) STD-OTFTs and (b) UV-OTFTs as a function of sensing time.....	119
5.15	Recovery dependent ammonia sensing response. Threshold voltage shifted of (a) STD-OTFTs and (b) UV-OTFTs as a function of sensing time.....	120
5.16	Humidity effect on ammonia sensing using UV-OTFTs..	122
6.1	Schematic device structures. (a) Vertical transistor with rough source metal [8]. (b) Vertical transistor with thin or porous base metal [9],[10]. (c) Vertical transistor which named as “SCLT”.....	129
6.2	The structure of the proposed vertical transistor.....	130
6.3	The process flow of the vertical transistor.....	130
6.4	(a) The structure of polystyrene spheres.(b) The polystyrene spheres on the Au film surface.(c) The polystyrene spheres are removed by an adhesive tape (Scotch, 3M) without damage to the metal. (d) The gold surface without the boiling IPA treatment. (from ref. 15).....	133
6.5	(a) The characteristics of silicon oxide with Polystyrene Spheres. (b) The characteristics of silicon oxide without Polystyrene Spheres.....	135
6.6	The electric characteristics of the P3HT-based SCLT with various grid voltages applied.....	136
6.7	The electric characteristics of the P3HT-based SCLT in double logarithmic scale with fixed V_G	137
6.8	The electric characteristics of the Pentacene-based SCLT with various grid voltages applied..	138
6.9	The electric characteristics of the Pentacene-based SCLT in double logarithmic scale with fixed V_G	139
6.10	The electric characteristics of the C60-based SCLT with various grid voltages applied. The Al electrode is commonly grounded and the Au collector is positive biased at V_C with respect to Au. The collector current I_C means the electrons are collected by the Au collector.....	140
6.11	The electric characteristics of the C60-based SCLT in double logarithmic scale with fixed V_G	141

6.12	(a) The device structure near one opening of polymer SCLT. Position A is at the center of the opening, while position B is near the grid. (b) The potential profile along the emitter–collector path through the opening when V_C is fixed at a negative value. (x), (y), (z) are the potential profile along the path for various conditions. (c) The schematic current–voltage curve of EC diode with the structure Au/P-type/Al. The path through position A in on or off state are denote as A^{ON} or A^{OFF} in the diode IV curve.....	143
6.13	(a) The device structure near one opening of polymer SCLT. Position A is at the center of the opening, while position B is near the grid. (b) The potential profile along the emitter–collector path through the opening when V_C is fixed at a positive value. (x), (y), (z) are the potential profile along the path for various conditions. (c) The schematic current–voltage curve of EC diode with the structure Au/C60/Al. The path through position A in on or off state are denote as A^{ON} or A^{OFF} in the diode IV curve.....	145
6.14	Current density – voltage curves for emitter–collector diodes made by P3HT, pentacene, and C60.	146
6.15	AFM images of (a) pentacene, (b) C60, and (c) P3HT above grid structure. The dimension of these images is $3\mu\text{m}\times 3\mu\text{m}$	147
6.16	The process flow of SCLT by nano-imprint technology.....	148
6.17	The process for developing the PDMS mold.	148
6.18	The (a) top view and (b) cross sectional view SEM images of the sample after nano-imprint.....	149
6.19	The different plasma etching conditions of cross sectional view SEM images.	150
6.20	(a), (b), (c) shows the cross sectional view SEM images of different wet etching conditions of sample. (d) is the sample cross sectional view SEM images after plasma etching.....	151
7.1	Context for Chapter 2.....	155
7.2	Context for Chapter 3.....	156
7.3	Context for Chapter 4.....	157
7.4	Context for Chapter 5.....	158
7.5	Context for Chapter 6.....	159

List of Tables

1.1 Diseases associated with unusual breath odors.....	15
1.2 The gas concentration with different healthy conditions	16
1.3 This table compares the ammonia sensors of this work and of others reports.....	19
1.4 Comparison of different types vertical transistors.	25
2.1 Comparisons of typical parameters in TG-STD and TG-NDD a-IGZO TFTs.	50
2.2 The intrinsic mobility of a-IGZO with 0.2 and 0.8 wt% nano dot doping.....	54
2.3 Typical parameters of BG-NDD TFTs with and without nano-dot doping.	59
6.1 Typical parameters of vertical transistors.	146



Chapter 1. Introduction

1.1. Overviews of Metal-Oxide Semiconductor

Thin-film transistors (TFTs) based on metal-oxide semiconductors were considered a promising candidate for next generation semiconductors [1]. With a high mobility ($> 10 \text{ cm}^2/\text{Vs}$) and a low subthreshold swing (0.2 V/decade) under low fabrication process, a-IGZO semiconductors have received considerable attention because of the applications on liquid-crystal displays, electrophoretic displays, and organic light-emitting diode displays [2,3]. In addition, the large band gap of the a-IGZO semiconductor ($>3 \text{ eV}$) results in high transparency, insensitivity to natural light, and transparency in visible region ($\lambda = 400\text{-}700 \text{ nm}$) [4,5]. Moreover, the carrier concentration of a-IGZO film can be controlled by modulating oxygen ratio, process power, and pressure. Radio-frequency sputtering, which enables deposition of thin films with high-melting-temperature materials over large areas at low substrate temperatures, is one of the methods used to deposit a-IGZO films [6].

Hosono et al. proposed that the chemical species and/or a structure in a thin film are unstable when thin films are deposited at low temperatures [6][7]. The chemical species and/or a structure are frozen in the as-deposited thin film, which relaxes to a more stable state and provides the atoms with more energy to rearrange after thermal annealing, leading to a desirable change in the electron transport properties [6][7]. Most oxide TFTs, especially a-IGZO TFTs, are fabricated by using physical vapor deposition (PVD) techniques at room temperature and often require a high temperature ($> 300 \text{ }^\circ\text{C}$) post-deposition thermal annealing process to obtain high-performance and high-stability TFTs [8][9].

1.1.1. Fundamental Transport Mechanism of Metal-Oxide Semiconductor

The a-Si:H material composed of covalent bonds of sp^3 orbital is shown in **Figure 1.1** [10]. The electronic levels and trap states were influenced by the fluctuation of the bonding angle in the a-Si:H structure [11]. By contrast, conduction band minimums (CBM) of oxides are composed of spherically extended orbitals of metals, and their overlaps with neighboring metal orbitals (s orbital) are not considerably altered by disordered amorphous structures; therefore, electronic levels of CBM are insensitive to local strained bonds, and electron transport is not considerably affected (**Figure 1.2**). Therefore, a-IGZO exhibits high mobility, even in an amorphous structure [10].

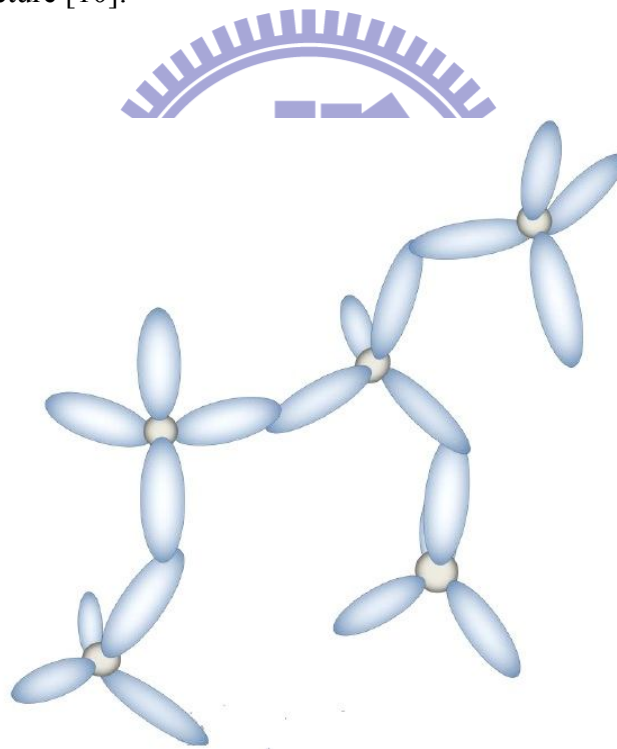


Figure 1.1 The carrier transport paths in covalent semiconductors.

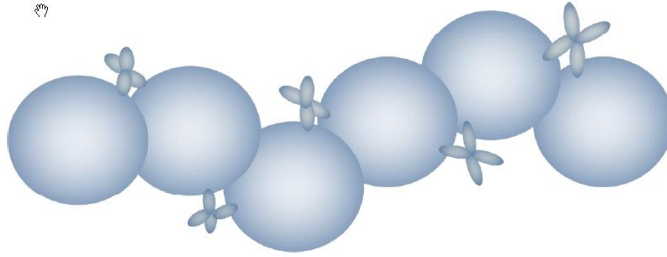


Figure 1.2 The carrier transport paths in amorphous oxide semiconductors.

Each element in a-IGZO film exhibits various characteristics that affect the performance of TFTs. A high In concentration is expected to obtain high electron concentration [11] because the element of In is a large atom that easily loses electrons. The released electron from In may move to the conduction band when the composition of a-IGZO lacks oxygen [12]. Ga was chosen because the atomic radius of Ga is close to In. Hosono et al. reported that the Ga^{3+} in the a-IGZO film attracts oxygen tightly because of the high ionic potential resulting from the small ionic radius and +3 valence. It suppresses the electron injection and induces the oxygen ions escaping from the a-IGZO film, providing relatively high stability for the device. [13]. Compared to the carrier concentration in the material of a-IZO ($\sim 10^{21} \text{ cm}^{-3}$), a lower carrier concentration of a-IGZO ($\sim 10^{19} \text{ cm}^{-3}$) was observed [13][14]. However, incorporation of Ga decreases carrier density and mobility. The largest mobility of $39 \text{ cm}^2/\text{Vs}$ was obtained for Zn-doped In O (a-IZO). However, it is difficult to control and maintain a low carrier density, which is necessary for efficient TFT operation for Ga-free or Ga-poor films. Therefore, the incorporation of Ga is crucial to obtain stable films and TFTs. The element of Zn in the a-IGZO film was reported to affect the crystallization of thin film. The crystalline structure was reported when the ratio of the Zn atoms in the a-IGZO film was higher than 65% [12]. The crystalline structure in a-IGZO film may degrade the electrical characteristic when uniformity is decreased by the disorder grain boundaries.

1.1.2. Oxygen Vacancy on a-IGZO Films

The oxygen vacancy formation process is closely related to the generation of charge carriers, according to (1).



In (1), O_2 is lost from the oxide sub-lattice (O_o^x) to create a doubly charged oxygen vacancy (V_o^\bullet) and two free electrons. It is assumed that IGZO films attained more charge carriers because of thermally enhanced or energy-activated oxygen vacancy formation processes. It was reported that the mobility of a-IGZO films depends on the carrier concentration because the carrier transport is governed by percolation conduction over trap states and is enhanced at high carrier concentrations by filling the trap states [10].

The chemical and oxygen binding energy of O_{1s} were analyzed by X-ray photoelectron spectroscopy (XPS) to understand the oxygen vacancy in a-IGZO films. This analytical method was used to investigate the origin of carriers in IGZO. By Gaussian fitting, these O_{1s} peaks were divided into three peaks, centered at approximately 530.5, 531.5, and 532.5 eV. The peak with the lower energy value of 530.5 eV represents O^{2-} ions combined with Zn, Ga, and In ions in the IGZO compound system. This indicates the stoichiometric ratio between the metal cations and oxygen anions. The medium binding energy value at 531.5 eV is associated with O^{2-} ions that are in oxygen vacancy regions within the IGZO films. Therefore, the change in the intensity of this peak may be connected to a variation in the concentration of oxygen vacancy. The higher binding energy value of 532.5 eV is related to loosely bonded oxygen on the IGZO surface, including absorbed H_2O , CO_3 , and O_2 . The peak may be eliminated completely when the film is annealed or slightly etched by plasma treatment; therefore, it is considered inconsequential [15].

1.1.3. Argon Plasma Treatment on a-IGZO Films

The influence of Ar plasma treatment on a-IGZO thin films was investigated. The net electron carrier concentration (10^{20} – 10^{21} cm⁻³) of the a-IGZO thin films considerably increased after exposure to the Ar plasma compared to that (10^{14} cm⁻³) of the as-deposited thin film. Furthermore, sheet resistivity considerably decreased after Ar plasma treatment lasting several seconds. Energetic Ar ion bombardment during plasma treatment induces the preferential sputtering of the relatively light atoms from the surfaces of II-VI or III-V group semiconductors because of the physical momentum transfer between the ions in the plasma and the atoms on the material surface. Therefore, the substantial change in electron concentration after exposure to the Ar plasma may be caused by the oxygen deficiency on the a-IGZO film surface [16].

1.2. Overviews of Organic Semiconducting Materials

In recent years, flexible display has been one of great interest especially in mobile applications. However, flexible substrates cannot sustain under high temperature fabrication process, the development of low temperature process of electronics is necessary. Organic semiconducting materials have high potential due to the following advantages: 1) low-cost; 2) solution fabrication process on a large area array system; 3) low fabrication temperature (< 200 °C); and 4) the applications are on a flexible substrate.

Recently, organic materials are extensively applied on electronic devices, such as light emitting diode(LED), thin film transistors(TFT), solar cells, and sensors. Also, organic chemical products are closely related to our life, such as foods, medicines, paper, plastics, and fibers. There are two kinds of organic semiconducting materials such as polymer and small molecular weight materials. We introduce these two kinds

of organic materials as following.

1.2.1. Polymers

The conventional polymer is extensively used due to their plastic deformability, mechanical strength, low weight, and usually high resistivity. In 1970, the Japanese chemist Shirakawa found that it was possible to synthesize polyacetylene $(CH)_n$ in a new way. Shirakawa synthesized *trans*-polyacetylene by accidentally adding “a thousand-fold too much catalyst” to the reaction vessel. Shirakawa was stimulated by this discovery. The corresponding reaction at another temperature gave a copper-colored film instead, and it appeared to consist of almost pure *cis*-polyacetylene. Around the same time chemist Alan G. MacDiarmid and physicist Alan J. Heeger were experimenting with a metallic-looking film of the inorganic polymer sulphur nitride, $(SN)_x$. When MacDiarmid heard about Shirakawa's discovery at a seminar in Tokyo, he invited Shirakawa to the University of Pennsylvania in Philadelphia. After Shirakawa and MacDiarmid modified polyacetylene by oxidation with iodine vapor, they knew that the optical properties changed in the oxidation process and asked Heeger to have a look at the films. After measured the conductivity of the iodine-doped *trans*-polyacetylene, the incredible increase of ten million times the original conductivity was discovered. In the summer of 1977, Alan Heeger, Alan MacDiarmid and Hideki Shirakawa, and co-workers, published their discovery in the article "Synthesis of electrically conducting organic polymers: Halogen derivatives of polyacetylene $(CH)_n$ " in The Journal of Chemical Society, Chemical Communications.[17] The discovery was considered a major breakthrough, and Alan Heeger *et al.* have been awarded the Nobel Prize in Chemistry in the year 2000 for showing how plastic can be made to conduct electric current.[18] Since the field has grown immensely, and also given rise to many new and exciting applications. The

properties of a polymer are strongly related to the physical arrangement of monomers along the backbone of the chain. Polymers which contain only one type of monomer are known as homopolymers, while polymers containing a mixture of monomers are known as copolymers.

The conducting conjugated polymer consists of a long chain of carbon atoms with alternating single and double bonds between them, each with one hydrogen atom. The structure of polyacetylene is shown in **Figure 1.3(a)** as a typical example. Polyacetylene is usually prepared in the cis- form which can be converted into the thermodynamically more stable trans- form by thermal isomerization. Other semiconducting conjugated polymers shown in **Figure 1.3** are commonly used in organic light-emitting diodes (OLEDs), organic field-effect transistors (FETs), and organic solar cells. As shown in **Figure 1.3(b)**, PEDOT:PSS is a water-soluble transparent conducting polymer, which enabled the fabrication of all plastic polymer light-emitting diodes (PLEDs). PEDOT:PSS can be used as a transparent anode. Currently, it serves as the hole transport layer to develop PLEDs for commercial products. Structures of PPV and PPV derivatives (MEH-PPV) are shown in **Figure 1.3(f)** and **1.3(h)**. The most commonly used PPV is typically deposited by spin coating a precursor polymer, and then thermal treatment is used to convert the precursor to PPV. PPV also used as hosts for low gap emitter.[19] PFO is also the material used in the blue PLEDs as shown in **Figure 1.3(g)**. Following the first blue PFO-based PLED was developed in 1991 [20], efforts was conducted on developing commercially viable devices based on these polymer. Polythiophenes and P3HT-based PLEDs and FETs are widely studied.[21], [22] Due to it relatively low gap, the polythiophenes are red emitters. However, the relatively poor lifetime of polythiophene-based PLEDs inhibits their commercialization. On the other hand, P3HT is a commonly used material in FETs. Under proper treatment, the mobility can

be increased and the performance of the FETs can be optimized.

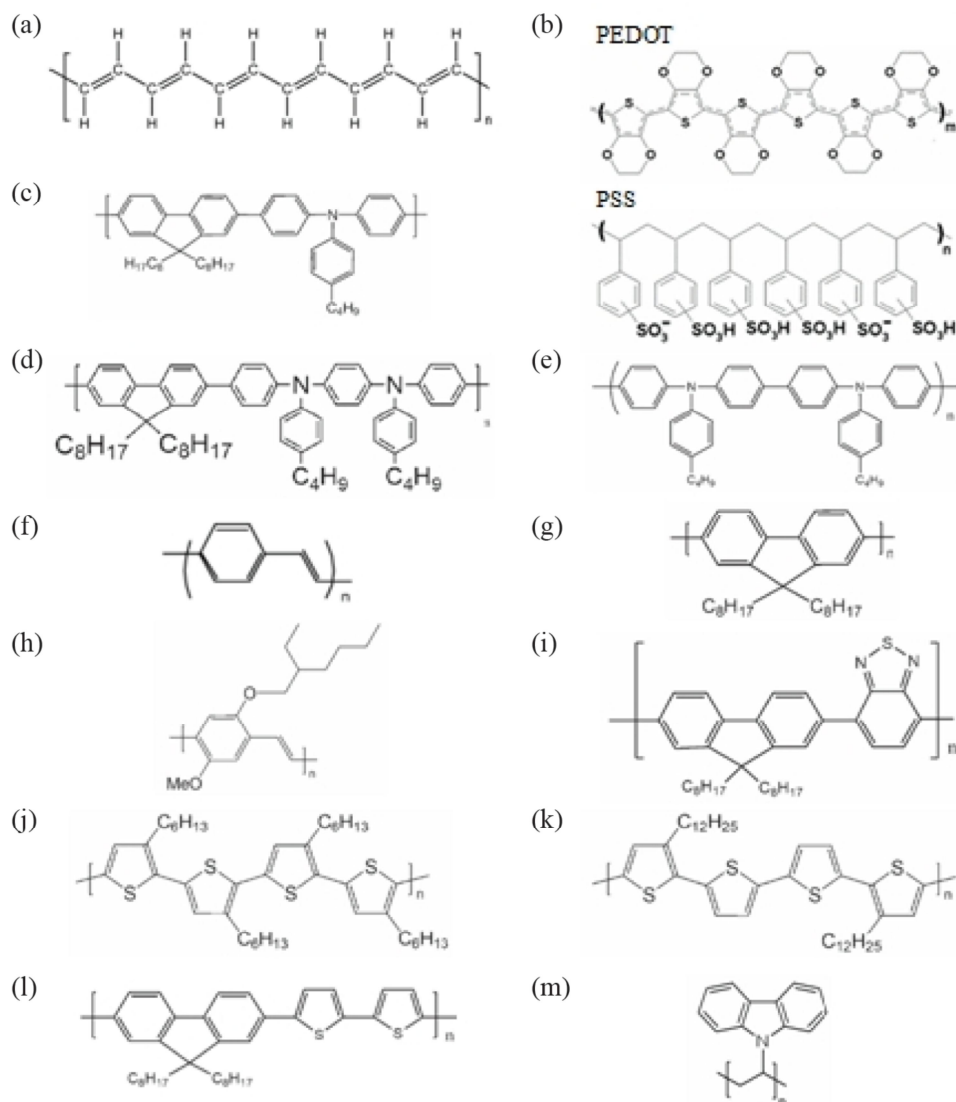


Figure 1.3 Molecular structure of widely used conjugated polymers: (a) polyacetylene; (b) poly(3,4-ethylenedioxythiophene) : poly(styrenesulfonate) (PEDOT:PSS); (c) poly(9,9-dioctylfluorene-co-N-(4-butylphenyl)diphenylamine) (TFB); (d) poly(9,9-dioctylfluorene-co-bis-N,N-(4-butylphenyl)-bis-N,N-phenyl-1,4-phenylenediamine) (PFB); (e) poly[N,N'-bis(4-butylphenyl)-N,N'-bis(phenyl)-benzidine] (polyTPD); (f) poly(p-phenylenevinylene) (PPV); (g) poly[9,9-dioctylfluorenyl-2,7-diyl] (PFO); (h) poly-[2-methoxy,(5-2'-ethyl-hexyloxy)-p-phenylenevinylene] (MEH-PPV); (i) poly(9,9-dioctylfluorene-co-benzothiadiazole) (F8BT); (j) poly[3-hexylthiophene] (P3HT); (k) poly[5,5'-bis(3-alkyl-2-thienyl)-2,2'-bithiophene] (PQT); (l) poly[(9,9-dioctylfluorene-co-bithiophene] (F8T2); (m)

poly(9-vinylcarbazole) (PVK).

1.2.2. Small molecular weight materials

The phenomenon of organic electroluminescence was first discovered by Pope in 1963.[23] However, the development of organic light-emitting diode actually began in the late 1970s by Tang and his coworkers. Their research led eventually to the discovery of the first efficient multi-layered organic electroluminescent device.[24] Since then, tremendous progress has been made in the field of organic electroluminescence. Among all efforts to improve the performance of organic light-emitting diode, the continuing discovery of new and improved electroluminescent materials is the most essential one. Small molecular weight materials consist of molecules with several to a few hundred atoms. Small molecular weight materials were the initial focus of physicists and engineers who seeking to understand the optoelectronics properties of organic materials. Structure of some small molecular weight materials are shown in **Figure 1.4**. **Figure 1.4(a)** shows the structure of CuPC which is widely used as an hole transport layer. However, depending on the other layer, it may inhibit hole injection [25] or enhance it [26]. TPD is another material commonly used as hole transport layer as shown in **Figure 1.4(b)**. But, its relatively low glass transition temperature around 65°C causes a failure of OLED as TPD recrystallized. The recrystallization may be suppressed by adding guest molecule such as rubrene. However, it may result in red electroluminescence from rubrene. Hence, NPB is developed with a structure similar to TPD but the methylphenyl groups are replaced by naphthylphenyls. The modification significantly enhances the stability of the OLED due to the increased glass transition temperature around 95°C.

Alq3 is the most widely used electron-transport and host emitting material in

OLEDs. It is still one of the most robust electron-transport backing layers in OLED, particularly with the help of the hole blocking layer to trap the hole carriers from injecting into Alq3.[27] It is not only commonly used as a green emitter, but also as a host for lower-gap emitter guest molecules. It has been found by the time-of-flight technique that the drift mobility of electrons in Alq3 is increased by about two orders of magnitude (to $10^{-4} \text{ cm}^2/\text{Vs}$) as the deposition rate decreased from 0.7 to 0.2 nm/s.

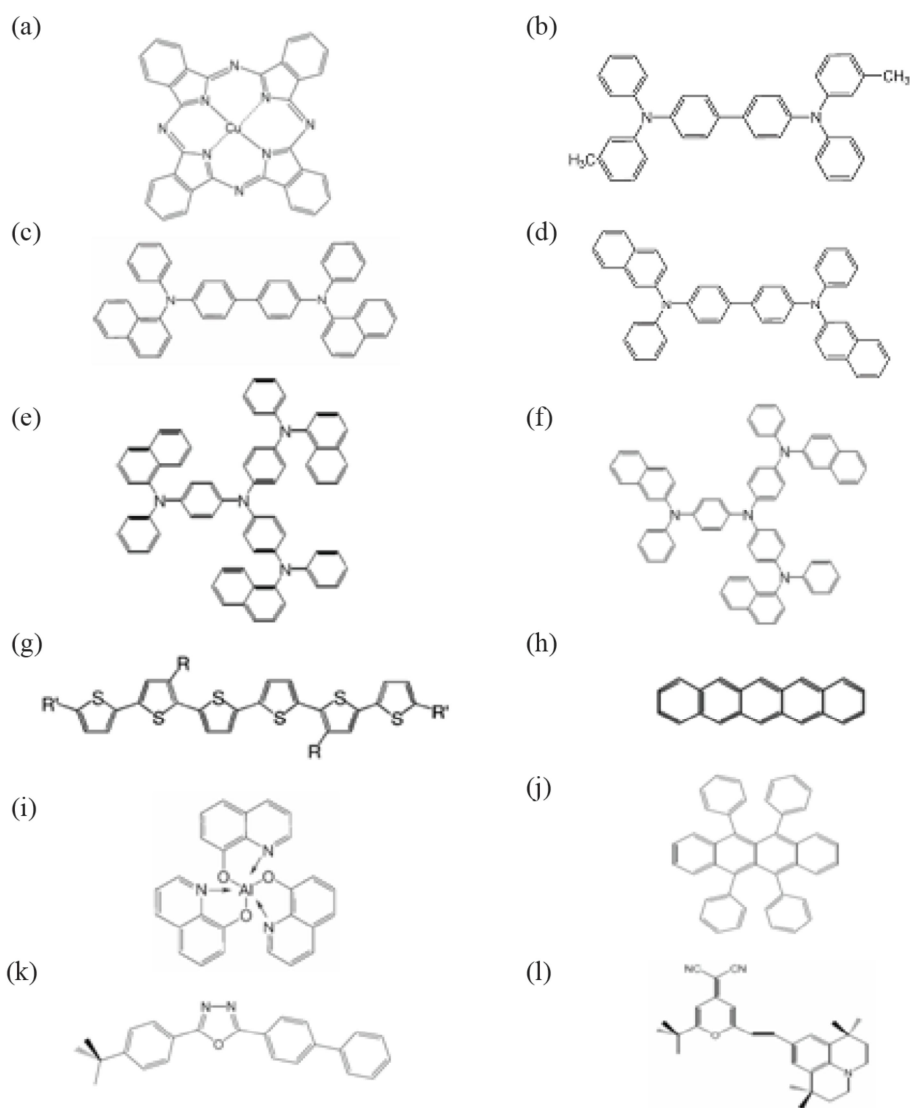


Figure 1.4 Molecular structure of widely used small molecular weight materials: (a) copper phthalocyanine (CuPC); (b) N,N'-Bis(3-methylphenyl)-N,N'-bis(phenyl)-benzidine (TPD); (c) N,N-bis(1-naphthalenyl)-N,N'-bis(phenyl)benzidine (α -NPB);

(d) N,N'-bis(2-naphthalenyl)-N,N'-bis(phenylbenzidine) (β -NPB); (e) 4,4',4''-Tris(N-(1-naphthyl)-N-phenyl-amino)triphenylamine (1T-NATA); (f) 4,4',4''-Tris(N-(2-naphthyl)-N-phenyl-amino)triphenylamine (2T-NATA); (g) α -sexthiophene (α -6T); (h) Pentacene; (i) Tris(8-hydroxyquinoline) Aluminum (Alq3T); (j) (5,6,11,12)-Tetraphenylnaphthacene (Rubrene); (k) 2-(4-Biphenyl)-5-(4-tert-butylphenyl)-1,3,4-oxadiazole (PBD); (l) 4-(Dicyanomethylene)-2-tert-butyl-6-(1,1,7,7-tetramethyljulolidin-4-yl-vinyl)-4H-pyran (DCJTb).

1.3. Overviews of Organic Sensors

1.3.1. Organic Photodetector

Organic electronics have attracted considerable interest because of their low fabrication temperature on a variety of low-cost flexible substrates, which enables the development of organic photonic integrated circuits, organic sensor arrays, organic photocouplers, or organic imaging sheets. The two main organic photodetectors used currently are as follows: (1) organic photodiode (OPD) and (2) organic phototransistor (OPT). The mechanism and the characteristics of these two photodetectors are discussed in the following paragraphs.

1.3.1.1. Organic photodiode

According to the research of organic photodiodes and solar cells, the light is mainly adsorbed by the organic materials and generates the high binding energy of excitons. The high binding energy of excitons causes difficulty in dissociating the electrons and holes. In **Figure 1.5**, the photodetector is through the dissociation of photogenerated excitons at the interface between donor-like materials and an acceptor-like material under reversed bias. The performance of an OPD is determined by the efficiency of charge generation and charge transport.

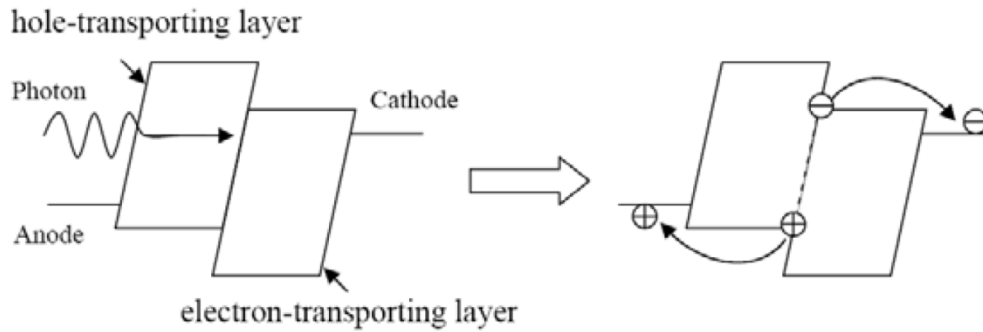


Figure 1.5 The operation mechanism of photo diode.

The quantum efficiency of an OPD can be enhanced by creating a bulk-heterojunction, and the charge transport property can be improved by using high mobility materials. Increasing the interfaces of the hole transporting layer and electron transporting layer with a blending system (for example, P3HT:PCBM) was proposed to enhance the external quantum efficiency (EQE). However, the blending system may decrease the frequency response of photodiodes because of the increasing recombination rate. The bilayered system may be used to decrease the recombination rate of electrons and holes to increase frequency response. Forrest et al. (2000) proposed the highest operation frequency (~ 430 MHz) of organic multilayer OPDs by using ultrahigh-vacuum (1×10^{-10} torr) organic molecular beam deposition to control the thickness of an individual layer as 0.5 nm, to enable carrier tunneling [28]. The device structure and the J - V curve are shown in **Figure 1.6(a)**, and the photoresponse is shown in **Figure 1.6(b)**.

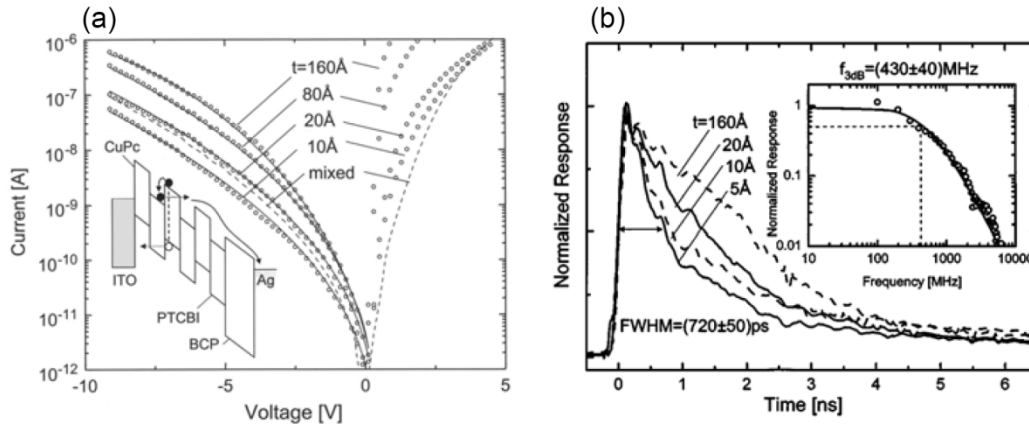


Figure 1.6 (a) The current density as a function of voltage (J - V), inset of Figure 1.7(a) is the device structure. (b) The frequency response of device.

When a conventional high vacuum (5×10^{-7} to 1×10^{-6} Torr) deposition system was used, a multilayered PD was reported to exhibit a bandwidth from a few kilohertz to a few megahertz under an operation voltage of 1–5 V, and demonstrated a small incident photon to current conversion efficiency IPCE of 0.02% [29]. Morimune et al. used a bilayered structure to demonstrate a bandwidth of 70 MHz under 7 V operation, with the peak IPCE at approximately 7% [30]. High frequency responses were demonstrated in these studies; however, factors associated with organic materials to influence frequency response were not discussed. In Chapter 3, we propose an adjustment of the vertical mobility to influence the frequency response and obtain an ultrahigh response of 80 MHz.

1.3.1.2. Organic phototransistor

Compared to OPD, the OPT exhibits a higher photoresponsivity because of the threshold voltage shift after exposure to light, and it may be used on flexible substrates and integrated with a circuit.

In organic semiconducting materials of phototransistors, pentacene is one of the most popular materials because of the high mobility ($\sim 1\text{-}5\text{ cm}^2/\text{Vs}$) and air stability. The

field-effect mobility and the threshold voltage varied, and the pentacene-based phototransistor was exposed to light [31]. This occurred because the photo penetrated to the interface between the active layer and dielectric, and generated the extra electron and hole pairs to contribute the photo current. In addition, after exposing to light for a specific period, the generated electron may induce negative traps and cause a threshold voltage shift. In previous research [32], threshold voltage largely shifted when the device was exposed to light with positive gate voltage, and led to the increased photoresponsivity of the device. The increased photoresponsivity occurred because the generated electron by exaction may attract through the positive voltage, and the electron was limited in the channel to form the traps. By contrast, the generated hole by excitons may extract from the channel and decrease the recombination rate. In addition, it was proposed that the electron trap induced by a photo has a lengthy life time; however, it may recover quickly by applying the positive voltage [33]. OPTs have high photoresponsivity; however, the frequency response is considerably slow because the reaction includes the trap generation, that is, the capture and release of carriers.

1.3.2. Ammonia Sensors

1.3.2.1. Applications of Ammonia Sensors

Ammonia is a crucial compound. It can be used in several fields, such as chemical industries, fertilizer factories, refrigeration systems, food processing, fire power plants, and medical diagnoses. The variation in ammonia concentration is crucial for these applications. For example, in chemical industries, ammonia concentration is related to the quality of fertilizers and frozen foods. Additionally, ammonia concentration plays a vital role in medical diagnoses. **Table 1** shows the component of human breath volatile organic compounds (VOCs) related to a number of diseases. It indicates that

ammonia is a disease marker for uremia, liver cirrhosis, and renal failure [34][35][36][37].

Table 1.1 Diseases associated with unusual breath odors.

Breath component as a disease marker	Diseases	References
Acetone	Diabetes; Lung cancer	[34], [35]
Ammonia	Uremia; Chronic liver disease	[36], [37]
Butyric acid	Liver cirrhosis	[37]
Ethanethiol	Liver cirrhosis	[37]
Hydrogen sulfide	Periodontal disease	[37]

Table 2 shows the gas concentration with various healthy conditions [36][38] [39]. The breath ammonia concentration of patients is 1-5 ppm for renal failure, and 0.5-1 ppm for liver cirrhosis.

The common method used for diagnosis is an examination of the ammonia concentration in blood. Recently, developments of a noninvasive diagnostic method have received considerable attention. The breath of patients can be detected easily and traced by the gas sensor if a noninvasive, inexpensive, portable, and disposable diagnostic device is developed.

Table 1.2 The gas concentration with different healthy conditions

	Renal failure	Liver cirrhosis	Diabetes	References
Ammonia	4.8 ppm	0.5-1 ppm		[36], [38]
Acetone			5-300 ppm	[39]

1.3.2.2. Different Types of Ammonia Sensors

(a) Metal-oxide gas sensors

ZnO[40], iridium oxide [41], molybdenum oxide [42], polyaniline [43][44][45], polypyrrole [46], Au and MoO₃-modified WO₃ [47][48], and Pt- and SiO₂-doped SnO₂ [49] are commonly used materials for ammonia gas sensing. When the device is exposed to analytes, the gas removes some of the adsorbed oxygen and modulates the height of the potential barriers, thereby changing the conductivity and creating the sensor signal. However, ammonia sensors based on metal oxide must be operated at high temperature (over 300 °C), and are not useful as noninvasive ammonia sensors.

(b) Catalytic ammonia sensors

The reaction of a catalytic ammonia sensor is based on a metal layer with ammonia gas. The reaction causes a change in electrode potential and charge carrier concentration, which can be quantified by using a field-effect device, such as a capacitor or a transistor [50][51].

(c) Conducting polymer gas detectors

Conducting polymer ammonia gas detectors used polymers, such as polypyrrole or polyaniline, to react with ammonia. During this process, ammonia can reversibly reduce the oxidized form of polymer. Because the reduction in the polymer film

causes a change in the conductivity of material, it can be used for resistometric or amperometric ammonia detection [52]. However, the irreversible reaction between ammonia and the polymer causes the sensitivity of the sensor to decrease when exposed to ammonia.

(d) Optical gas analyzers

Two optical methods are used for the detection of ammonia. The first method is the Berthelot reaction, which uses a coloration reaction of ammonia with phenol and hypochlorite in aqueous solutions [53][54]. The disadvantage of this method is the slow kinetics of the reaction. The detection limit is approximately 5 μM of ammonia in water or 90 ppb. The second method is optical absorption ammonia detection [55]. A spectrum of the light influenced by the gas composition can be obtained by using a laser and a spectrograph. Although the method is sensitive and selective for ammonia sensing, the equipment is expensive and is unsuitable for miniaturized ammonia sensors.

1.3.2.3. OTFTs Ammonia Gas Sensors

Research on OTFT sensors began in the late 1980s, after the first OTFTs were proposed. Such sensors offer the advantages of simple process, low fabrication cost, remarkable response repeatability [56], and selectivity [57][58]. Because several types of organic molecules exhibit sensing behavior based on their chemical compositions, sensibility and selectivity can be pursued by choosing chemically or biologically functionalized semiconducting polymer active layers for the use of OTFTs in compact sensing systems or in biochips [56][59][60][61]. In addition, [59] and [62] verified that the OFET sensor exhibited superior performance than a similar resistor-type sensor for drift, sensitivity, signal-to-noise ratio, response time, life time, and

operating temperature. In particular, OTFTs were proposed as multi-parameter sensors [63]. A fingerprint of each gas can be obtained by measuring the parameters of field-induced conductivity, threshold voltage, and field-effect mobility. This enables the transistors to be more selective than conventional chemiresistors. The morphology of the active layer plays a crucial role in the sensibility of OTFT sensors. The device response increases when the grain size is reduced [64]. The effect of a channel length compared to the grain size was also observed. Nanoscale organic transistors were explored to improve the limit of detection [65].

The active layer of OTFT sensors currently include substituted thiophene polymers, oligomers, naphthalenes, copper-phthalocyanine, and pentacene. These devices were exposed to various analytes, such as alcohols, ketones, thiols, nitriles, and ester and ring compounds. However, research on ammonia sensors with OTFTs is limited. Our study is the first to demonstrate the pentacene-based OTFTs as ammonia gas sensors.

Finally, **Table 3** shows a comparison of the ammonia sensors proposed in this study and those of other studies [66][67][68][69][70][71][72]. Currently, only optical sensing systems exhibit a sensitivity in parts-per-billion (ppb) or even parts-per-trillion (ppt) regime. Electrical ammonia sensors, such as poly(3-hexylthiophene)(P3HT)-based OTFT, exhibit sensitivity higher than 10 ppm. Electrical sensors based on catalytic metals exhibit sensitivity of 1 ppm; however, the sensors must be operated at a temperature higher than 150 °C. Our proposed pentacene-based OTFT, particularly the UV-treated pentacene-based OTFT, exhibited sensitivity of 0.5 ppm at room temperature.

Table 1.3 This table compares the ammonia sensors of this work and of others reports

Principle	Low detection limit	Response time	Temperature range	Remarks[ref.]
Optical gas sensors /Nessler	90 ppb	~1 min	37°C	To detect in water[66]
Optical gas sensors /Coulometric	1 ppt	~5 min	N/A	Expensive setup[67]
Optical gas sensors /Absorption spectroscopy	1 ppb	~5 min	N/A	Expensive setup[68]
Catalytic metal / Palladium	1 ppm	~1 min	Up to 600°C	Low selectivity[69]
Catalytic metal / Polyaniline	1 ppm	~1 min	Up to 150°C	Irreversible reactions [70], [71]
OTFT/P3HT	10 ppm	2~3 min	RT	Low sensitivity[72]
Our proposed / pentacene-based OTFT	0.5 ppm	~ 500 sec	RT	Low cost and high sensitivity

1.4. Overviews of Organic Transistors

1.4.1. Organic Field-Effect Transistors

The beginning of the electronics was marked by cathode ray tube, vacuum rectifier, and vacuum-tube triode. The triode, includes a grid between the anode and the cathode, transformed communication and long-distance telephone come true. However, the vacuum-tube d the rectifier into an amplifier, and made the radio triode was fragile, slow, and difficult to miniaturize.

Replacing the triode with a solid-state device offering an alternative to the thermionic principle is thus a good idea for solving problems of triode. This concept was successfully demonstrated with Bardeen and Brattain's point-contact transistor and Shockley's bipolar transistor. After material technology research for more than forty

years, the performance of metal-oxide-semiconductor field-effect transistor (MOSFET) is optimized. Today, MOSFETs dominated almost every electronic device. Recently, organic field-effect transistors (OFETs) based on solution-processed polymeric as well as small molecular semiconductors have obtained impressive improvements in their performance. Even an all polymer transistor has been reported. [73] Initially, the interest in organic transistors remained limited due to the poor performance of these initial devices. Several review papers and books describing the materials, operating principles, and fabrication processes have been published for comprehensive understanding. ([74], [75])

Organic field-effect transistors have been developed to realize low-cost, large-area electronic devices. OFETs have been developed with various device geometries as depicted in **Figure 1.7**. The most commonly used device geometry is bottom gate with top contact because of using thermally grown Si/SiO₂ oxide as gate dielectric. Devices based on glass substrate are also demonstrated for possible integration with organic light-emitting diodes.

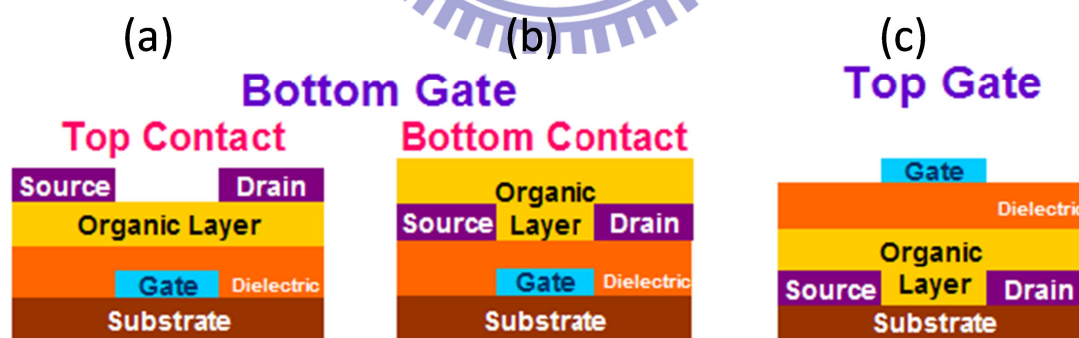


Figure 1.7 Schematic of the bottom-gate organic field-effect transistors with (a) top contact or (b) bottom contact structures. (c) Schematic diagram of a (c) top-gate with bottom contact transistor using a standard TFT device structures.

Carrier mobilities in organic semiconductors are limited by the hopping process between the molecules in disordered regions of the material. Many research works have examined the effects of modifying molecular parameters (regioregularity[76],

molecular weight [77], and side-chain length [78]) and processing conditions (film thickness [79], doping level [80], thermal annealing [81], and the film-forming method [82]). Studies of semiconductor/insulator interface phenomena (such as surface-mediated molecular ordering, surface dipoles, semiconductor alignment using self-assembled monolayers (SAMs), physical treatment, and photoalignment) are also receiving attention for enhancing the electrical properties of organic semiconductors. SAMs are highly ordered, two-dimensional structures that form spontaneously on a variety of surfaces. Tuning of the interfacial surface can be achieved by varying the rigidity, length, and terminal functional group of the molecule, which in turn affects the uniformity, packing, conformation, polarity, and charge density of the surface. Fluorene copolymers and polythiophenes have a relatively rigid backbone with attached alkyl chains for solubility, and are able to crystallize. Charge transport is fastest in the conjugation direction as shown in **Figure 1.8(a)**. [83] When chains pack, the π -orbitals belonging to different polymer chains are stacked co-facially, and this partial overlap between π -orbitals assists inter chain charge transfer. However, in another direction, the insulating alkyl chains impede charge transport so that mobility in this direction is the lowest. Such anisotropy has been experimentally verified by comparing the electrical characteristics of TFTs and diodes. Because of this pronounced anisotropy, texture and relative orientation of crystallites are expected to play an crucial role in controlling the electrical properties of these materials.

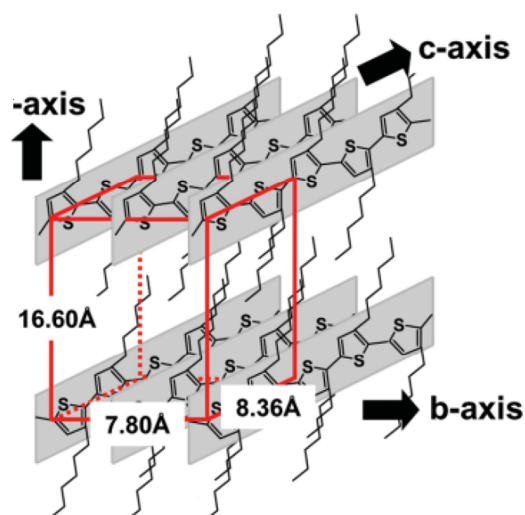


Figure 1.8 Molecular and crystallographic structures (orthorhombic unit cell) of P3HT chains show the enhanced π - π overlap along the b direction. [83]

1.4.2. Organic Vertical Transistors

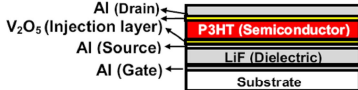
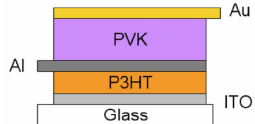
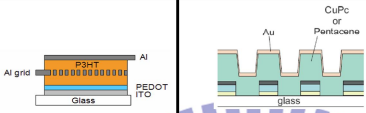
An explosion of interests in flexible electronics made from organic semiconductors gave rise to extensive research on organic light-emitting diodes (OLED), organic field-effect transistors (OFET), organic chemical sensors, and organic solar cells. One of the key components of the flexible electronics is the organic FET, a horizontal device with source and drain electrodes on the same plane. Its operating voltage usually over 25 V due to low carrier mobility and long channel length. The characteristics of organic FETs can be strengthened by increasing the mobility [83], utilizing a self-assemble monolayer as gate dielectrics [85] and reducing the channel lengths to the submicron [86]. Horizontal organic FETs with submicron channel lengths made by electron-beam lithography [87], nanoimprint lithography [88] and soft contact lamination [89] have been demonstrated. Vertical organic FETs, whose channel length was determined by the thickness of an insulating layer between source and drain, have been made by solid-state embossing [90], excimer laser [91] and photolithography [92]. However, the inherently low mobility as well as the incompatibility between conventional submicron lithography and

organic materials create great limitation on the device performance and the fabrication process for organic FET. The unique advantages of organic materials such as low-cost and large-area solution process are so far not fully explored for high-performance FET. Vertical non-field-effect transistors with multilayer structures give another route to circumvent the limits of both horizontal and vertical field-effect transistors. In vertical non-field-effect transistors, the channel length can be easily defined by the total thickness of the organic layers, and the current is modulated by a conductive layer embedded in the organic materials. Various device operating principles were proposed with different types of conductive layers such as a thin metal film[93], a strip-type metal film[94], a mesh gate electrode[95], and a porous conducting polymer network[96]. The remaining problems are the low current density, low on/off ratio as well as the complex fabrication process. One promising direction is to turn a vacuum tube triode into a solid-state device with current limited by the space-charge-limited current. Here, the vertical transistor is called “space-charge-limited transistor.” The operation mechanism of the SCLT can be understood as the quadratic space charge limited current between the emitter and the opening modulated by the grid potential. As in vacuum tube, the potential at the center of the opening is a linear combination of grid and collector potential $kV_G + V_C$, the factor k depends on the device geometry and increases with the ratio between the opening diameter and the grid-collector distance. The SCLC between the emitter and the opening is therefore approximately $C\varepsilon\mu (\lambda V_G + V_C)^2 / L^3$, where ε is the polymer dielectric constant and L is the emitter-grid distance. If the potential across the opening were uniform, the factor C would be the standard SCLC value of 9/8. The overall effect of non-uniform potential in our case can be absorbed into a numerical factor C. Because of the higher electric field the space between the grid and the collector does not limit the collector current,

therefore the emitter-opening current given above is actually the output current.

Table 1.4 shows the different types of vertical transistors and classified three types: (1) vertical organic field-effect transistor, VOFET (Y Yang *et al.*) [97], (2) hot carrier transistor, HCT (H. F. Meng *et al.*) [98] and metal-base transistor, MBT (I. A. Hümmelge) [99] (3) space-charge limited transistor, SCLT (H. F. Meng *et al.*) [100] and static induced transistor, SIT (Kudo *et al.*) [101]. Most of the devices are operated at low voltage (<5 V) with high output current density (>10 mA/cm²). For the first type transistor (VOFET), the transistor can obtain high on/off current ratio due to the transistor is operated at normally-off mode. However, it is difficult to develop for large area because it needs to deposit thin charge injection layer (2.5 nm) between source electrode and organic layer for improving the gate controllability. Also, the uniformity of the thin charge injection layer is difficult to control. The operation mechanism of second type transistor (HCT or MBT) is similar to BJT, the output current have saturation region. However, the carriers have to tunnel from base metal to collector, therefore, the film thickness of base metal have to be well controlled. For the third type transistor (SCLT or SIT), it does not need to deposit ultra-thin base metal due to the porous base structure. However, the low on/off current ratio and high leakage current are needed to solve. In the chapter 6, we proposed a new structure of vertical transistor and successfully solved these two issues.

Table 1.4 Comparison of different types vertical transistors.

Research group (device)	The device structure	Merit and shortcoming	Ref.
Y. Yang (VOFET)	 <p style="text-align: center;">VOFET</p>	<ul style="list-style-type: none"> ✓ On/off ratio: $\sim 10^3$ or 10^4 ✓ Operation voltage = 5 V ✗ Thin charge injection layer (2.5 nm) is used. 	[97]
H. F. Meng(HCT) I. M. Chan (HCT) I. A. Hümmelgen (MBT)	 <p style="text-align: center;">HCT or MBT</p>	<ul style="list-style-type: none"> ✓ On/off ratio: $\sim 10^2$ or 10^3 ✓ Operation voltage = 5 V ✓ High current gain ✗ Thin base metal is needed to enable tunneling. 	[98], [99]
H. F. Meng (SCLT) K. Kudo and M. Nakamura (SIT)	 <p style="text-align: center;">SCLT SIT</p>	<ul style="list-style-type: none"> ✓ On/off ratio: < 500 ✓ Operation voltage = 4 V ✓ High current gain ✗ High off current limits the on/off ratio. 	[100], [101]

Reference

- [1] M. Orita, H. Ohta, M. Hirano, S. Narushima, H. Hosono, "Amorphous transparent conductive oxide $\text{InGaO}_3(\text{ZnO})_m$ ($m \leq 4$): a Zn 4s conductor" *Philosophical magazine B*, 81, 501, (2001).
- [2] H. Yabuta, M. Sano, K. Abe, T. Aiba, T. Den, H. Kumomi, K. Nomura, T. Kamiya, H. Hosono, "High-mobility thin-film transistor with amorphous InGaZnO channel fabricated by room temperature rf-magnetron sputtering" *Appl. Phys. Lett.* 89, 112123, (2006).
- [3] A. Tsukazaki, A. Ohtomo, T. Onuma, M. Ohtani, T. Makino, M. Sumiya, K. Ohtani, S. F. Chichibu, S. Fuke, Y. Segawa, "Repeated temperature modulation epitaxy for p-type doping and light-emitting diode based on ZnO" *Nature Mater.*, 4, 42, (2005).

- [4] Y. Sun and J. A. Rogers, "Inorganic semiconductors for flexible electronics" *Adv. Mater.*, 19, 1897, (2007).
- [5] D. Y. Ku, I. H. Kim, I. Lee, K. S. Lee, T. S. Lee, J. H. Jeong, B. Cheong, Y.J. Baik, W. M. Kim, "Structural and electrical properties of sputtered indium-zinc oxide thin films" *Thin Solid Films* 515,1516, (2006).
- [6] H. Kumomi, K. Nomura, T. Kamiya, and H. Hosono, "Amorphous oxide channel TFTs" *Thin Solid Films* 516, 1516, (2008).
- [7] H. Hosono, K. Nomura, Y. Ogo, T. Uruga, and T. Kamiya, "Factors controlling electron transport properties in transparent amorphous oxide semiconductors" *J. Non-Cryst. Solids* 354, 2796, (2008).
- [8] W.B. Jackson, R.L. Hoffman, G. S. Herman, "High-performance flexible zinc tin oxide field-effect transistors" *Appl. Phys. Lett.* 87, 193503, (2005).
- [9] P. Görrn, M. Sander, J. Meyer, M. Kröger, E. Becker, H.-H. Johannes, W. Kowalsky, T. Riedl, "Towards See-Through Displays: Fully Transparent Thin-Film Transistors Driving Transparent Organic Light-Emitting Diodes" *Adv. Mater.* 18, 738, (2006).
- [10] K. Nomura, H. Ohta, Takagi, T. Kamiya, M. Hirano, H. Hosono, "Room-temperature fabrication of transparent flexible thin-film transistors using amorphous oxide semiconductors" *Nature*, 432, 488, (2004).
- [11] T. Iwasaki, N. Itagaki, T. Den, H. Kumomi, K. Nomura, T. Kamiya, and H. Hosono, "Combinatorial approach to thin-film transistors using multicomponent semiconductor channels: An application to amorphous oxide semiconductors in In-Ga-Zn-O system" *Appl. Phys. Lett.* 90, 242114 (2007).
- [12] H. Hosono, "Ionic amorphous oxide semiconductors: Material design, carrier transport, and device application" *J. Non-Cryst. Solids* 352, 851, (2006).
- [13] H. C. Pan, M. H. Shiao, C. Y. Su, and C. N. Hsiao, "Influence of sputtering

parameter on the optical and electrical properties of zinc-doped indium oxide thin films” *J. Vac. Sci. Technol.* 23, 1187, (2005).

[14] W. Lim, D. P. Norton, J. H. Jang, V. Craciun, S. J. Pearton, and F. Ren, “Carrier concentration dependence of Ti/Au specific contact resistance on n-type amorphous indium zinc oxide thin films” *Appl. Phys. Lett.* 92, 122102, (2008).

[15] S. Jeong, Y.-G. Ha, J. Moon, A. Facchetti, and T.J. Marks, “Role of Gallium Doping in Dramatically Lowering Amorphous-Oxide Processing Temperatures for Solution-Derived Indium Zinc Oxide Thin-Film Transistors” *Adv. Mater.* 22, 1346-1350, (2010).

[16] J. S. Park, J. K. Jeong, Y. G. Mo, H. D. Kim, S. I. Kim, “Improvements in the device characteristics of amorphous indium gallium zinc oxide thin-film transistors by Ar plasma treatment” *Appl. Phys. Lett.* 90, 262106. (2007).

[17] H. Shirakawa, E. J. Louis, A. G. MacDiarmid, C. K. Chiang and A. J. Heeger, “Synthesis of electrically conducting organic polymers: halogen derivatives of polyacetylene, $(CH)_x$ ” *J. Chem. Soc., Chem. Commun.*, Vol. 1977, pp. 578-580, (1977).

[18] [http://nobelprize.org/nobel_prizes/chemistry/laureates\(2000\)](http://nobelprize.org/nobel_prizes/chemistry/laureates(2000))

[19] R. H. Friend, R. W. Gymer, A. B. Holmes, J. H. Burroughes, R. N. Marks, C. Taliani, D. D. C. Bradley, D. A. Dos Santos, J. L. Bredas, M. Logdlund, W. R. Salaneck, “Electroluminescence in conjugated polymers” *Nature*, Vol. 397, pp. 121-128, (1999).

[20] Y. Ohmori, M. Uchida, K. Muro, and K. Yoshino, “Blue Electroluminescent Diodes Utilizing Poly(alkylfluorene)” *Jpn. J. Appl. Phys.*, Vol. 30, pp. L1941-L1943, (1991).

[21] D. Braun, G. Gustafsson, D. McBranch, and A. J. Heeger, “Electroluminescence and electrical transport in poly (3-octylthiophene) diodes” *J. Appl. Phys.*, Vol. 72,

pp. 564-568, (1992).

- [22] K. Sethuraman, S. Ochiai, K. Kojima, and T. Mizutani, "Performance of poly (3-hexylthiophene) organic field-effect transistors on cross-linked poly (4-vinyl phenol) dielectric layer and solvent effects" *Appl. Phys. Lett.*, Vol. 92, pp. 183302, (2008).
- [23] M. Pope, H. P. Kallmann, and P. Magnante, "Electroluminescence in organic crystals" *J. Chem. Phys.*, Vol. 38, pp. 2042-2043, (1963).
- [24] C. W. Tang and S. A. Vanslyke, "Organic electroluminescent diodes" *Appl. Phys. Lett.*, Vol. 51, pp. 913-915, (1987).
- [25] H. Aziz, Z. D. Popovic, N.X. Hu, A.M. Hor, and G. Xu, "Degradation Mechanism of Small Molecule-Based Organic Light-Emitting Devices" *Science*, Vol. 283, pp. 1900-1902, (1999).
- [26] W. L. Yu, J. Pei, Y. Cao, and W. Huang, "Hole-injection enhancement by copper phthalocyanine (CuPc) in blue polymer light-emitting diodes" *J. Appl. Phys.*, Vol. 89, pp. 2343-2350, (2001).
- [27] Y. Hamada, N. Matsusue, H. Kanno, H. Fujii, T. Tsujioka, and H. Takahashi, "Improved luminous efficiency of organic light-emitting diodes by carrier trapping dopants" *Jpn. J. Appl. Phys.*, Vol. 40, pp. L753-L755, (2001).
- [28] P. Peumans, V. Bulovic, and S. R. Forrest, "Efficient high-bandwidth organic multilayer photodetectors" *Appl. Phys. Lett.* 76, 3855, (2000).
- [29] M. Kaneko, T. Taneda, T. Tsukagawa, H. Kajii, and Y. Ohmori, "Organic Electroluminescent Diode Fabricated on Indium-Tin-Oxide-Coated Polyimide Substrate as an Electro-optical Conversion Device for Polymeric Waveguides" *Jpn. J. Appl. Phys.* 42, 2523 (2003).
- [30] T. Morimune, H. Kajii, and Y. Ohmori, "Photoresponse Properties of a High-Speed Organic Photodetector Based on Copper-Phthalocyanine Under Red

Light Illumination” *IEEE Photonic Tech. Lett.* 18, 2662 (2006).

- [31] M. Debucquoy, S. Verlaak, S. Steudel, K. Myny, J. Genoe, and P. Heremans, “Correlation between bias stress instability and phototransistor operation of pentacene thin-film transistors” *Appl. Phys. Lett.* 91, 103508, (2007).
- [32] Y. Guo, C. Du, C.A. Di, J. Zheng, X. Sun, Y. Wen, L. Zhang, C. Wu, G. Yu, and Y. Liu, “Field dependent and high light sensitive organic phototransistors based on linear asymmetric organic semiconductor” *Appl. Phys. Lett.* 94, 143303, (2009).
- [33] D. Knipp, R.A. Street, A. Volkel, and J. Ho, “Pentacene thin film transistors on inorganic dielectrics: Morphology, structural properties, and electronic transport” *J. Appl. Phys.* 93, 347, (2003).
- [34] S. E. Ebeler, A. J. Clifford, and T. Shibamo, “Quantitative analysis by gas chromatography of volatile carbonyl compounds in expired air from mice and human” *J. of Chromatography B.* 702, 211. (1997).
- [35] C. Grote and J. Pawliszyn, “Solid-phase microextraction for the analysis of human breath” *Anal. Chem.* 69, 587. (1997).
- [36] S. Davies, P. Spanel, and D. Smith, “Quantitative analysis of ammonia on the breath of patients in end-stage renal failure” *Kidney International*, 52, 223. (1997).
- [37] A. Manolis, “The diagnostic potential of breath analysis” *Clin.Chem.*, 29, 5. (1983).
- [38] C. Shimamoto, I. Hirata and K. Katsu, “Closure of an esophageal perforation due to fish bone ingestion by endoscopic clip application” *Hepato-Gastroenterol.* 47, 443. (2000).
- [39] Q. Zhang, P. Wang, J. Li and X. Gao, “Diagnosis of diabetes by image detection of breath using gas-sensitive laps” *Biosens.Bioelectron.* 15, 249. (2000).

- [40] G. S. Trivikrama Rao, and D. Tarakarama Rao, "Gas sensitivity of ZnO based thick film sensor to NH₃ at room temperature" *Sens. Actuators B: Chem.* 55, 166-169 (1999).
- [41] A. Karthigeyan, R. P. Gupta, K. Scharnagl, M. Burgmair, S. K. Sharma, I. Eisele, "A room temperature HSGFET ammonia sensor based on iridium oxide thin film" *Sens. Actuators B* 85, 145-153 (2002).
- [42] D. Mutschall, K. Holzner, E. Obermeier, "Sputtered molybdenum oxide thin films for NH₃ detection" *Sens. Actuators B: Chem.* 36, 320-324 (1996).
- [43] K. P. Kakde, D. J. Shirale, H. J. Kharat, P. D. Gaikwad, P. A. Savale, V. K. Gade, M. D. Shirsat, "Optimization of process parameters of chemically synthesized Polyaniline films for Ammonia gas sensing" *Proceedings of NSPTS-II*, C 17 1-5 (2006).
- [44] A. L. Kukla, Y. M. Shirshov, S. A. Piletsky, "Ammonia sensors based on sensitive polyaniline films," *Sens. Actuators B: Chem.* 37, 135-140 (1996).
- [45] V. V. Chabukswar, S. Pethkar, A. A. Athawale, "Acrylic acid doped polyaniline as an ammonia sensor" *Sens. Actuators B: Chem.* 77, 657-663 (2001).
- [46] I. Lahdesmaki, A. Lewenstam, A. Ivaska, "A polypyrrole-based amperometric ammonia sensor" *Talanta* 43, 125-134 (1996).
- [47] X. Wang, N. Miura, N. Yamazoe, "Study of WO₃-based sensing materials for NH₃ and NO detection" *Sens. Actuators B: Chem.* 66, 74-76 (2000).
- [48] C. N. Xu, N. Miura, Y. Ishida, K. Matuda, N. Yamazoe, "Selective detection of NH₃ over NO in combustion exhausts by using Au and MoO₃ doubly promoted WO₃ element" *Sens. Actuators B: Chem.* 65, 163-165 (2000).
- [49] Y. Wang, X. Wu, Q. Su, Y. Lee, Z. Zhou, "Ammonia-sensing characteristics of Pt and SiO₂ doped SnO₂ materials" *Solid-state Electron.* 45, 347-350 (2001).

- [50] F. Winqvist, A. Spetz, I. Lundstrom, "Determination of urea with an ammonia gas-sensitive semiconductor device in combination with urease" *Anal. Chim. Acta.* 164, 127-138 (1984).
- [51] I. Lundstrom, A. Spetz, F. Winqvist, U. Ackelid, H. Sundgren, "Catalytic metals and field-effect devices--a useful combination" *Sens. Actuators B: Chem.* 1 p.p 15-20 (1990).
- [52] E. Palmqvist, C. Berggren Kriz, K. Svanberg, M. Khayyami, D. Kriz, "DC-resistometric urea sensitive device utilizing a conducting polymer film for the gas-phase detection of ammonia" *Biosens. Bioelectron.* 10, 283-287 (1995).
- [53] M. P. E. Berthelot, *Repertoire Chimique Appliquee* 284 (1859).
- [54] P. L. Saerle, "The berthelot or indophenol reaction and its use in the analytical chemistry of nitrogen. A review" *Analyst* 109, 549-568 (1984).
- [55] G. H. Mount, B. Rumberg, J. Havig, B. Lamb, H. Westberg, D. Yonge, K. Johnson, R. Kincaid, "Measurement of atmospheric ammonia at a dairy using differential optical absorption spectroscopy in the mid-ultraviolet" *Atmos. Environ.* 36 (11), 1799-1810 (2002).
- [56] B. Crone, A. Dodabalapur, A. Gelperin, L. Torsi, H. E. Katz, A. J. Lovinger, Z. Bao, "Electronic sensing of vapors with organic transistors" *Appl. Phys. Lett.* 78, 2229-2231 (2001).
- [57] M. C. Tanese, L. Torsi, N. Cioffi, D. Colangiuli, G. M. Farinola, F. Babudri, F. Naso, M. M. Giangregorio, L. A. Zotti, L. Sabbatini, P. G. Zambonin, "Poly (phenyleneethynylene) polymers bearing glucose substituents as promising active layers in enantioselective chemiresistors" *Sens. Actuators B: Chem.* 100, 17-21 (2004).
- [58] D. Fine, D.F. Cauble, T. Jung, H. V. Seggern, M. Krische, A. Dodabalapur, "Organic FET Chemical Sensors with Small Molecule Receptors" *APS Meeting*

(2003).

- [59] T. Someya, H. E. Katz, A. Gelperin, A. J. Lovinger, A. Dodabalapur, "Vapor sensing with α , ω -dihexylquarterthiophene field-effect transistors: The role of grain boundaries" *Appl. Phys. Lett.* 81, 3079-3081 (2002).
- [60] L. Torsi, M. C. Tanese, N. Cioffi, M. C. Gallazzi, L. Sabbatini, P. G. Zambonin, G. Raos, S. V. Meille, M. M. Giangregorio, "Side-chain role in chemically sensing conducting polymer field-effect transistors" *J. Phys. Chem. B* 107, 7589-7594 (2003).
- [61] Z. T. Zhu, J. T. Mason, R. Diechkermann, G. Malliaras, "Humidity sensors based on pentacene thin-film transistors" *Appl. Phys. Lett.* 81, 4643-4645 (2002).
- [62] T. Someya, T. Sekitani, S. Iba, Y. Kato, H. Kawaguchi, T. Sakurai, "A large-area, flexible pressure sensor matrix with organic field-effect transistors for artificial skin applications," *Proc. Natl. Sci. USA* 101, 9966-9970 (2004).
- [63] L. Torsi, A. Dodabalapur, L. Sabbatini, P. G. Zambonin, "Multi-parameter gas sensors based on organic thin-film-transistors" *Sens. Actuators B: Chem.* 67, 312-316 (2000).
- [64] L. Torsi, A. J. Lovinger, B. Crone, T. Someya, A. Dodabalapur, H. E. Katz, A. Gelperin, "Correlation between oligothiophene thin film transistor morphology and vapor responses" *J. Phys. Chem. B* 106, 12.563-12.568 (2002).
- [65] L. Wang, D. Fine, A. Dodabalapur, "Nanoscale chemical sensor based on organic thin-film transistors" *Appl. Phys. Lett.* 85 (26), 6386-6388 (2004)
- [66] R.M. Tiggelaar, T.T. Veenstra, R.G.P. Sanders, E. Berenschot, H. Gardeniers, M. Elwenspoek, A. Prak, R. Mateman, J.M. Wissink, A.v.d. Berg, "Analysis systems for the detection of ammonia based on micromachined components modular hybrid versus monolithic integrated approach" *Sens. Actuators B: Chem.* 92,25-36. (2003).

- [67] A. Yimit, K. Itoh, M. Murabayashi, "Detection of ammonia in the ppt range based on a composite optical waveguide pH" *Sens. Actuators B: Chem.* 88, 239–245. (2003).
- [68] T. Hutter, and S. Ruschin, "Non-imaging optical method for multi-sensing of gases based on porous silicon" *IEEE Sens. Journal*, 10, 97-103, (2010).
- [69] F. Winqvist, A. Spetz, I. Lundström, "Determination of urea with an ammonia gas-sensitive semiconductor device in combination with urease" *Anal. Chim. Acta* 164, 127–138. (1984).
- [70] A.L. Kukla, Y.M. Shirshov, S.A. Piletsky, "Ammonia sensors based on sensitive polyaniline films" *Sens. Actuators B: Chem.* 37, 135 (1996).
- [71] V.V. Chabukswar, S. Pethkar, A.A. Athawale, "Acrylic acid doped polyaniline as an ammonia sensor" *Sens. Actuators B: Chem.* 77, 657–663, (2001).
- [72] J. W. Jeong, Y. D. Lee, Y. M. Kim, Y. W. Park, J. H. Choi, T. H. Park, C. D. Soo, S. M. Won, I. K. Han and B. K. Ju, "The response characteristics of a gas sensor based on poly-3-hexylthiophene thin-film transistors" *Sens. Actuators B: Chem.* 146, 40–45, (2010).
- [73] H. Sirringhaus, T. Kawase, R. H. Friend, T. Shimoda, M. Inbasekaran, W. Wu, and E.P. Woo, "High-resolution inkjet printing of all-polymer transistor circuits" *Science*, Vol. 290, pp. 2123-2126, (2000).
- [74] A. Facchetti, "Semiconductors for organic transistors" *Materials Today*, 10, 28-37, (2007).
- [75] A. Salleo, "Charge transport in polymeric transistors" *Materials Today*, 10, 38-45, (2007).
- [76] C.D. Dimitrakopoulos and P.R.L. Malenfant, "Organic thin film transistors for large area electronics" *Adv. Mater.*, 14, 99-117, (2002).
- [77] H. Sirringhaus, P. J. Brown, R. H. Friend, M. M. Nielsen, K. Bechgaard, B. M. W.

- Langeveld-Voss, A. J. H. Spiering, R. A. J. Janssen, E. W. Meijer, P. Herwig, and D.M. de Leeuw, "Two-dimensional charge transport in self-organized, high-mobility conjugated polymers" *Nature*, 401, 685-688, (1999).
- [78] R. J. Kline, M.D. McGehee, E.N. Kadnikova, J. Liu, and J.M.J. Frechet, "Controlling the Field-Effect Mobility of Regioregular Polythiophene by Changing the Molecular Weight" *Adv. Mater.*, 15, 1519-1522, (2003).
- [79] Y. D. Park, D. H. Kim, Y. Jang, J. H. Cho, M. Hwang, H. S. Lee, J. A. Lim, and K. Cho, "Effect of side chain length on molecular ordering and field-effect mobility in poly (3-alkylthiophene) transistors" *Org. Electron.*, 7, 514-520, (2006).
- [80] R. J. Kline, M. D. McGehee, and M. F. Toney, "Highly oriented crystals at the buried interface in polythiophene thin-film transistors" *Nature Mater.*, 5, 222-228, (2006).
- [81] J. J. Apperloo, R. A. J. Janssen, M. M. Nielsen, and K. Bechgaard, "Doping in Solution as an Order-Inducing Tool Prior to Film Formation of Regio-Irregular Polyalkylthiophenes" *Adv. Mater.*, 12, 1594-1597, (2000).
- [82] Y. D. Park, J. H. Cho, D. H. Kim, Y. Jang, H. S. Lee, K. Ihm, T. H. Kang, and K. Cho, "Energy-level alignment at interfaces between gold and poly (3-hexylthiophene) films with two different molecular structures" *Electrochem. Solid-State Lett.*, 9, G317-G319, (2006).
- [83] D.H. Kim, J.T. Han, Y.D. Park, Y. Jang, J.H. Cho, M. Hwang, and K. Cho, "Single-Crystal Polythiophene Microwires Grown by Self-Assembly" *Adv. Mater.*, 18, 719-723 (2006).
- [84] I. McCulloch, M. Heeney, C. Bailey, K. Genevicius, I. Macdonald, M. Shkunov, D. Sparrowe, S. Tierney, R. Wagner, W. Zhang, M.L. Chabinyc, R. J. Kline, M.D. McGehee and M. F. Toney, "Liquid-crystalline semiconducting polymers with

- high charge-carrier mobility” *Nature Mater.* 5, 328, (2006).
- [85] M. Halik, M. Halik, H. Klauk, U. Zschieschang, G. Schmid, C. Dehm, M. Schütz, S. Maisch, F. Effenberger, M. Brunnbauer, F. Stellacci “Low-voltage organic transistors with an amorphous molecular gate dielectric” *Nature* 431, 963, (2004).
- [86] J.Z. Wang, Z.H. Zheng, H.W. Li, W.T.S. Huck, and H. Sirringhaus, “Dewetting of conducting polymer inkjet droplets on patterned surfaces” *Nature Mater.* 3, 171, (2004).
- [87] Y. Zhang, Y. Guan, S. Yang, J. Xu, and C.C. Han, “Fabrication of Hollow Capsules Based on Hydrogen Bonding” *Adv. Mater.* 15, 1632, (2003).
- [88] M.D. Austin and S.Y. Chou “Fabrication of 70 nm channel length polymer organic thin-film transistors using nanoimprint lithography” *Appl. Phys. Lett.* 81, 4431, (2002).
- [89] J. Zaumseil, T. Someya, Z. Bao, Y.-L. Loo, R. Cirelli, and J. A. Rogers “Nanoscale organic transistors that use source/drain electrodes supported by high resolution rubber stamps” *Appl. Phys. Lett.* 82, 793, (2003).
- [90] N. Stutzmann, R. H. Friend, and H. Sirringhaus, “Self-aligned, vertical-channel, polymer field-effect transistors” *Science* 299, 1881, (2003).
- [91] R. Parashkov, E. Becker, G. Ginev, T. Riedl, M. Brandes, H.-H. Johannes, and W. Kowalsky, “Organic vertical-channel transistors structured using excimer laser” *Appl. Phys. Lett.* 85, 5751, (2004).
- [92] R. Parashkov, E. Becker, S. Hartmann, G. Ginev, D. Schneider, H. Krautwald, T. Dobbertin, D. Metzdorf, F. Brunetti, C. Schildknecht, A. Kammoun, M. Brandes, T. Riedl, H.-H. Johannes, and W. Kowalsky, “Vertical channel all-organic thin-film transistors” *Appl. Phys. Lett.* 82, 4579, (2003).
- [93] M.S. Meruvia, I.A. Hümmelgen, M.L. Sartorelli, A.A. Pasa, and W. Schwarzacher, “Organic-metal-semiconductor transistor with high gain” *Appl.*

Phys. Lett. 84, 3978, (2004).

- [94] K. Kudo, D.X. Wang, M. Iizuka, S. Kuniyoshi, and K. Tanaka “Schottky gate static induction transistor using copper phthalocyanine films” *Thin Solid Films* 331, 51, (1998).
- [95] K. Fujimoto, S. Kera, T. Kataoka, S. Hosoumi, Y. Watanabe, K. Kudo, and N. Ueno “The Role of the Ionization Potential in Vacuum-Level Alignment at Organic Semiconductor Interfaces” *Adv. Mater.* 19, 525, (2007).
- [96] Y. Yang and A.J. Heeger, “A new architecture for polymer transistors” *Nature* 372, 344, (1994).
- [97] S.-H. Li, Z. Xu, G. Yang, L. Ma, and Yang Yang, “Solution-processed poly(3-hexylthiophene) vertical organic transistor” *Appl. Phys. Lett.* 93, 213301 (2008).
- [98] Y.-C. Chao, M.-H. Xie, M.-Z. Dai, H.-F. Meng, S.-F. Horng and C.-S. Hsu, “Polymer hot-carrier transistor with low bandgap emitter” *Appl. Phys. Lett.* 92,093310 (2008).
- [99] J. Huang, M. Yi, D. Ma, and I. A. Hümmelgen, “Vertical structure p-type permeable metal-base organic transistors based on N,N-diphenyl-N,N-bis(1-naphthylphenyl)-1,1-biphenyl-4,4-diamine” *Appl. Phys. Lett.* 92, 232111 (2008).
- [100] Y.-C. Chao, H.-F. Meng, S.-F. Horng, C.-S. Hsu, “Polymer space-charge limited transistor” *Organic Electronics.* 9, 310–316 (2008).
- [101] K. Fujimoto, T. Hiroi, K. Kudo, and M. Nakamura, “High-performance vertical-type organic transistors with built-in nanotriode arrays” *Adv. Mater.* 19, 525–530 (2007).

Chapter 2. Effective Mobility Enhancement by Using Nanometer Dot Doping in amorphous IGZO Thin-Film Transistors

2.1. Introduction

With a high mobility ($>10 \text{ cm}^2 \text{ V}^{-1} \text{ s}^{-1}$) and a low threshold voltage ($< 5 \text{ V}$) under a low temperature process, transparent oxide semiconductor thin-film transistors (TOS TFTs) draw considerable attention due to their applications on flexible displays, level shifters, drivers, and pixel driving circuits for active-matrix organic-light-emitting-diode (AMOLED) displays. [1–3] In addition to display applications, a-IGZO TFTs are also promising for the development of radio-frequency identification (RFID) tags, smart cards, and other types of flexible electronics. When TOS TFTs are developed for a low-power high-frequency circuit, high electron mobility and a low parasitic capacitance are required. Most TFTs fabricated with ZnO, SnO₂, In₂O₃, IGZO or other semiconducting oxide thin films exhibit electron mobilities smaller than $35 \text{ cm}^2 \text{ V}^{-1} \text{ s}^{-1}$. [4–6] Recent reports on transparent oxide nanowire transistors (NWTs) have demonstrated high electron mobilities approximately $70 \sim 4000 \text{ cm}^2 \text{ V}^{-1} \text{ s}^{-1}$. [7–9] The quasi-one-dimensional structure of NWTs may reduce low-angle carrier scattering to produce high electron mobility.^[9] However, the fabrication process of NWTs has a poor reproducibility and is still not practical for real applications. Because TOS transistors are transparent, developing TOS circuits on windows is appealing. Particularly, for modern buildings or trains with series of windows, TOS RFID circuits on windows can deliver various types of signals through a low-power transmission system. In this type of application, the

dimension of the transparent transistor can be large because an integrated circuit on a small chip is not necessary. A low cost production method for delivering a high performance TOS transistor is the critical challenge.

This report proposes a new nanostructure to improve the effective mobility in a-IGZO TFTs. A large channel dimension of one thousand micron meters defined by a shadow mask is utilized. The nanostructure is developed using a low-cost, lithography-free process to produce abundant nanometer-scale dot-like doping in a-IGZO channel. The new method, called “nano-dot doping” (NDD) increases electron mobility to a level 19 times higher than that of the control. This study demonstrates a lithography-free, low-cost process utilizing self-organized polystyrene spheres with a diameter as 200 nm to fabricate a porous gate structure. Ar plasma treatment through the porous gate performs dot-like doping on a-IGZO channel region. An effective field-effect mobility ($\sim 79 \text{ cm}^2 \text{ V}^{-1} \text{ s}^{-1}$) top-gate self-aligned a-IGZO TFT is realized. The top-gate (TG) self-aligned structure also eliminates the overlaps between the gate electrode and the source/drain contacts, which are known to suppress the parasitic capacitance and increase the response speed. This paper discusses the influences of dot and doping concentrations on device performance. The application of NDD treatment on conventional bottom-gate (BG) a-IGZO TFT is also demonstrated. After NDD treatment, this study observed a two-fold improvement of electron mobility in a conventional bottom-gate a-IGZO TFT.

2.2. Experiment

2.2.1. Device Fabrication Process

This study fabricated top gate (TG) structures with nano-dot doping (NDD) and without NDD (named STD hereafter).

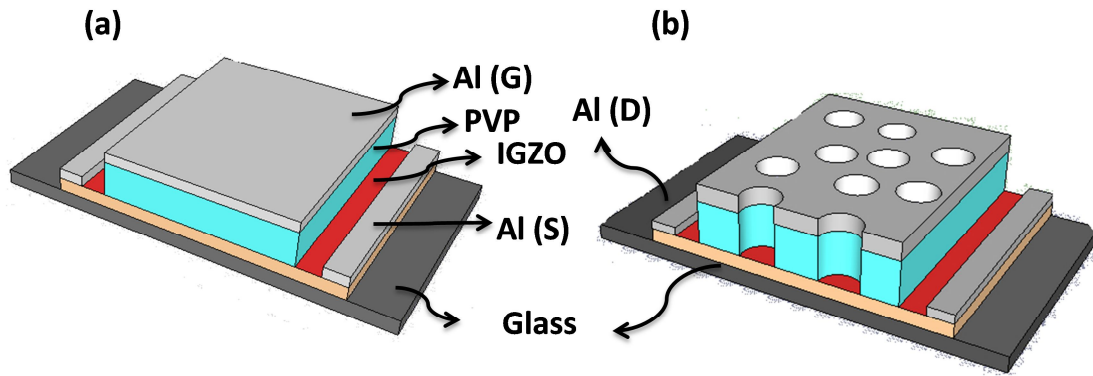


Figure 2.1 The schematic device structures of (a) STD (standard) and (b) NDD (nano-dot doping) top gate (TG) a-IGZO TFTs.

Two device structures called “TG-STD” (top-gate without NDD) and “TG-NDD” (top-gate with NDD) are depicted in **Figures 2.1(a)** and **2.1(b)**, respectively. The SEM image of the cross sectional view of the channel region of TG-NDD device is shown in **Figure 2.2**. Openings with a 200 nm diameter can be observed in the channel region.

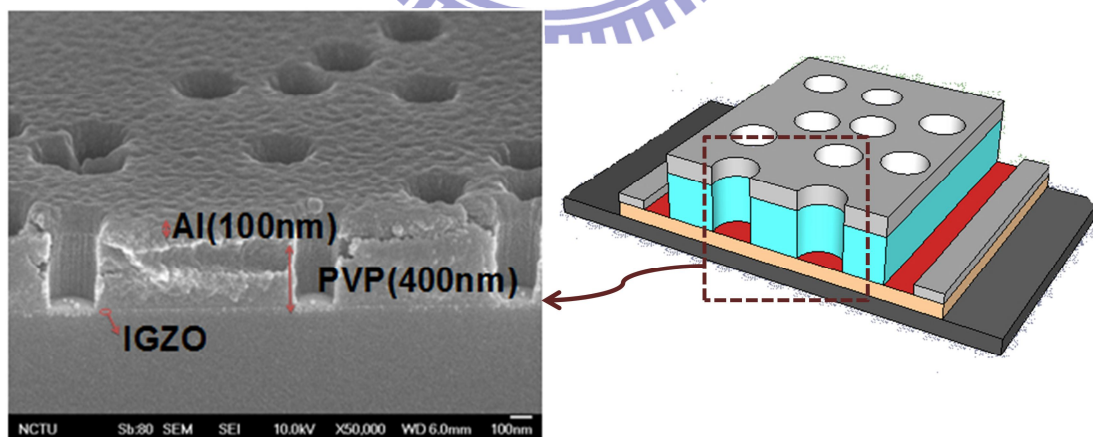


Figure 2.2 The SEM image of the cross sectional view of the TG-NDD a-IGZO TFTs in the channel region.

The process flow of fabricating TG-NDD is shown in **Figure 2.3**. Glass substrate (CORNING Eagle 2000) must keep clean or films may become rough. The rough surface would cause point discharge between the insulator and metal. The steps of clean glass substrate are shown as following.

Steps:

- (1) De Ion (DI) water current flows for 5 minutes in order to remove the particles.
- (2) The substrates should be placed under the in the acetone and ultrasonic resonance for 5 minutes in order to remove the organic pollution. Then, the substrates have to put under the DI water current flow for 5 minutes in order to remove the solvent.
- (4) The substrates were put in the KG detergent bath with ultrasonic resonance for 5 minutes in order to remove the particles, fingerprint, and ionic.
- (5) The substrates were put under the DI water current flow for 5 minutes in order to remove the solvent.
- (6) Finally, the substrates would be fried with dry N_2 flow to blow off the water on the substrates.

30-nm-thick *a*-IGZO (3-in. circular target: In:Ga:Zn = 1:1:1 at %) was deposited by radio-frequency (RF) sputtering onto a pre-cleaned glass substrate through a shadow mask to form the active layer at room temperature. During the sputtering, the RF power and chamber pressure were 100 W and 9 mTorr while Ar flow rate maintains at 30 sccm. The annealing process was then performed at 400 °C in a nitrogen furnace for 90 min. A 4000 Å cross-linkable poly(4-vinyl phenol) (PVP) was spin-coated on the *a*-IGZO surface, and then cross-linked at 200° C for 60 min in air to serve as the gate insulator. The capacitance and the relative dielectric constant of PVP is 13.2 nFcm⁻² and 3.5, respectively. Poly (melamine-co-formaldehyde) methylated (Aldrich, Mw~511) was utilized as a crosslinking agent for PVP. The surface of PVP was

turned into hydrophilic by short-time exposure of 50 W O₂ plasma before submerging the substrate into 2000 Å positively charged polystyrene spheres (Merck, K6–020) diluted in ethanol solution with 0.2 or 0.8 wt %. The scanning electron microscope (SEM) images of the PVP with 0.2 or 0.8 wt % PS sphere concentrations are shown in **Figures 2.3(b)** and **2.3(c)**, respectively. By counting the PS spheres on SEM images in **Figures 2.3(b)** and **2.3(c)**, the concentration of dots per area is estimated to be $6.8 \times 10^6 \text{ mm}^{-2}$ for 0.8 wt % PS spheres and is $4.8 \times 10^6 \text{ mm}^{-2}$ for 0.2 wt % PS spheres, respectively.

The polystyrene spheres were adsorbed on the PVP surface to serve as the shadow mask. After submerging the substrate for 3 min in a polystyrene sphere solution, the substrate was then transferred into a beaker with boiling isopropanol solution for 10 s to avoid the accumulation of PS spheres. The substrate was immediately blown dry to form two-dimensional columnar arrays. A 1000 Å Al was evaporated as a metal gate electrode. After removing the polystyrene spheres using an adhesive tape (Scotch, 3M), the PVP at sites without Al coverage was removed after 8 min 150 W O₂ plasma treatment.

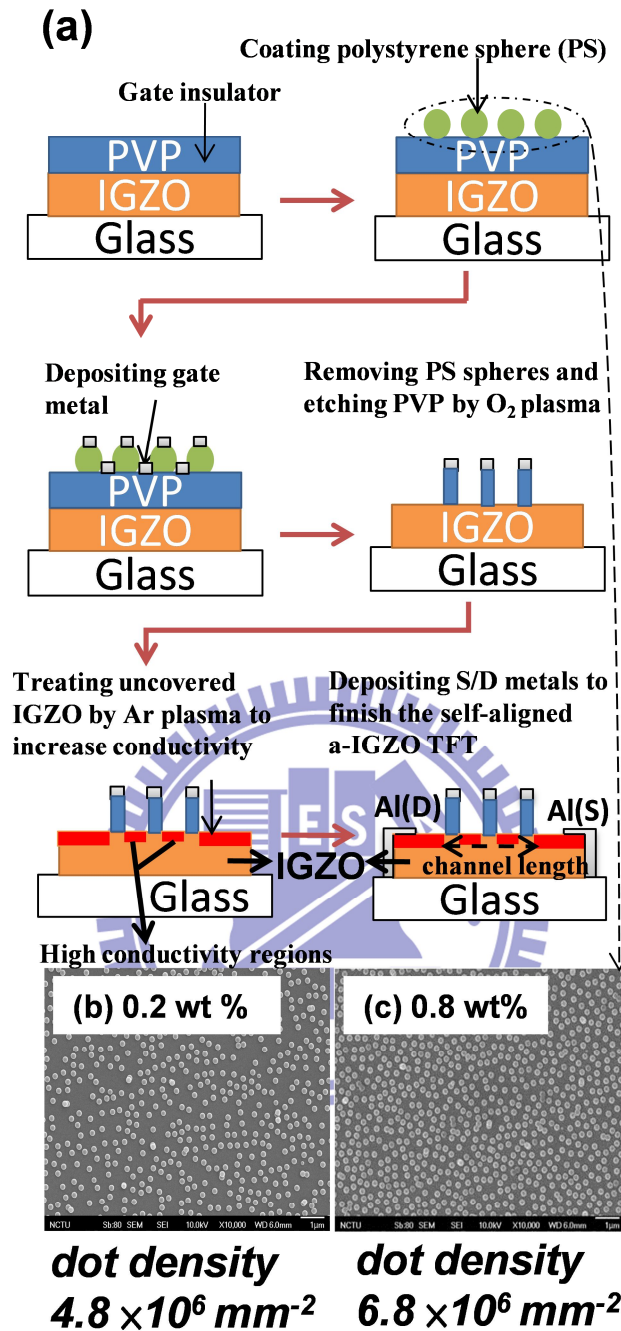


Figure 2.3 (a) The processes flow of the TG-NDD (top-gate with nano-dot doping) a-IGZO TFT. The SEM images of the PVP substrate adsorbed with (b) 0.2 wt % and (c) 0.8 wt % polystyrene spheres. The diameter of the sphere is 200 nm. By counting the PS spheres on SEM images in Figures 6.3(b) and 6.3(c), the concentration of dots per area is estimated to be $6.8 \times 10^6 \text{ mm}^{-2}$ for 0.8 wt % PS spheres and is $4.8 \times 10^6 \text{ mm}^{-2}$ for 0.2 wt % PS spheres, respectively.

The source/drain region and the bare channel region (without PVP coverage) was then treated with Ar plasma to increase the conductivity. Finally, a 100-nm-thick layer of Al used as a source/drain metal was evaporated at room temperature through a shadow mask. The Ar plasma treatment on the source/drain regions of the a-IGZO active layer lowered the series resistance between the source/drain metal pads and the induced channel under the gate region. After Ar treatment, a self-aligned structure was formed. The channel width is defined by the edge of the a-IGZO pattern. For top-gate device (TG-STD and TG-NDD), the channel length is defined by the edge of the gate electrode. Due to the confinement of the a-IGZO pattern, there is no current spreading outside the channel region. The channel width and length of the top gate devices are listed in Table 2.1. For TG-STD, the process flow is similar to that depicted in **Figure 2.3** except that the PS sphere absorption process is removed.

2.3. Results and Discussions

2.3.1. The Resistivity Variation of a-IGZO Thin Film after Ar Plasma Treatment

Figure 2.4 shows the resistivity of the a-IGZO thin film as a function of the Ar plasma exposure time. The resistivity of a-IGZO film is drastically reduced from $>10^5$ Ωcm to 3.85 Ωcm during the Ar plasma treatment. After that, the resistivity seemed to become saturated with the plasma exposure time was increased to 300 s. In addition, the reason why the saturation of carrier density was observed above the treatment time of 60 s can be tentatively speculated as follows: As a consequence of preferential sputtering of oxygen, the enrichment of cations including In, Ga, and Zn on the surface would balances out the preferential sputtering of oxygen, which makes the steady-state condition (i.e., saturation behavior) achieved.[11]

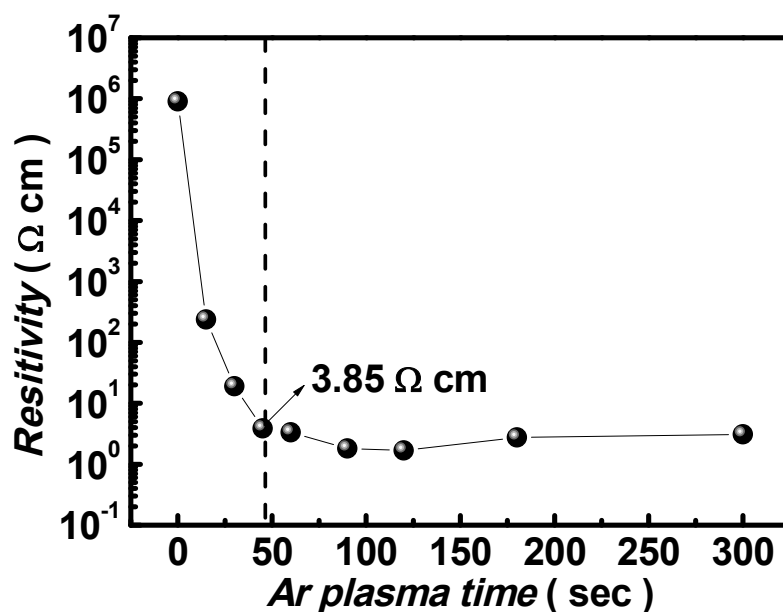


Figure 2.4 Resistivity of the *a*-IGZO thin film as a function of the Ar plasma exposure time. The resistivity of *a*-IGZO film is drastically reduced from $>10^5 \Omega\text{cm}$ to $3.85 \Omega\text{cm}$ during the Ar plasma treatment. After that, the resistivity seemed to become saturated with the plasma exposure time was increased to 300 sec.

In order to further verify the reduced resistivity after the Ar plasma treatment, we utilized the X-ray photoelectron spectroscopy (XPS) to analyze the bared *a*-IGZO thin film with and without Ar plasma treatment. From the O1s XPS spectrum, which is shown in **Figure 2.5**, the oxygen vacancies is increased with the plasma treatment sample and the result is consistent with reference 10. The peak with the lower energy value of 530.5 eV, represents O^{2-} ions combined with Zn, Ga, and In ions, in the IGZO compound system. The medium binding energy value at 531.5 eV, is associated with O^{2-} ions which are in oxygen vacancies regions within the IGZO films. The higher binding energy value of 532.5 eV, is related to loosely bonded oxygen on the IGZO surface, including absorbed H_2O , CO_3 , or O_2 . We can observe the area ratio of O_M 1s peak to O_L 1s peak in IGZO and IGZO with Ar plasma treatment is 25.54% and 34.53%, respectively. Therefore, it is clear that the huge change in the resistivity of the *a*-IGZO film is due to the creation of the net electron carriers during the Ar

plasma treatment. It is believed that the dramatic change of the electron concentration upon the exposure to the Ar plasma comes from the oxygen deficiency on the *a*-IGZO film surface. This result is consistent with a previous report on ZnO film.[11]

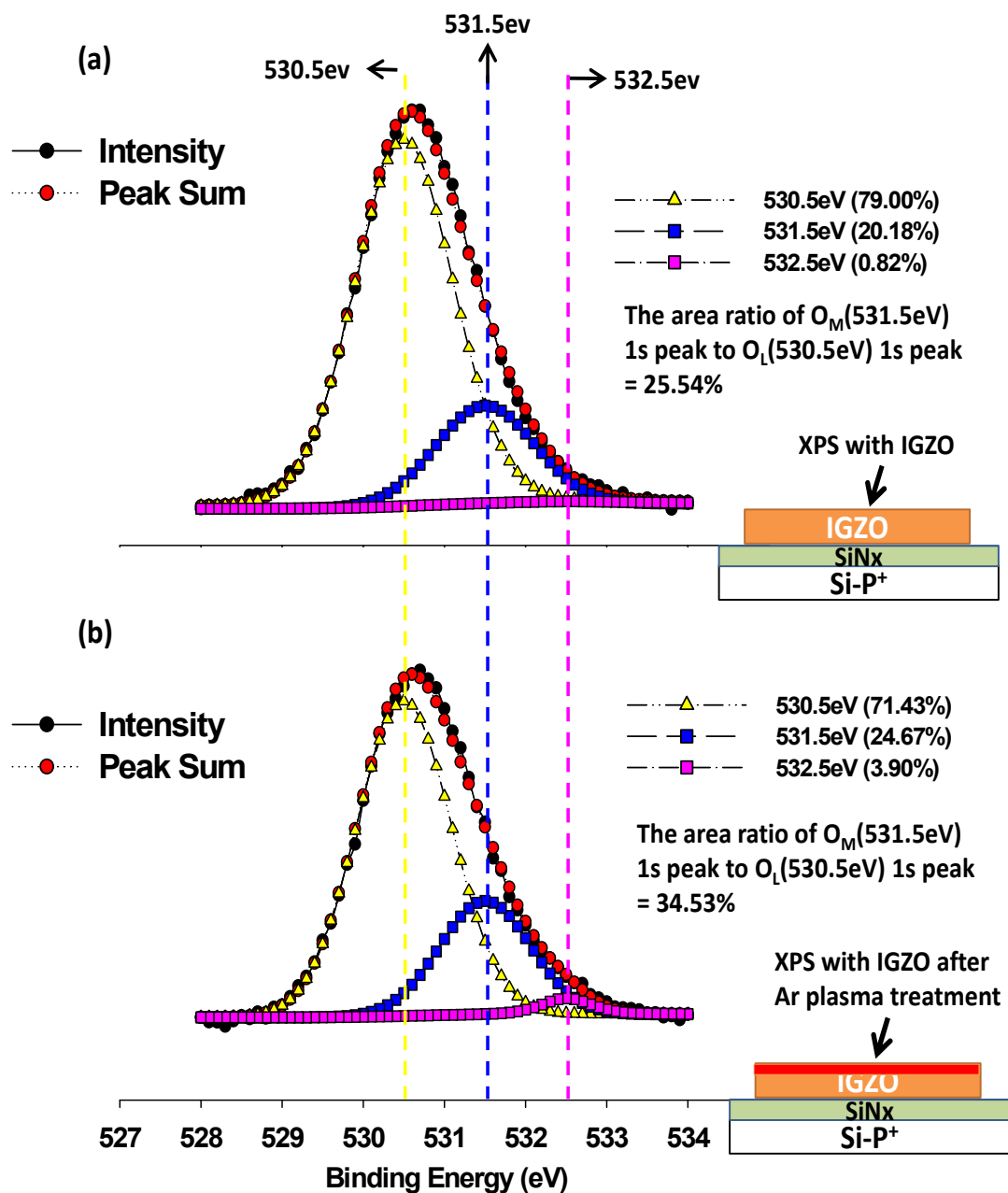


Figure 2.5 (a) and (b) are O_{1s} XPS spectra for IGZO without and with Ar plasma treatment films, respectively. The peak with the lower energy value of 530.5 eV, represents O^{2-} ions combined with Zn, Ga, and In ions, in the IGZO compound system. The medium binding energy value at 531.5 eV, is associated with O^{2-} ions which are in oxygen vacancies regions within the IGZO films. The higher binding energy value of 532.5 eV, is related to loosely bonded oxygen on the IGZO surface, including absorbed H_2O , CO_3 , or O_2 .

Also, from the result of O1s (XPS) spectra for a-IGZO thin film (shown in **Figure 2.5**), the relative concentrations of oxygen vacancies ($V_o^{\cdot\cdot}$, peak centered at ~ 531.5 eV) in IGZO films is increased from 20.18 % to 24.67 % after the Ar plasma treatment. (the relative concentrations of oxygen vacancies in IGZO films is calculated by the area integration of O1s (V_o) peak to the area integration of each O1s peak).[10]

In previous reports, it has been found that the Ar plasma treated surface exhibits higher In concentration, lower Ga concentration, and lower Zn concentration than does the untreated sample.[11] The In-rich surface contributes to the formation of a region with high electron concentration because the weak bonds between the In ions and oxygen are more likely to generate carriers than the Ga-O bonds or Zn-O bonds.[12] The variation in the cation composition (In, Ga, and Zn), however, was not the only reason to cause the dramatic decrease of the resistivity after Ar plasma treatment. The increase of oxygen deficiency after the Ar ion bombardment was a critical factor in causing the drastic resistivity change.[11]

2.3.2. The Influence of Ar Plasma Treatment Time on a-IGZO TFT

The transfer characteristics of TG-STD devices with different Ar plasma treatment durations are compared in **Figure 2.6**. In **Figure 2.6**, device channel width is $3000 \mu\text{m}$ and the channel length is $1000 \mu\text{m}$. In this top-gate device, the Ar plasma treatment produces the source and drain regions with high electron concentration. Without the Ar plasma treatment, the offset regions between the gate-induced-channel and the source/drain electrodes are highly resistive. As a result, no turn-on characteristics can be observed. After a suitable Ar plasma treatment (for example, the 3-min treatment depicted in **Figure 2.6**), the conductivity in the offset regions becomes high enough to serve as the source and drain regions. The transistor exhibits normal transfer

characteristics.

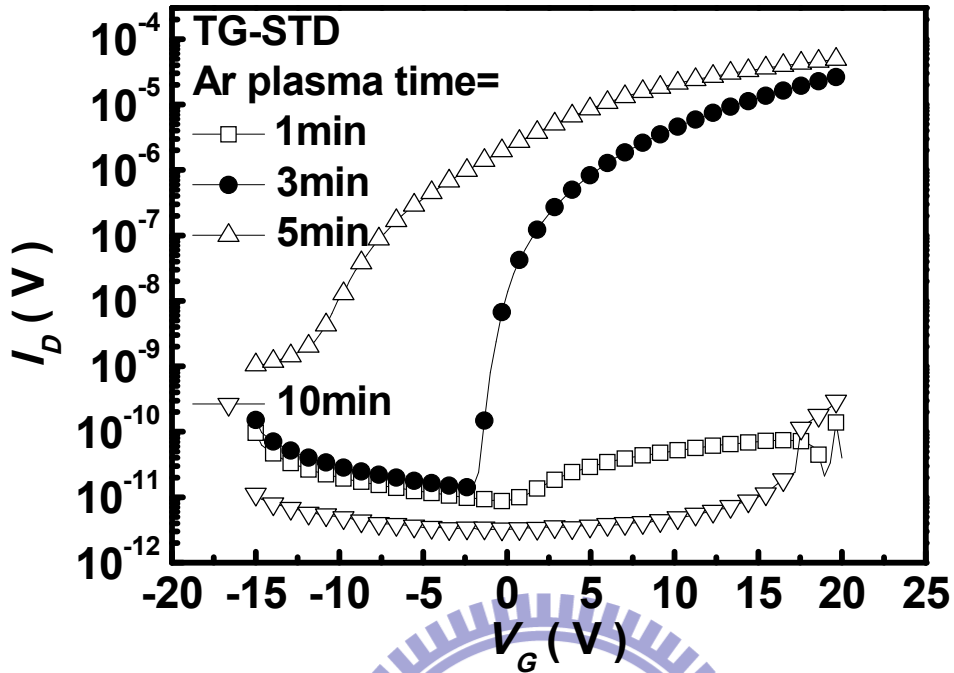


Figure 2.6 The transfer characteristics of TG-STD devices with different Ar plasma treatment time on source/drain electrodes. The device channel width is 3000 μm and the channel length is 1000 μm .

When the Ar plasma treatment time increases to 5 mins, the leakage current is raised because the sidewall of the PVP layer is damaged by the Ar ions. When the Ar plasma treatment time increases to 10 mins, the thin IGZO film is damaged due to the etching effect caused by the Ar ion bombardment. No turn on characteristics can be observed.

The transfer characteristics of TG-NDD (PS 0.8 wt %) device with different Ar plasma treatment durations are shown in **Figure 2.7**. Device channel width is 3000 μm and the channel length is 1000 μm . In addition to forming the conductive source and drain regions, Ar plasma treatment in TG-NDD devices also produces a nanometer-scale dot-like doping in IGZO front channel surfaces.

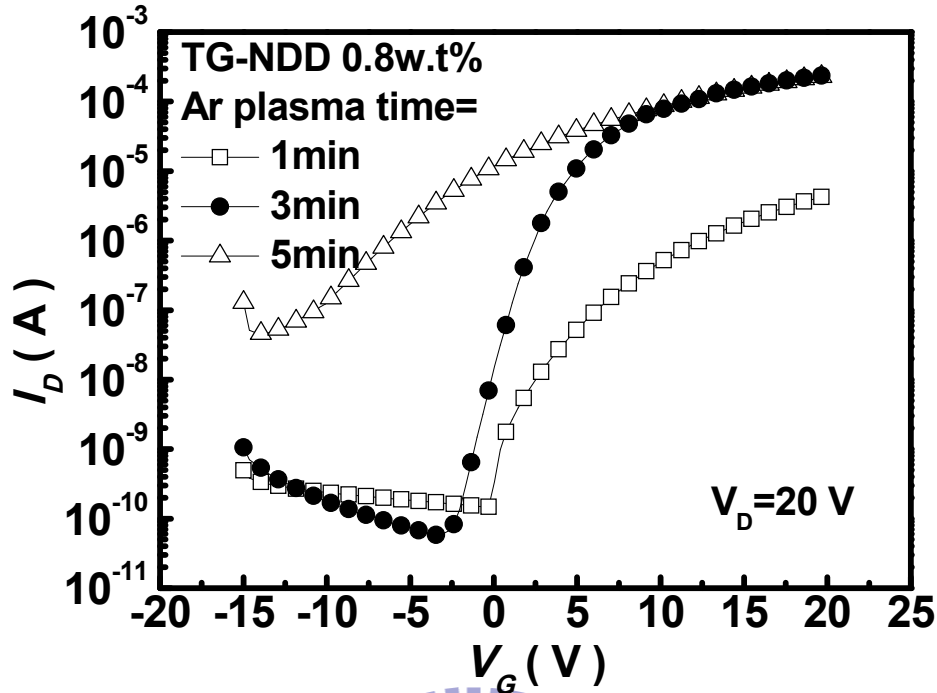


Figure 2.7 The transfer characteristics of TG-NDD devices with high density dots (0.8 wt % PS spheres) with different Ar plasma treatment time. The device channel width is 3000 μm and the channel length is 1000 μm .

When the Ar plasma time is 3 min, the device exhibits superior transfer characteristics. The on current is higher than 0.1 mA; the off current remains lower than 1 nA; the effective field-effect mobility is $79 \text{ cm}^2 \text{ V}^{-1} \text{ s}^{-1}$; the subthreshold swing is $1.2 \text{ V decade}^{-1}$; and the threshold voltage is -2.94 V . When the Ar plasma time increases to 5 min, both the source to drain leakage current and the gate leakage current are raised.

Figure 2.8 shows the output characteristics (drain current (I_D)) as a function of drain voltage (V_D) of TG-NDD (PS 0.8 wt %) a-IGZO TFT with channel width and length as 3000 μm and 1000 μm , respectively. The transistor operates in the enhancement mode. I_D increases linearly with increasing V_D at low V_D , and saturates at higher V_D .

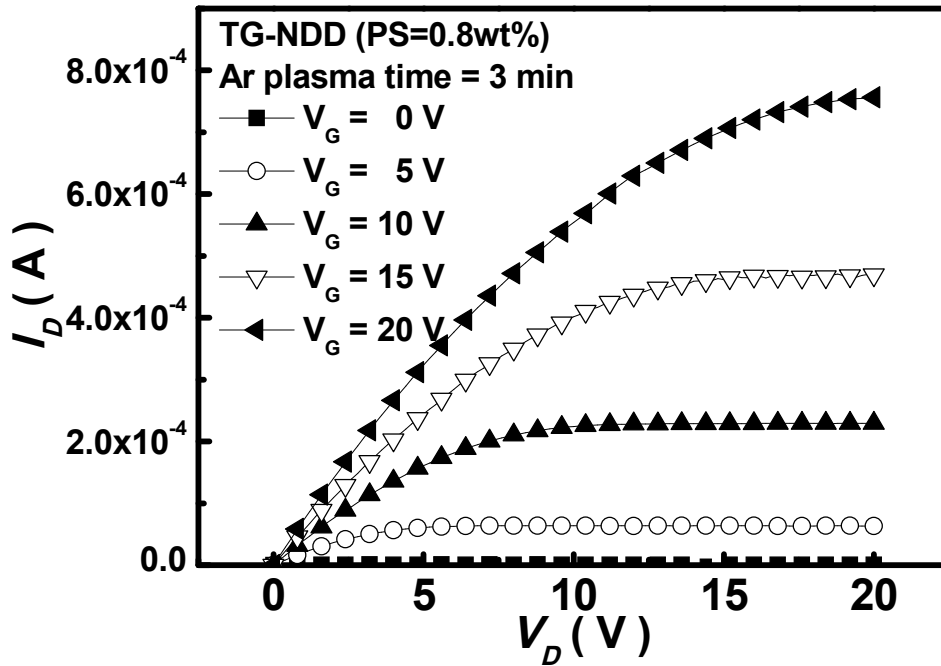


Figure 2.8 The output characteristics of TG-NDD devices (PS spheres: 0.8 wt %) with the optimal Ar plasma treatment time (3 mins). The device channel width is 3000 μm and the channel length is 1000 μm .

2.3.3. The Influence of Dots Concentration on a-IGZO TFT

The influences of the nano-dot concentration on the device performance are studied by fabricating TG-NDD devices with different PS sphere densities. The SEM images of the low-density PS sphere mask (PS 0.2 wt %) and the high-density PS sphere mask (PS 0.8 wt %) are shown in **Figure 2.3(b)** and **Figure 2.3(c)**, respectively. The transfer characteristics and the root square of the drain current plotted as a function of gate bias of TG-STD, TG-NDD (PS 0.2 wt %), and TG-NDD (PS 0.8 wt %) are compared in **Figure 2.9** when channel width and length are 3000 μm and 1000 μm , respectively.

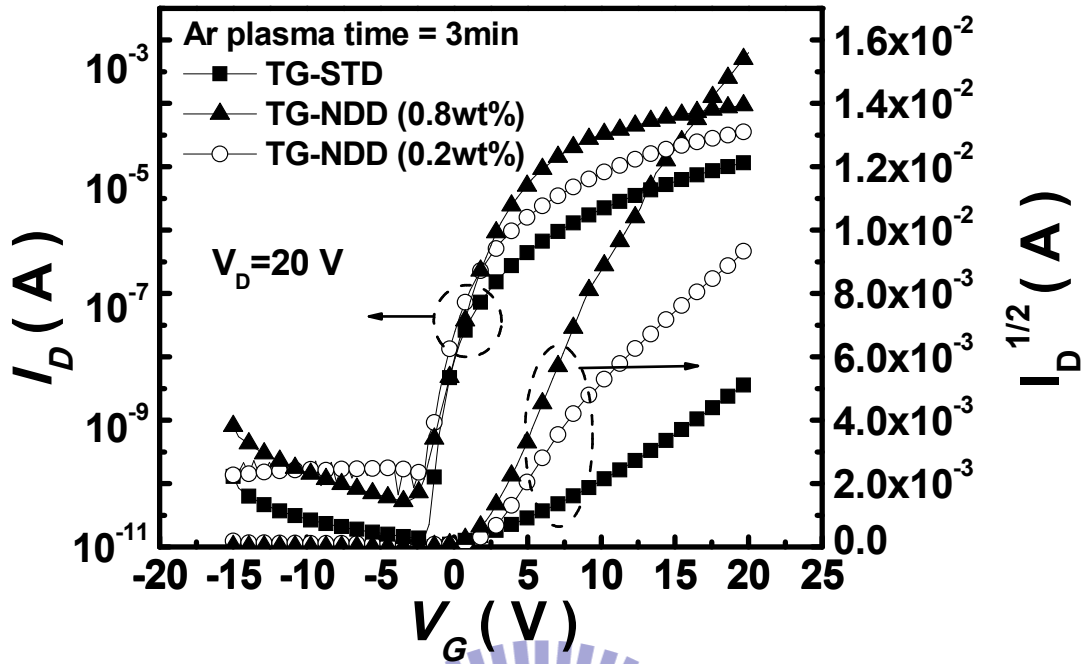


Figure 2.9 The transfer characteristics and the root square of the drain current plotted as a function of gate bias for three devices: TG-STD, TG-NDD (PS 0.2 wt %), and TG-NDD (PS 0.8 wt %). The device channel width is 3000 μm and the channel length is 1000 μm .

In Table 2.1, we listed the threshold voltage, the maximum field-effect mobility, the average mobility, the standard deviation of the mobility, the subthreshold swing, and the on/off current ratio for the TG-STD and TG-NDD devices with different W/L ratios (3, 3.3, and 10).

Table 2.1 Comparisons of typical parameters in TG-STD and TG-NDD a-IGZO TFTs.

TG-STD	W/L($\mu\text{m}/\mu\text{m}$)	W/L ratio	V_{th} (V)	μ_{max} [a](μ_{avg} [b]) ($\text{cm}^2\text{V}^{-1}\text{s}^{-1}$)	σ [c] ($\text{cm}^2\text{V}^{-1}\text{s}^{-1}$)	S.S. (V/dec)	On/Off
	1000/100	10	-3.1	5.53 (4.87)	0.304	0.97	1.7×10^5
	1000/300	3.33	-3.1	5.54 (5.3)	0.13	0.39	2.8×10^6
	3000/1000	3	0.5	4 (3.38)	0.24	0.67	1.6×10^6
TG-NDD (0.8 wt %)	W/L($\mu\text{m}/\mu\text{m}$)	W/L ratio	V_{th} (V)	μ_{max} [a](μ_{avg} [b]) ($\text{cm}^2\text{V}^{-1}\text{s}^{-1}$)	σ [c] ($\text{cm}^2\text{V}^{-1}\text{s}^{-1}$)	S.S. (V/dec)	On/Off

	1000/100	10	-2.29	87.4 (N/A)	N/A	0.49	1.06×10^6
	1000/300	3.33	-2.47	71.7 (N/A)	N/A	0.34	1.81×10^5
	3000/1000	3	-2.94	79.2 (67.5)	6.1	0.92	9.42×10^6
TG-NDD (0.2 wt %)	W/L($\mu\text{m}/\mu\text{m}$)	W/L ratio	V_{th} (V)	μ_{max} [a](μ_{avg} [b]) ($\text{cm}^2\text{V}^{-1}\text{s}^{-1}$)	σ [c] ($\text{cm}^2\text{V}^{-1}\text{s}^{-1}$)	S.S. (V/dec)	On/Off
	1000/100	10	-5.91	45.6 (N/A)	N/A	0.29	3.5×10^6
	1000/300	3.33	-4.5	47.5 (43.7)	4.16	0.72	5.6×10^6

[a] μ_{max} is the maximum effective field-effect mobility.

[b] μ_{avg} and [c] σ are average effective mobility and standard deviation calculated from 5 independent devices.

The TG-STD devices, the TG-NDD with high density dots (produced with 0.8 wt % polystyrene spheres), and the TG-NDD with low density dots (produced with 0.2 wt % polystyrene spheres) are compared. The TG-NDD structure obviously increases the field-effect mobility when we increase the concentration of the doping dots. The effective field-effect mobility (71.7 to $87.4 \text{ cm}^2 \text{V}^{-1} \text{s}^{-1}$) can be obtained for TG-NDD with high density dots and with a W/L ratio ranged from 3 to 10. The reproducibility is represented by the standard deviation of the mobility as listed in Table 2.1. To improve the reproducibility and the uniformity, an ordered dot-like structure is required. Nano imprint may be utilized to produce the ordered nano-scale dot-like structure in future works. The improvement of mobility by NDD is observed for devices with various channel widths and lengths. Also, changing the W/L ratio doesn't significantly influence the mobility. The reported mobility overestimation due to the current spreading is not observed.[13] The device pattern used in our study is shown in **Figure 2.10(a)**. The device pattern reported in reference 13 is shown in **Figure 2.10 (b)**. In **Figure 2.10 (b)**, the active region (ZnO layer) is undefined. As a result, current spreading at the edges of the source and the drain electrodes cause an overestimation of the mobility. In our work, the channel width is defined by the IGZO

pattern, not by the source/drain electrodes. A well confined active region avoids current spreading outside the channel region.

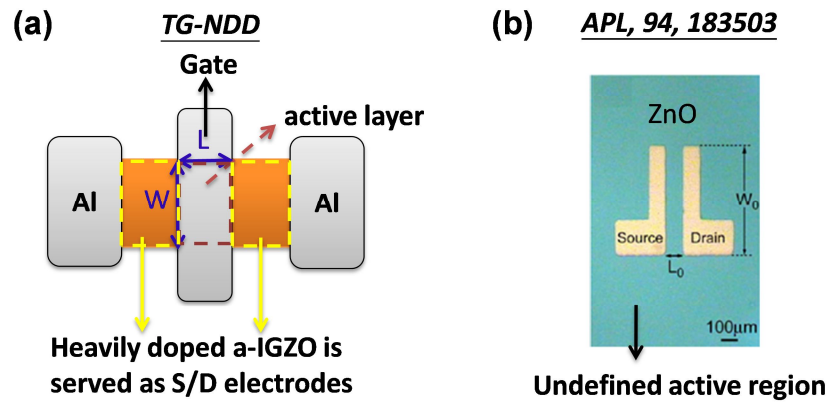


Figure 2.10 (a)The top view of device structure in the work and (b) top view of the device structure in reference 13.

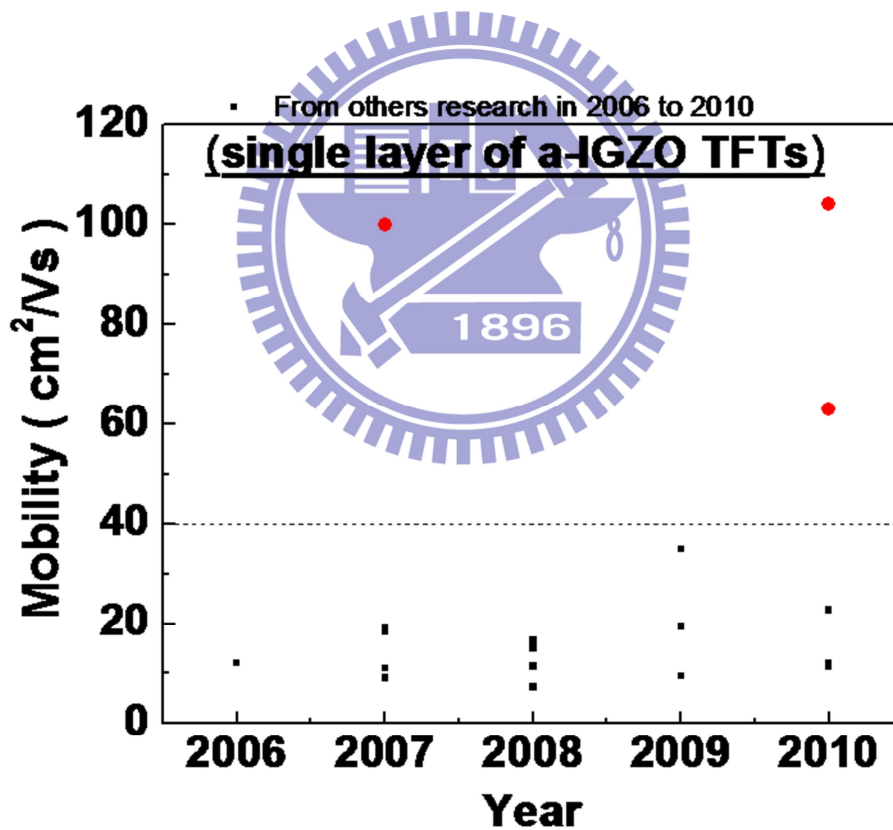


Figure 2.11 Effective field-effect electron mobility of this work and of other reports from 2006 to 2010.

In **Figure 2.11**, we compare the reported mobility of a-IGZO TFTs from 2006 to 2010. When most reported field-effect mobilities of a-IGZO TFTs are lower than $35 \text{ cm}^2 \text{ V}^{-1} \text{ s}^{-1}$, [4–6] three previous studies have reported high mobility a-IGZO TFTs. The typical parameters of the high mobility a-IGZO TFTs in these previous reports are also listed in Table 2.1. Kim *et al.* proposed that the metal-oxide TFT with ITO/IGZO double active layer exhibits a high mobility of $104 \text{ cm}^2 \text{ V}^{-1} \text{ s}^{-1}$. [14] Lee *et al.* utilized a multilayer gate insulator to realize an effective field-effect mobility of $100 \text{ cm}^2/\text{Vs}$. [3] In these reports, the photolithography process is required to realize a channel length smaller than $20 \mu\text{m}$. Chiu *et al.* proposed a lithography-free long-channel a-IGZO TFT with a high-k gate dielectric to realize a high mobility of $62 \text{ cm}^2 \text{ V}^{-1} \text{ s}^{-1}$. [15] In our work, an effective mobility of $79 \text{ cm}^2 \text{ V}^{-1} \text{ s}^{-1}$ can be achieved using nano-dot doping with a $1000 \mu\text{m}$ channel length and a conventional silicon nitride gate dielectric. It is expected that the effective field-effect mobility could be further increased if a high-k dielectric is used with the NDD structure.

2.3.4. The Plausible Mechanism of Increased Mobility

The drastically enhanced the effective field-effect mobility in NDD structures may be because of two reasons. Firstly, the effective channel length is reduced due to the conductive dot regions inside the channel. The effective channel length for TG-NDD devices can be estimated by calculating the dots concentration [shown in **Figure 2.12**]. From these two SEM images in **Figure 2.12**, we estimated the average PS spheres in different dots concentration. The average dots of 0.2 wt% and 0.8 wt% are 1583 and 2500 per $1000 \mu\text{m}$, respectively. Then, the effective channel length is equal to the channel length definition by shadow mask minus the high conductive region.

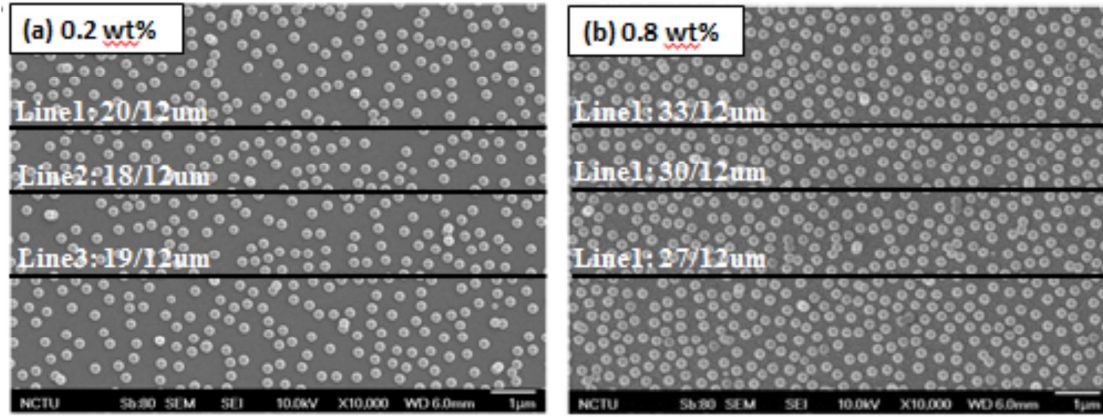


Figure 2.12 The SEM images of different dots concentration.

For TG-NDD devices with high-density dots (with 0.8 wt% PS spheres), the effective channel length reduces from 1000 μm to 500 μm . For TG-NDD devices with low-density dots (with 0.2 wt% PS spheres), the effective channel length reduces from 1000 μm to 684 μm . If the effective intrinsic channel length is used to estimate the mobility inside the intrinsic a-IGZO region, the intrinsic mobility is 39.6 $\text{cm}^2 \text{V}^{-1} \text{s}^{-1}$ for TG-NDD devices with high-density dots and is 32.5 $\text{cm}^2 \text{V}^{-1} \text{s}^{-1}$ for TG-NDD devices with low-density dots. (shown in **Table 2.2**) The mobility for TG-STD devices is only around 3.8 $\text{cm}^2 \text{V}^{-1} \text{s}^{-1}$, which is 8-10 times smaller than the mobility in the intrinsic channel region for TG-NDD devices. The reduction of the effective channel length is not sufficient to explain the enhanced mobility in TG-NDD devices.

Table 2.2 The intrinsic mobility of a-IGZO with 0.2 and 0.8 wt% nano dot doping.

TG-NDD (0.8 wt%)	$L_{\text{total}} (\mu\text{m})$	$L_{\text{int}} (\mu\text{m})$	$\mu (\text{cm}^2 \text{V}^{-1} \text{s}^{-1})$	$\mu_{\text{int}} (\text{cm}^2 \text{V}^{-1} \text{s}^{-1})$
	1000	500	79.2	39.6
TG-NDD (0.2 wt%)	$L_{\text{total}} (\mu\text{m})$	$L_{\text{int}} (\mu\text{m})$	$\mu (\text{cm}^2 \text{V}^{-1} \text{s}^{-1})$	$\mu_{\text{int}} (\text{cm}^2 \text{V}^{-1} \text{s}^{-1})$
	1000	684	47.5	32.5

* L_{int} =intrinsic channel length, μ_{int} =intrinsic mobility

Therefore, we proposed the second reason to explain the enhanced mobility in the intrinsic channel region for TG-NDD devices is the field-induced barrier lowering effect. It is known that the electron transport in a-IGZO is governed by the percolation transport.[16, 17] The random distribution of Ga³⁺ and Zn²⁺ ions in the network structure forms potential barriers around the conduction band and then reduces electron mobility.[18] The potential barrier can be significantly reduced when carrier concentration is increased.[16-18] When high-density conductive dot-like regions are introduced into the intrinsic a-IGZO film, the potential barrier in the intrinsic a-IGZO is lowered by the neighboring high conductive regions. Increasing the dot concentration leads to a more pronounced barrier lowering effect. As a result, when dot density increases from $4.8 \times 10^6 \text{ mm}^{-2}$ to $6.8 \times 10^6 \text{ mm}^{-2}$, the mobility in the intrinsic channel increases from $32.5 \text{ cm}^2 \text{ V}^{-1} \text{ s}^{-1}$ to $39.6 \text{ cm}^2 \text{ V}^{-1} \text{ s}^{-1}$.

The barrier lowering effect is well observed in many semiconductor devices. For example, the Schottky barrier at the metal-organic interface exhibits a Schottky-barrier lowering effect when increasing the doping level of the organic semiconductor.[19] For short-channel MOSFETs, the built-in potential barrier between the heavily-doped source and the bulk suffers from the drain-induced-barrier-lowering effect.[20-22] For poly-Si TFTs, the grain boundary barrier is also lowered by the drain-to-source electric field.[23] Drain-induced barrier lowering effect is also observed in short channel ZnO TFT.[24] The high density dot-like doping in channel region of field-effect transistors was not reported in previous studies. However, in our work, it is believed that the effective potential barrier in the intrinsic a-IGZO surrounded by heavily-doped dots is lowered when the dot density is increased and when the doping level is increased. Since the electron mobility in a-IGZO is exponentially dependent on the minus of the potential barrier height[shown in Eq. 1], the reduction of potential barrier leads to a significant

improvement of the electron mobility. [16, 17]

$$\mu(n) = \mu_o e^{-\phi_{eff}(n)/k_B T}, \phi_{eff} \text{ is effective potential barrier height} \quad (\text{Eq. 1})$$

Also, The transfer characteristics of TG-NDD devices when we repeating the measurement for seven times are shown in **Figure 2.13**. The stability is acceptable. The performance of the devices, however, gradually degrades after several days when stored in ambient. Because the dot-like regions with a large amount of oxygen deficiencies are exposed to the oxygen-rich ambient, the oxygen deficiencies are gradually decreased and the conductivity is reduced. Passivation is required to solve this issue and the related process is currently developed.

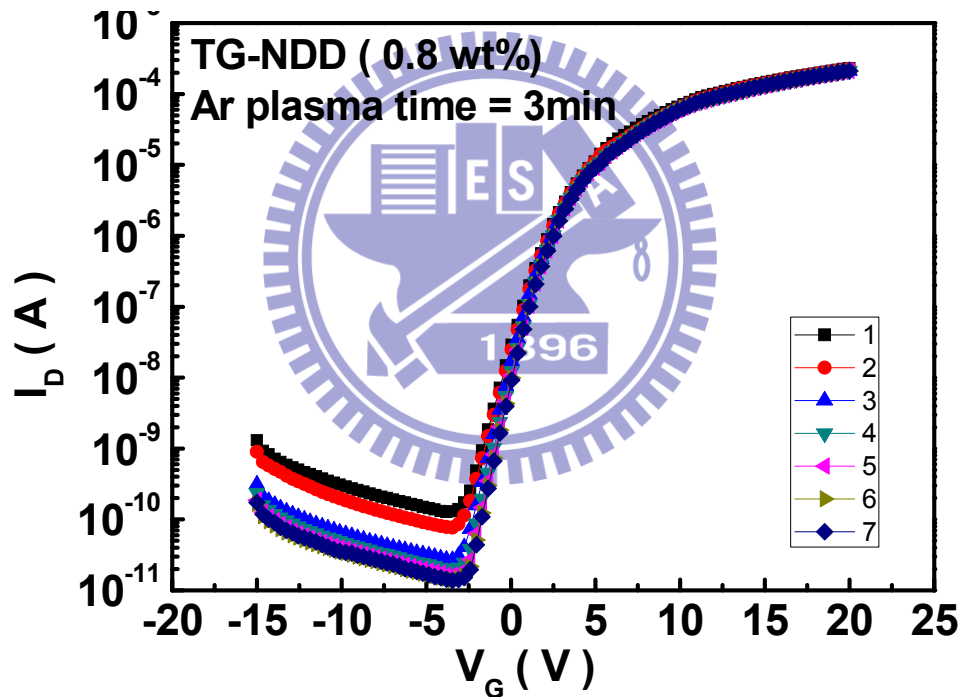


Figure 2.13 The transfer characteristics of TG-NDD devices when we repeating the measurement for seven times.

Finally, the NDD process is utilized on the back interface of conventional bottom-gate (BG) a-IGZO TFTs. The bottom-gate (BG) a-IGZO TFTs with and without NDD are denoted as BG-NDD and BG-STD, respectively. The schematic diagrams of BG-STD and BG-NDD a-IGZO TFTs are shown in **Figures 2.14(a)** and **2.14(b)**, respectively.

For bottom-gate devices, process flow is similar to that shown in **Figure 2.3(a)** except for two differences. The first difference is that the glass substrate is replaced by a heavily-doped silicon substrate capped with a 100 nm silicon nitride. The second is that the top aluminum electrode above the PVP layer is replaced by a thermal-evaporated SiO_x with a thickness of 40 nm. The SiO_x is served as a mask and the PVP without the SiO_x coverage is etched by oxygen plasma. The channel width and length of the bottom gate devices are 1000 μm and 100 μm , respectively. The channel width is defined by the edge of the a-IGZO pattern. For bottom-gate devices (BG-STD and BG-NDD), the channel length is defined by the edge of the source/drain electrodes. Four typical parameters, including threshold voltage (V_{th}), on/off ratio, field-effect mobility (μ), and subthreshold swing ($S.S.$), are extracted and plotted as a function of Ar plasma treatment time, as shown in **Figures 2.14(c)**. For BG-STD devices, when the Ar plasma time increases from 0 sec to 180 sec, the field-effect mobility slightly increases from 10.76 to 15.6 $\text{cm}^2 \text{V}^{-1} \text{s}^{-1}$ and the threshold voltage decreases from 3.7 to -0.42 V. The subthreshold swing and the on/off current ratio are almost unchanged. The decrease of the threshold voltage and the increase of the field-effect mobility after Ar plasma treatment was also reported by Park *et al.* and was explained by the improvement of the contact resistance between the source/drain electrodes and a-IGZO semiconductor. [11]

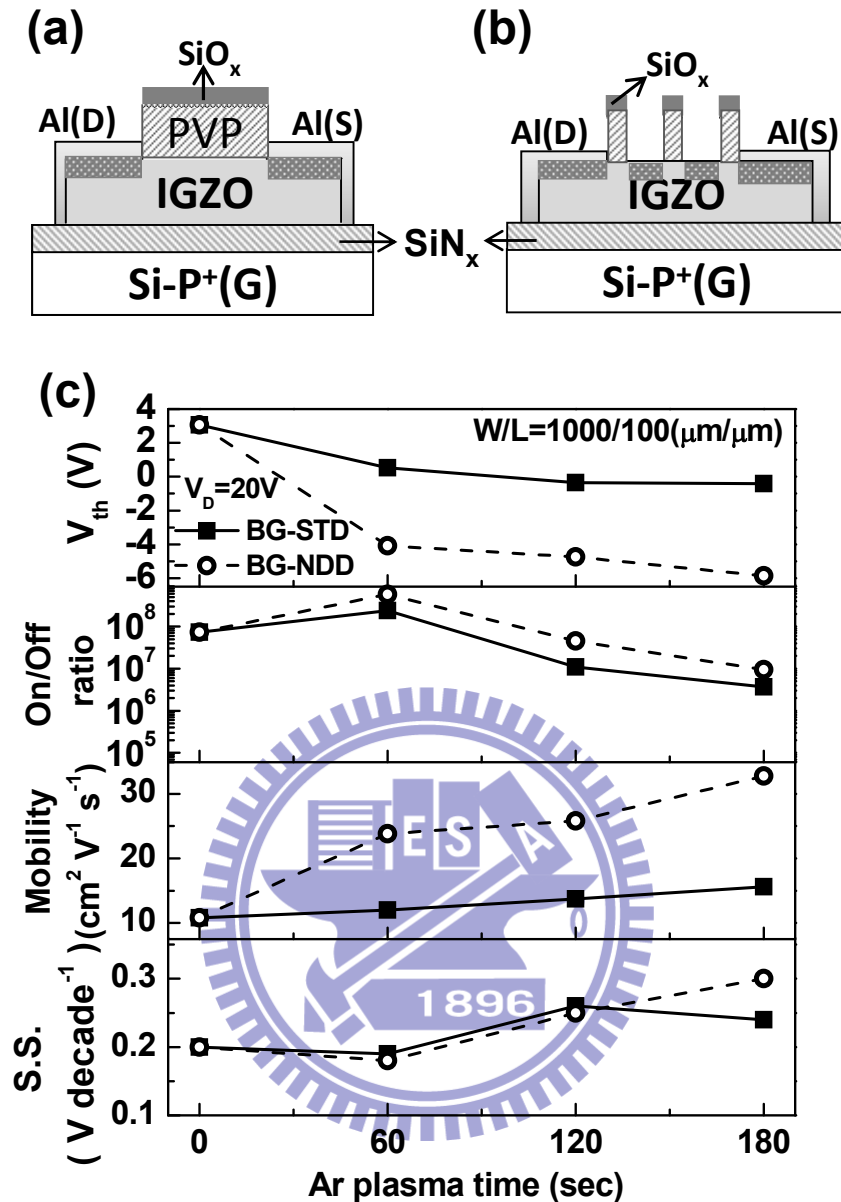


Figure 2.14 The schematic device structures of (a) standard (STD) and (b) nano-dot doping (NDD) bottom gate (BG) a-IGZO TFTs. (c) Four typical parameters (threshold voltage, on/off ratio, mobility, and subthreshold swing) of BG-STD and BG-NDD devices are extracted and plotted as a function of Ar plasma treatment time. Each data point was extracted from the transfer characteristics measured at $V_D = 20$ V. The device channel width is 1000 μm and the channel length is 100 μm .

For BG-NDD devices, when the Ar plasma time increases from 0 sec to 180 s, the field-effect mobility significantly increases from 10.8 to 32.7 $\text{cm}^2 \text{V}^{-1} \text{s}^{-1}$. The threshold voltage decreases from 3.1 to -5.9 V. Also, the parameters is summarized

in **Table 2.3**. The NDD structure influences the electric field distribution in the front channel because the a-IGZO film is only 30 nm thick. As a result, the field-effect mobility is enlarged by NDD treatment due to the reduced effective channel length together with the barrier-lowering-effect. The shift of the threshold voltage is not clearly understood. In our previous report, the removal or the injection of electrons into body region causes a positively-shifted or a negatively-shifted threshold voltage, respectively.[25] When electron concentration in body region is increased, a more negative gate bias is required to deplete the channel. In this work, the dot doping creates localized high electron concentration regions. The three-dimensional potential distribution in channel region is still not clearly investigated. However, the negatively shift of threshold voltage is consistent with the phenomenon reported in our previous work when electrons are injected into back channel by capping calcium/aluminum layer onto the back interface of a bottom-gate a-IGZO TFT.[25]

Table 2.3 Typical parameters of BG-NDD TFTs with and without nano-dot doping.

	<i>BG-STD</i> (Ar treatment 0 sec)	<i>BG-STD</i> (Ar treatment 180 sec)	<i>BG-NDD</i> (Ar treatment 0 sec)	<i>BG-NDD</i> (Ar treatment 180 sec)
V_t (V)	3.10	-0.42	3.10	-5.90
μ_{max}(cm²/Vs)	10.76	15.60	10.80	32.70
S.S.(dec./V)	0.2	0.24	0.2	0.3
On/Off ratio	7.30E+07	3.70E+06	7.30E+07	9.40E+06

2.4. Conclusion

To summarize, this study proposes a top-gate self-aligned a-IGZO TFT with nano-meter-scale dotted channel doping. With a simple, low-cost, and lithography-free process, the effective mobility level of TG a-IGZO TFT becomes 19 times higher than that of the control sample and the maximum effective mobility reaches $79 \text{ cm}^2 \text{ V}^{-1} \text{ s}^{-1}$. If the effective intrinsic channel length is used to estimate the mobility inside the intrinsic a-IGZO region, the maximum intrinsic mobility of TG a-IGZO TFT reaches $39.6 \text{ cm}^2 \text{ V}^{-1} \text{ s}^{-1}$ and increases 10 times than controls (STD). The nano dot doping (NDD) structure reduces the effective channel length and lowers the potential barrier in the intrinsic a-IGZO by the neighboring high conductive regions. Increasing the dot concentration leads to a more pronounced barrier lowering effect. According to the percolation conduction model, the decrease of the potential barrier leads to a significant increase of the field-effect mobility in a-IGZO semiconductor. The high mobility and the self-aligned structure of the proposed a-IGZO TFTs with NDD are promising for the development of low cost circuit-like RFID tags, smart cards, and transparent circuits on windows.

References

- [1] Y. Kwon, Y. Li, Y. W. Heo, M. Jones, P. H. Holloway, D. P. Norton, Z. V. Park, S. Li, “Enhancement-mode thin-film field-effect transistor using phosphorus-doped (Zn, Mg) O channel” *Appl. Phys. Lett.*, 84, 2685. (2004).
- [2] H. Q. Chiang, J. F. Wager, R. L. Hoffman, J. Jeong, D. A. Keszler, “ High mobility transparent thin-film transistors with amorphous zinc tin oxide channel layer” *Appl. Phys. Lett.*, 86, 013503. (2005).
- [3] H. N. Lee, J. Kyung, M. C. Sung, D. Y. Kim, S. K. Kang, S. J. Kim, C. N. Kim, H. G. Kim, S. T. Kim, “ Oxide TFT with multilayer gate insulator for backplane of

- AMOLED device” *J. Soc. Info. Display*, 16, 265-272. (2008).
- [4] C. T. Tsai, T. C. Chang, S. C. Chen, I. Lo, S. W. Tsao, M. C. Hung, J. J. Chang, C. Y. Wu, C. Y. Huang, “Influence of positive bias stress on N₂O plasma improved InGaZnO thin film transistor” *Appl. Phys. Lett.*, 96, 242105. (2010).
- [5] H. Seo, Y. J. Cho, J. Kim, S. M. Bobade, K. Y. Park, J. Le, D. K. Choi, “Permanent optical doping of amorphous metal oxide semiconductors by deep ultraviolet irradiation at room temperature” *Appl. Phys. Lett.*, 96, 222101. (2010).
- [6] W. Lim, E. A. Douglas, S. H. Kim, D. P. Norton, S. J. Pearton, F. Ren, H. Shen, W. H. Chang, “High mobility InGaZnO₄ thin-film transistors on paper” *Appl. Phys. Lett.*, 94, 072103. (2009).
- [7] S.H. Ju, A. Facchetti, Y. Xuan, J. Liu, F. Ishikawa, P. Ye, C. Zhou, T.J. Marks, and D.B. Janes, “Fabrication of fully transparent nanowire transistors for transparent and flexible electronics” *Nature Nanotech.* **2007**, 2, 378-384.
- [8] P. C. Chang, Z. Fan, C. J. Chien, D. Stichtenoth, C. Ronning, J. G. Lua, “High-performance ZnO nanowire field effect transistors” *Appl. Phys. Lett.*, 89, 133113. (2006).
- [9] F. Liu, M. Bao, K. L. Wang, C. Li, C. Zhou, “One-dimensional transport of In₂O₃ nanowires” *Appl. Phys. Lett.*, 86, 213101. (2005).
- [10] S. Jeong, T. G. Ha, J. Moon, A. Facchetti, and T. J. Marks, “Role of Gallium Doping in Dramatically Lowering Amorphous-Oxide Processing Temperatures for Solution-Derived Indium Zinc Oxide Thin-Film Transistors” *Adv. Mater.*, 22, 1346-1350, (2010).
- [11] J. S. Park, J. K. Jeong, Y. G. Mo, H. D. Kim, S. I. Kim, “Improvements in the device characteristics of amorphous indium gallium zinc oxide thin-film transistors by Ar plasma treatment” *Appl. Phys. Lett.*, 90, 262106. (2007).
- [12] K. Nomura, A. Takagi, T. Kamiya, H. Ohta, M. Hirano, H. Hosono, “Amorphous

oxide semiconductors for high-performance flexible thin-film transistors” *Jpn. J. Appl. Phys.*, 45, 4303-4308. (2006).

[13]K. Okamura, D. Nikolova, N. Mechau, and H. Hahn, “ Appropriate choice of channel ratio in thin-film transistors for the exact determination of field-effect mobility”*Appl. Phys. Lett.*, 94, 183503. (2009).

[14]S. I. Kim, C. J. Kim, J. C. Park, I. Song, S. W. Kim, H. Yin, E. Lee, J. C. Lee, Y. Park,“ High performance oxide thin film transistors with double active layers” *IEDM Tech. Dig.*, 1-4. (2008).

[15]C. J. Chiu, S. P. Chang, S. J. Chang, “High-Performance a-IGZO Thin-Film Transistor Using Ta₂O₅ Gate Dielectric” *IEEE Electron Device Lett.*, 31, 1245. (2010).

[16]A. Takagia, K. Nomura, H. Ohta, H. Yanagi, T. Kamiya, M. Hirano, H. Hosono, “Carrier transport and electronic structure in amorphous oxide semiconductor, a-InGaZnO₄” *Thin Solid Films*, 486, 38-41. (2005).

[17]K. Nomura, H. Ohta, A. Takagi, T. Kamiya, M. Hirano, H. Hosono, “Room-temperature fabrication of transparent flexible thin-film transistors using amorphous oxide semiconductors” *Nature*, 432, 488. (2004).

[18]K. Nomura, T. Kamiya, H. Ohta, K. Ueda, M. Hirano, and H. Hosono, “Carrier transport in transparent oxide semiconductor with intrinsic structural randomness probed using single-crystalline InGaO (ZnO) films” *Appl. Phys. Lett.* 85, 11, (2004).

[19]E.J. Lous, P.W.M. Blom, L.W. Molenkamp, and D.M. de Leeuw, “Schottky contacts on a highly doped organic semiconductor” *Phys. Rev. B*, 51, 23, (1995).

[20]Y. Taur and T. H. Ning, *Fundamentals of Modern VLSI Devices* (Cambridge University Press, Cambridge, (1998.))

- [21]L. D. Yau, "A simple theory to predict the threshold voltage of short-channel IGFET's" *Solid-State Electron.*, 17, 1059. (1974).
- [22]Y. Taur, G. J. Hu, R. H. Dennard, L. M. Terman, C. Y. Ting, and K. E. Petrillo, "A self-aligned 1- μ m-channel CMOS technology with retrograde n-well and thin epitaxy" *IEEE Trans. Electron Devices*, ED-32, 203-209. (1985).
- [23]W. J. Wu and R. H. Yao, "A Simple Model of DIGBL Effect for Polysilicon Films and Polysilicon Thin-Film Transistors" *IEEE Electron Device Lett.*, 29, 1128-1131. (2008).
- [24]H. H. Hsieh and C. C. Wu, "Scaling behavior of ZnO transparent thin-film transistors" *Appl. Phys. Lett.*, 89, 041109. (2006).
- [25]H. W. Zan, W. T. Chen, C. C. Yeh, H. W. Hsueh, C. C. Tsai, and H. F. Meng, "Dual gate indium-gallium-zinc-oxide thin film transistor with an unisolated floating metal gate for threshold voltage modulation and mobility enhancement" *Appl. Phys. Lett.* 98, 153506, (2011)

Chapter 3. Increasing Organic Vertical Carrier Mobility for the Application of High Speed Bilayered Organic Photodetector

3.1. Introduction

Organic electronics has drawn lots of interest due to their low fabrication temperature on a variety of low-cost flexible substrates, thereby enabling the development of organic photonic integrated circuit, organic sensor array, organic photocouplers, or organic imaging sheets. For these applications, high speed organic photodetectors (PDs) are usually required. In organic PDs, photo detection is via the dissociation of photogenerated excitons at the interface between a donor-like material and an acceptor-like material. The performance of a PD is determined by the efficiency of charge generation and charge transport. The quantum efficiency of a PD can be enhanced by creating a bulk heterojunction, while the charge transport property can be improved by utilizing high mobility materials. However, the influence of carrier mobility on the PD response speed was never been clearly discussed. The frequency response of organic PDs is also rarely studied. Only a few reports demonstrated the frequency response of organic PDs.[1-3] The highest operation frequency (~430 MHz) of organic multilayer PDs was reported by using ultra-high-vacuum (1×10^{-10} torr) organic molecular-beam deposition (OMBD) to control the thickness of an individual layer as 0.5 nm to enable carrier tunneling.[1] When a conventional high-vacuum (5×10^{-7} to 1×10^{-6} torr) deposition system is used, a multilayered PD was reported to exhibit a bandwidth from a few kHz to a few MHz under a operation voltage as 1 to 5 volts and have a small incident photon to current

conversion efficiency (IPCE) as 0.02% [2]. Another report used a bilayered structure to demonstrate a bandwidth as 70 MHz under a 7-volts operation while the peak IPCE is around 7% [3]. In these studies, even high frequency responses are demonstrated, factors associated with organic materials to influence frequency response are not discussed. For a bilayered organic PD, response speed may be influenced by the separation of exciton, the carrier mobility, the multiple trapping and releasing procedure, the interface trapping, the RC delay due to the PD structure, etc. In this study, experiments are designed to show that the vertical carrier mobility is the dominant factor to influences the response speed of bilayered organic PDs. The influence of microstructure of organic film on the vertical carrier mobility is also explored. By utilizing commonly used organic molecules such as fullerene (C60) and pentacene, we proposed that the key to increase the speed of organic PD is to use materials with high vertical carrier mobility. A clear dependence between vertical carrier mobility and the frequency response of organic diodes and of organic PDs is verified. With C60 as the acceptor material, using high mobility pentacene in stead of poly(3-hexylthiophene) (P3HT) to serve as the hole transport layer effectively improves the hole mobility over 1 orders and hence enlarges the operation bandwidth to be 80 MHz under a 4-volts operation. The influence of deposition rate on the vertical mobility of pentacene film grown on poly (3,4-ethylenedioxythiophene):poly (styrenesulfonate) (PEDOT:PSS) is also discussed for the first time.

3.2. Experiment

3.2.1. Device Fabrication Process

Schematic cross sectional view of the bilayered PD is shown in the inset of **Figure 3.1.**

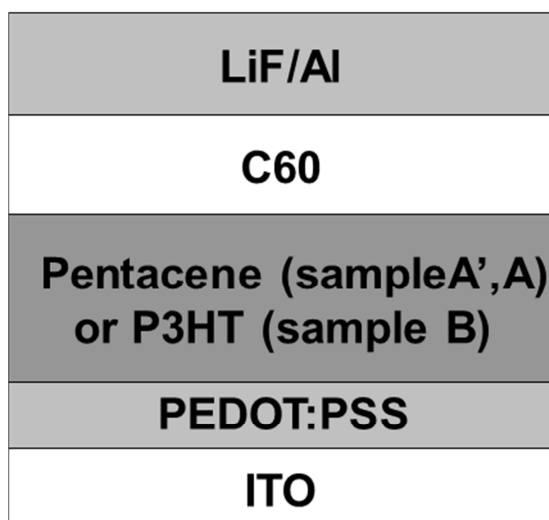


Figure 3.1 Schematic device structure of the bilayered photodetector. The device anode and cathode is ITO:PEDOT and LiF/Al, respectively.

For the PDs with structure as **ITO/PEDOT:PSS/pentacene/C60/LiF/Al**, the device made from pentacene deposited at high deposition rate (1 Å/s) is referred to Sample A (1 Å/s) while the device made from pentacene deposited at low deposition rate (0.1 Å/s) is referred to Sample A' (0.1 Å/s). Sample B represents the PD with structure **ITO/PEDOT:PSS/P3HT/C60/LiF/Al**.

The PD structures were fabricated on precleaned indium–tin oxide (ITO) glass substrate with a layer of 200 Å PEDOT:PSS. The steps of clean ITO substrate is shown follow:

Steps:

- (1) De Ion (DI) water current flows for 5 minutes in order to remove the particles.
- (2) The substrates should be placed under the in the acetone and ultrasonic resonance for 5 minutes in order to remove the organic pollution. Then, the substrates have to put under the DI water current flow for 5 minutes in order to remove the solvent.
- (4) The substrates were put in the KG detergent bath with ultrasonic resonance for 5

minutes in order to remove the particles, fingerprint, and ionic.

(5) The substrates were put under the DI water current flow for 5 minutes in order to remove the solvent.

(6) Finally, the substrates would be dried with dry N_2 flow to blow off the water on the substrates.

The 200 Å PEDOT :PSS (AI 4083) was spin coated on the ITO and annealed at 200°C for 15 min. Then, the substrate with anode was already prepared. To investigate the influence of hole mobility on the response speed, pentacene and poly(3-hexylthiophene) (P3HT) with identical thickness were used as donor materials and C60 was used as acceptor layer, respectively.

1. P3HT:

P3HT was spin coated on PEDOT:PSS from toluene (1.5 wt %, 1500rpm) and annealed at 200 °C for 10min. After we spin coated the P3HT film, we use acetone to clean the unnecessary area. Then, a thin P3HT layer of about 1000 Å was obtained.

2. Pentacene

The pentacene material obtained from *Aldrich* without any purification was directly placed in the thermal coater for the deposition. Pentacene (0.1 Å/s or 1 Å/s) was deposited by thermal evaporation through shadow mask at a pressure as 1×10^{-6} torr at room temperature. The thickness of the donor and acceptor was 1000 Å.

3. C60

The C60 was directly placed in the thermal coater for the deposition. The deposition was started at the pressure around 3×10^{-6} torr. The 50-nm-thick C60 was deposited by thermal evaporation at a deposition rate of 1Å/s. The active region was defined by shadow mask. Then, the samples were transferred to deposit the cathode of LiF(10 Å)/Al(1000 Å). All the fabrication processes were in glove box to immune the

influence of water vapor and oxygen. The active region of the PDs was 4 mm^2 . The devices are encapsulated by glass cap with UV glue in a glove box, and measured in ambient condition.

3.2.2. Measurement Instrument

For transient response measurement, the laser diode with a wavelength as 633 nm (U-LD-650541A/B, Union Optronics Corp.) is used to trigger samples. The photocurrent from the PD was measured by using a Femto DHPCA-100 trans-impedance amplifier (TIA) and the output signal is displayed on a digital oscilloscope (Gwinstek). Atomic force microscope (AFM) images were measured in tapping mode by Dimension 3100, Digital Instrument. The J - V curve was measured by using a HP-4156 or HP-5270 instrument.

3.3. Results and Discussions

The energy band diagrams of sample A and sample B are shown in **Figure 3.2**, while the incident photon-to-electron conversion efficiency (IPCE) of sample A and sample B under reverse voltage biases are compared in **Figure 3.3**. The IPCE of sample A achieves 24 % at 580 nm at a reverse bias of 10 V and remains 10.1 % at 690 nm. As for sample B, the IPCE is around 45-50 % at a reverse bias of 10 V in the range from 420 nm to 620 nm. A sharply decrease in IPCE start at 620 nm and the IPCE lower than 10 % is observed over 650 nm. Sample A absorbs more effectively than sample B in the range from 650 nm to 690 nm. This results from the difference in absorption spectra of pentacene and P3HT as shown in **Figure 3.4**. Changing pentacene deposition rate has no significant influence on IPCE curves or on absorption spectrum.

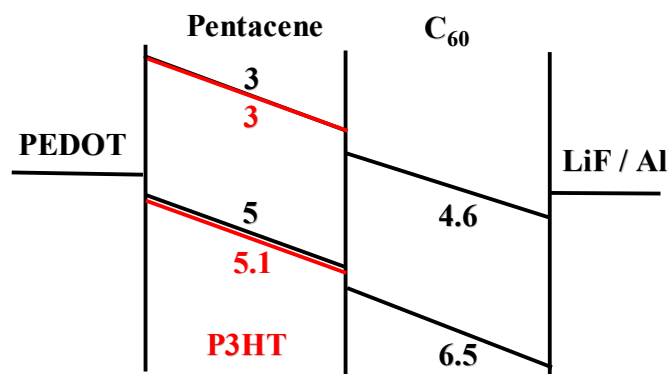


Figure 3.2 The energy band diagrams of sample A and sample B under reverse voltage biases. The voltage biases is 0, -5, and -10V. The device anode and cathode is ITO:PEDOT and LiF/Al, respectively.

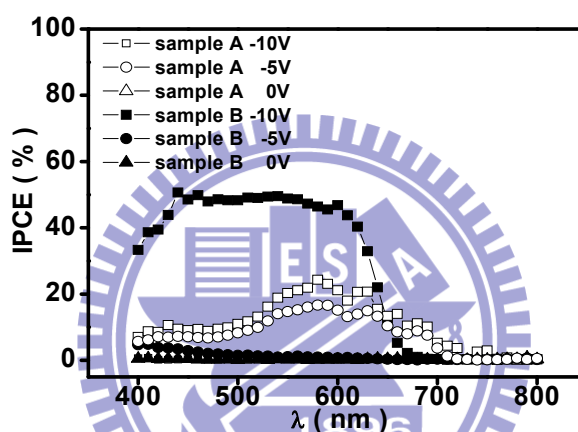


Figure 3.3 The incident photon-to-electron conversion efficiency of sample A and sample B under various reverse voltage biases. The voltage biases is 0, -5, and -10V. The device anode and cathode is ITO:PEDOT and LiF/Al, respectively.

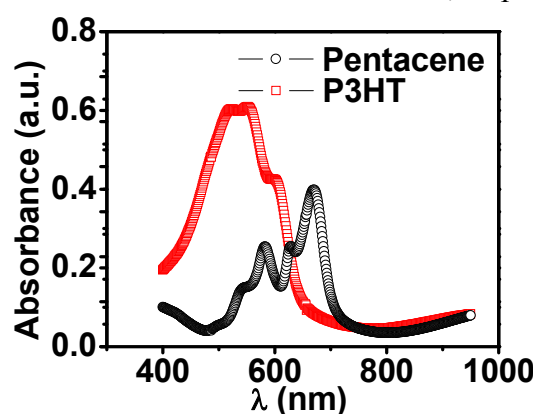


Figure 3.4 The absorption spectra of pentacene and P3HT. The thickness of pentacene and P3HT is 100 nm.

As a first step to understand the influence of the mobility on the frequency response of PD, the vertical carrier mobility of C60 and pentacene are extracted from the space-charged-limited current of organic diodes [4]. **Figure 3.5** compares the current density - voltage characteristics of organic diodes with C60, P3HT, pentacene deposited at 0.1 Å/s, and pentacene deposited at 1 Å/s. The thickness of organic layer is fixed as 180 nm. The vertical carrier mobility is $1.9 \times 10^{-3} \text{ cm}^2/\text{Vs}$, $6.0 \times 10^{-5} \text{ cm}^2/\text{Vs}$, $2.3 \times 10^{-5} \text{ cm}^2/\text{Vs}$, and $2.8 \times 10^{-4} \text{ cm}^2/\text{Vs}$ for C60, P3HT, pentacene (0.1 Å/s), and pentacene (1 Å/s), respectively. The carrier mobility in C60 is much higher than that in P3HT or in pentacene, implying that the response bottleneck in organic PDs is usually in donor material rather than in acceptor material. Hence, it is essential to obtain high vertical hole mobility in donor material.

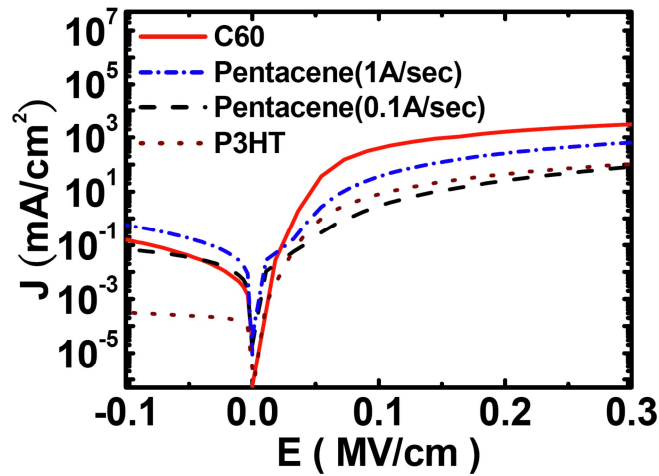


Figure 3.5 The current density–voltage characteristics of organic diodes with C60, P3HT, pentacene deposited at 0.1 Å/s, and pentacene deposited at 1 Å/s. The thickness of acceptor layer and donor layer is 50 nm and 100 nm, respectively. The device anode and cathode is ITO:PEDOT and LiF/Al, respectively.

To demonstrate the influence of vertical hole mobility on the electrical frequency response of the diode, the frequency responses of P3HT diodes and pentacene diodes measured in a rectifier circuit are compared in **Figure 3.6**.

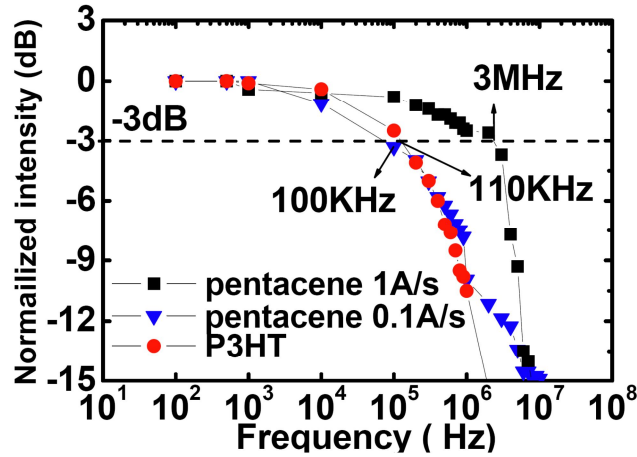


Figure 3.6 The electrical frequency responses of pentacene diodes and P3HT diode. Characteristics of diodes made by pentacene films deposited at different deposition rate are compared. A function generator (8110A Pulse Pattern Generator, Agilent) is used to supply the ac input signals. A capacitor as $0.1 \mu\text{F}$ and the internal resistance of the oscilloscope as $10 \text{ M}\Omega$ are used as the load capacitor and the load resistance in the rectifier circuit.

A function generator (8110A Pulse Pattern Generator, Agilent) is used to supply the ac input signals. A capacitor as $0.1 \mu\text{F}$ and the internal resistance of the oscilloscope as $10 \text{ M}\Omega$ are used as the load capacitor and the load resistance in the rectifier circuit [5]. The rectifier circuit diagram is shown in **Figure 3.7**. The high hole mobility in pentacene (1 \AA/s) contributes to a large bandwidth as 3 MHz while the low hole mobilities in P3HT and pentacene (0.1 \AA/s) make the P3HT and pentacene (1 \AA/s) diodes lose their rectifying ability at a frequency about 100 kHz.

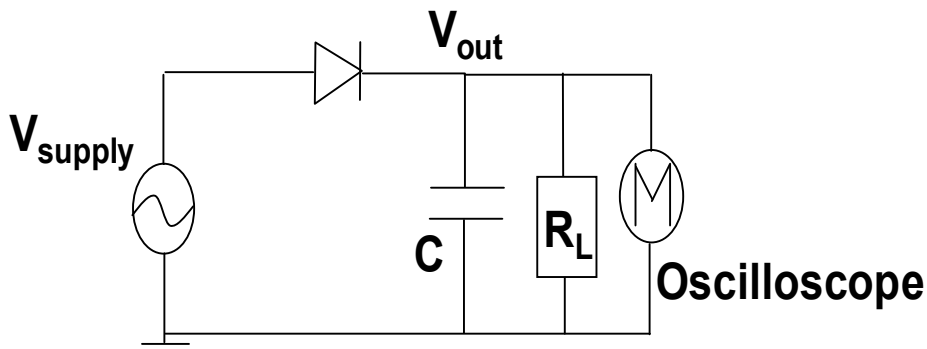


Figure 3.7 The rectifier circuit. A function generator (8110A Pulse Pattern Generator,

Agilent) is used to supply the ac input signals. A capacitor as 0.1 μF and the internal resistance of the oscilloscope as 10 $\text{M}\Omega$ are used as the load capacitor and the load resistance in the rectifier circuit.

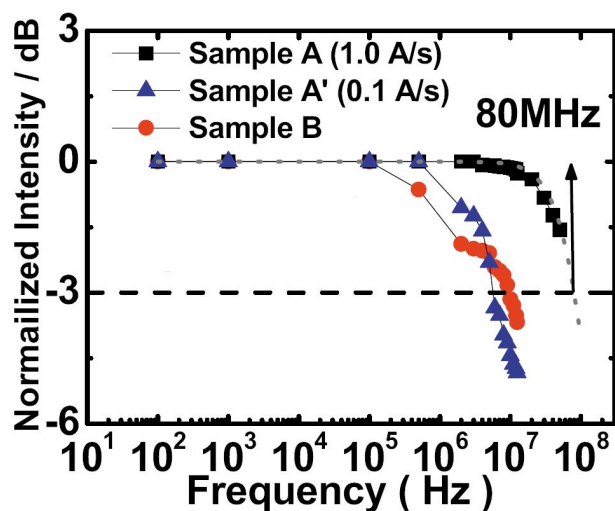


Figure 3.8 The frequency characteristics of PDs made by pentacene and P3HT. Characteristics of PDs made by pentacene films deposited at different deposition rate are compared. The gray dotted line is calculated following $P=P_0 / (1 + f / f_c)$. The thickness of acceptor layer and donor layer is 50 nm and 100 nm, respectively. The device anode and cathode is ITO:PEDOT and LiF/Al, respectively.

Then, the frequency responses of PDs (Samples A, A' and B) are compared in **Figure 3.8** by plotting the normalized output amplitude versus the frequency of the input signal varies from 100 Hz to 50-MHz.

The schematic measurement setup is shown in **Figure 3.9**. The input signal is the light generated by a laser diode with a wavelength as 633 nm. The laser diode is switched on and off by a square-wave voltage signal with different frequencies. Samples are reverse-biased at 4 volts during measurement.

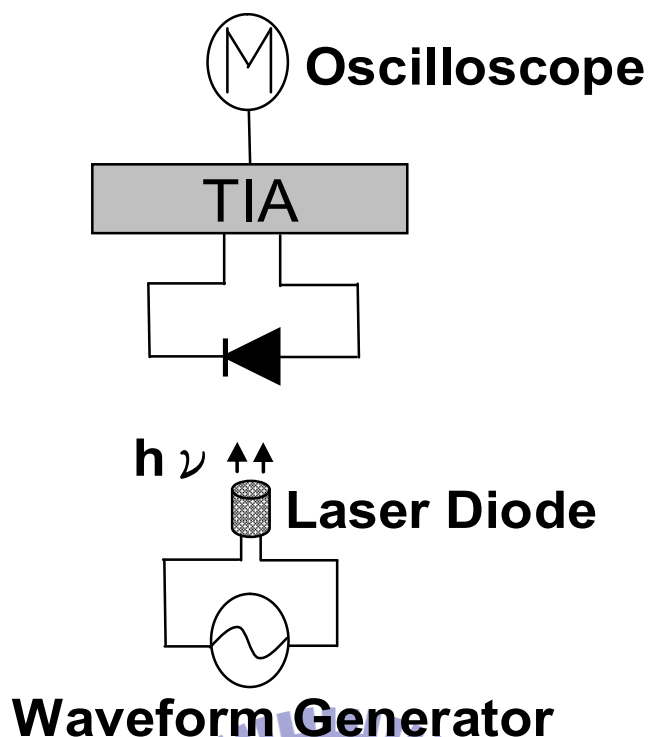


Figure 3.9 The schematic measurement setup. The input signal is the light generated by a laser diode with a wavelength as 633 nm. The laser diode is switched on and off by a square-wave voltage signal with different frequencies. For transient response measurement, the laser diode with a wavelength as 633 nm (U-LD-650541A/B, Union Optronics Corp.) is used to trigger samples. The photocurrent from the PD was measured by using a Femto DHP-100 trans-impedance amplifier (TIA) and the output signal is displayed on a digital oscilloscope (Gwinstek).

It is found that the frequency response of Sample B is similar to that of Sample A' (0.1 Å/s) while Sample A (1 Å/s) follows the input signal well even under a 50-MHz light switching. Though the pulse generator in our experiment has a frequency limitation of 60 MHz, the bandwidth of Sample A can be estimated by fitting the experimental data with the basic transfer function of a single-time-constant low-pass amplifier [3, 6]. The dashed line in **Figure 3.8** represents the calculated normalized output power intensity as a function of frequency. A 80-MHz bandwidth can be expected for Sample A under a 4-volts operation.

As aforementioned, the response bottleneck is in the donor material. Our results

reveal a significant influence of pentacene deposition rate on the vertical hole mobility and on the PD bandwidth. For pentacene grown on PEDOT:PSS, it is reported that a deposition rate higher than 3 Å/s leads to high nucleation sites and small grain size [7]. In our experiment, the AFM images of 100-nm-thick pentacene films deposited at 0.1 Å/s or 1 Å/s on PEDOT:PSS are shown in **Figure 3.10(a)** and **3.10(b)**, respectively. Grain size and grain structure of these two images are similar to each other. Thin-film X-ray diffraction patterns of these two samples (shown in **Figure 3.11**) are also almost identical. It is therefore speculated that the deposition rate (0.1 Å/s or 1 Å/s) has no significant influence on pentacene bulk region. The difference in the initial growth stage may play an crucial role to influence the observed vertical hole mobility. To verify the speculation, we compares the AFM images of 1.5-nm-thick pentacene films deposited at 0.1 Å/s or 1 Å/s on PEDOT:PSS as shown in **Figure 3.10(c)** and **3.10(d)**, respectively. The AFM images of 3-nm-thick pentacene films deposited at 0.1 Å/s or 1 Å/s on PEDOT:PSS are also shown in **Figure 3.10(e)** and **3.10(f)**. As shown in **Figure 3.10(f)**, the 3-nm-thick pentacene deposited at 1 Å/s on PEDOT:PSS starts to develop dendritic structures. The 3-nm-thick pentacene film deposited at 0.1 Å/s on PEDOT:PSS as shown in **Figure 3.10(e)**, however, has no clear grain structure yet.

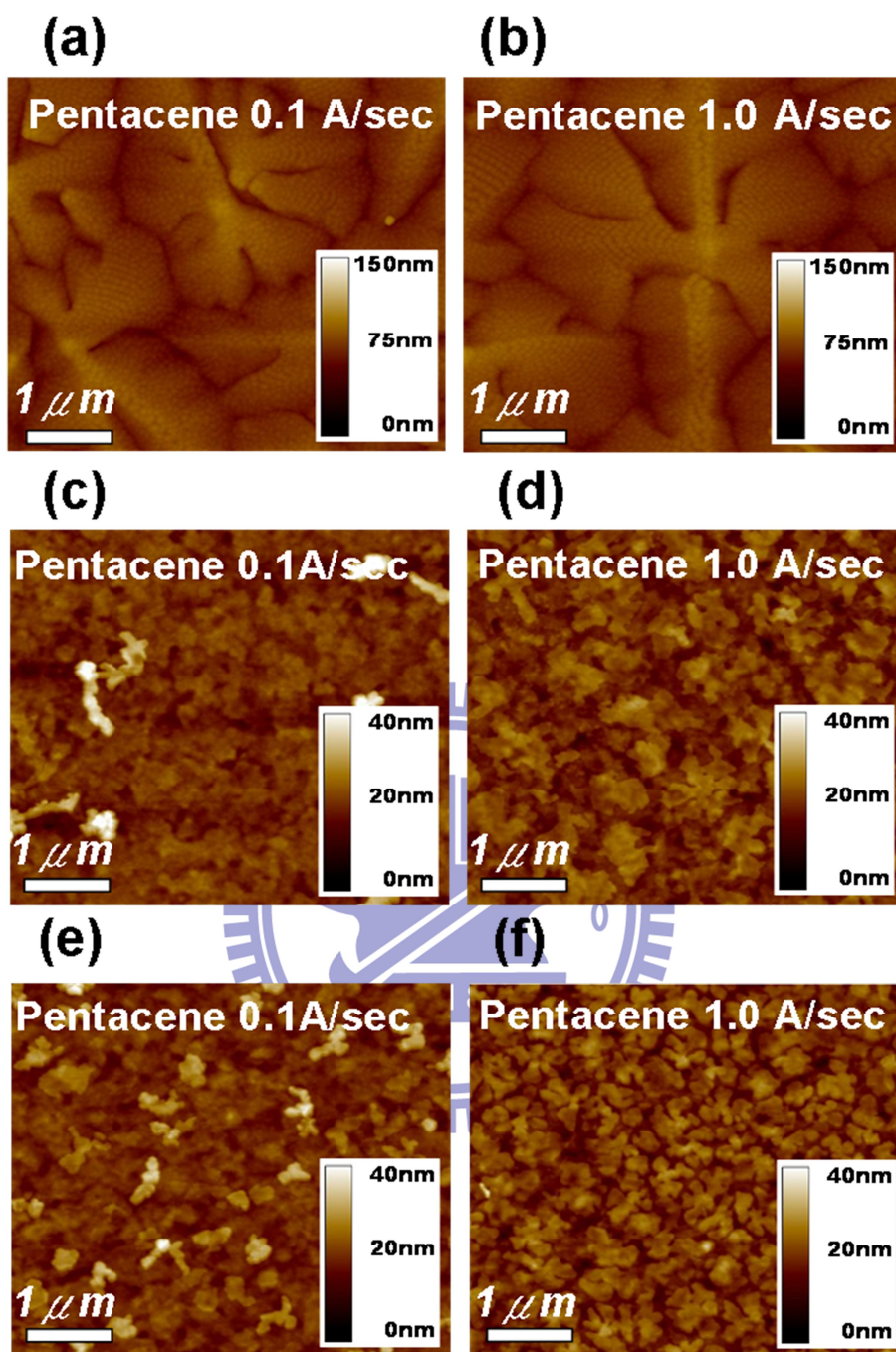


Figure 3.10 AFM images of 100 nm, 1.5 nm, and 3 nm pentacene films deposited at (a) 0.1 Å/s and (b) 1 Å/s, (c) 0.1 Å/s and (d) 1 Å/s, and (e) 0.1 Å/s and (f) 1 Å/s on PEDOT:PSS covered ITO glass, respectively.

Since the PEDOT:PSS exhibits a hydrophilic surface, it is proposed that pentacene grown on PEDOT:PSS follows “layer-plus-island” (Stranski-Krastanov) mode [8]. When pentacene molecules arrive on PEDOT:PSS, they rearrange and pack to form

two-dimensional islands due to the strong interaction between pentacene molecules and substrate.

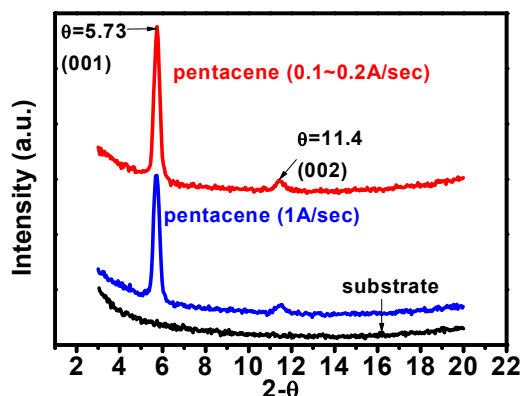


Figure 3.11 X-ray diffraction (XRD) pattern of pentacene deposited on ITO surface. The thickness of pentacene thin films deposited on ITO surface are 100 nm.

After the formation of the first few monolayers to cover the substrate, pentacene growth mode turns to the island mode that forms three-dimensional islands when the interaction between pentacene molecules is stronger than the interaction between pentacene and substrate. Decreasing the deposition rate may reduce the surface coverage [9]. Because low deposition rate creates low nucleus density, molecules have to diffuse a larger distance to be incorporated into islands, hence have a larger possibility of being desorbed. As a result, in our study, lower deposition rate retards the formation of three-dimensional islands. On the other hand, pentacene deposited at 1 Å/s on PEDOT:PSS exhibits more three-dimensional islands, leading to the improvement of film order in the vertical direction and the increase of vertical mobility.

3.4. Conclusion

In summary, we report a direct influence of the vertical carrier mobility on the response speed of organic PDs. By using C60 as the acceptor material and

pentacene with high deposition rate as the donor material, a high-speed bilayered organic PD is demonstrated for the detection of very-high-frequency (VHF, > 30MHz) light switching signals. The influence of deposition rate on the vertical hole mobility of pentacene on PEDOT:PSS is investigated and explained. The VHF organic PDs facilitate the development of the next-generation information technologies.

References

- [1] P. Peumans, V. Bulovic, and S. R. Forrest, "Efficient photon harvesting at high optical intensities in ultrathin organic double-heterostructure photovoltaic diodes" *Appl. Phys. Lett.* **76**, 3855 (2000).
- [2] M. Kaneko, T. Taneda, T. Tsukagawa, H. Kajii, and Y. Ohmori, "Fast Response of Organic Photodetectors Utilizing Multilayered Metal-Phthalocyanine Thin Films" *Jpn. J. Appl. Phys.* **42**, 2523 (2003).
- [3] T. Morimune, H. Kajii, and Y. Ohmori, "Photoresponse properties of a high-speed organic photodetector based on copper-phthalocyanine under red light illumination" *IEEE Photonic Tech. Lett.* **18**, 2662 (2006).
- [4] C. Goh, R. J. Kline, M. D. McGehee, E. N. Kadnikova, and J. M. J. Fréchet, "Molecular-weight-dependent mobilities in regioregular poly (3-hexyl-thiophene) diodes" *Appl. Phys. Lett.* **86**, 122110 (2005).
- [5] Y. Ai, S. Gowrisanker, H. Jia, I. Trachtenberg, E. Vogel, R. M. Wallace, B. E. Gnade, R. Barnett, H. Stiegler, and H. Edwards, "14 MHz organic diodes fabricated using photolithographic processes" *Appl. Phys. Lett.* **90**, 262105 (2007).
- [6] A. S. Sedra and K. C. Smith, "Microelectronic Circuits" 4th ed. Oxford University Press, New York (1998).
- [7] J. Yang, T. Q. Nguyen, "Effects of thin film processing on pentacene/C60 bilayer

solar cell performance” *Organic Electron.* **8**, 566 (2007).

[8] R. Ruiz, D. Choudhary, B. Nickel, T. Toccoli, K. C. Chang, A. C. Mayer, P. Clancy, J. M. Blakely, R. L. Hearick, S. Iannotta, and G. G. Malliaras, “Pentacene thin film growth” *Chem Mater.* **16**, 4497 (2004).

[9] S. Pratontep, M. Brinkmann, F. Nüesch, and L. Zuppiroli, “Correlated growth in ultrathin pentacene films on silicon oxide: Effect of deposition rate” *Phys. Rev. B* **69**, 165201 (2004).



Chapter 4. Vertical Polymer Phototransistor featuring

Photomultiplication due to Base-field Shielding

4.1. Introduction

Organic photodetector arrays can be fabricated at low temperatures on a large scale, with low production costs. The integration of organic photodetectors and other organic electronic devices such as organic transistors, organic light-emitting diodes, and various sensors enables the development of numerous devices, including flexible touch panel displays, flexible large-area scanners, footprint scanners, proximity sensors, biomedical sensors, to name a few.[1~3]

A good photodetector requires high photoresponsivity, low operational voltage, wide bandwidth, and processes that are compatible with organic transistors, should one desire an active-matrix photodetection array. The term photodetectors generally refers to two classes of organic devices. The first class refers to an organic photodiode (OPD) with a vertical metal/semiconducting/metal structure. The semiconducting layer is generally a blend of a donor material with an acceptor material to absorb light and dissociate excitons. OPDs can usually be operated at low voltages (< 5 V) with wide bandwidths (over 80 MHz).[4,5] Unfortunately, the processes involved in the fabrication of vertical structures are incompatible with the process of forming conventional horizontal organic thin-film transistor (OTFT). The second class of photodetector refers to organic phototransistors (OPT) based on an OTFT structure. The photodetection mechanism is based on the shift of threshold voltage due to the formation of a charged state in the organic semiconducting layer or at the semiconductor/dielectric interface under light irradiation.[6] OPTs exhibit high photoresponsivity (> 10 A/W), but usually require high operating voltage (> 10 V).[3]

In this research, we propose a new vertical OPT based on space-charge limited transistors (SCLT).[7] This SCLT-based OPT utilizes a new photo detecting mechanism referred to as the base-field shielding to induce photomultiplication (PM). The effects of PM in organic semiconducting devices has been reported by several research teams.[8,9] In 2007, Jinsong Huang and Yang Yang suggested that PM was due to photo-induced carrier injection.[10] In SCLT-based OPT, we first observed a new effect of PM that was not only related to photo-induced carrier injection but was also greatly enhanced by the effects of base-field shielding. To enhance the effect of base-field shielding, we exchanged the channel material from a donor material, poly(3-hexylthiophene) (P3HT), to a blend of a donor material and an acceptor material, P3HT blended with (6,6)-phenyl-C61-butyric acid methyl ester (PCBM), to enhance the dissociation of excitons. The SCLT-based OPT and P3HT blended with PCBM channel material demonstrated high EQE (approximately 358 %), high photo-to-dark current ratio (approximately 2000), low operational voltage (-1.5 volts) and positive transistor characteristics with an initial on/off current ratio as high as 5000 for single devices.

4.2. Experiment

4.2.1. Device Fabrication process

The structure of the device is shown in **Figure 4.1**.

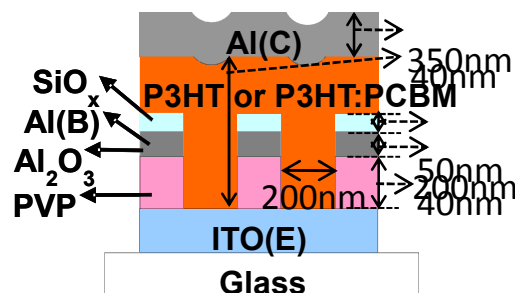


Figure 4.1 Schematic illustration of the structure of P3HT or P3HT:PCBM-SCLT.

P3HT or P3HT blended with PCBM was used as the polymer semiconducting material. The SCLT-based OPT was fabricated on a pre-cleaned ITO glass substrate that had been flattened by 150 W O₂ plasma for 30 min.

The ITO substrate resistance is determined $< 7 \Omega$ and the pattern of emitter is shown in **Figure 4.2**. Firstly, we divide ITO glass into 3×3 cm² square, and clean by soap, acetone, IPA solution each by each in ultra sonic for 20 minutes. Then, we use amount DI water to remove leftover solution, and dry by N₂ air. The processes for patterning the emitter is as following.

1. The clean ITO glasses were put on 170°C hotplate for 5 minutes to remove the residual moisture, and stuck the negative photoresistor (PR) onto the glasses.
2. Next step is using UV lithography through defined shadow mask for 32 seconds.
3. The ITO is immersed in prepared K₂CO₃ solution and then cleaned by DI water.
4. Removing the ITO without coverage the PR and etching by 50°C HCl solution.
5. Finally, the PR is removed by NaOH solution, and the defined ITO pattern is cleaned by DI water.

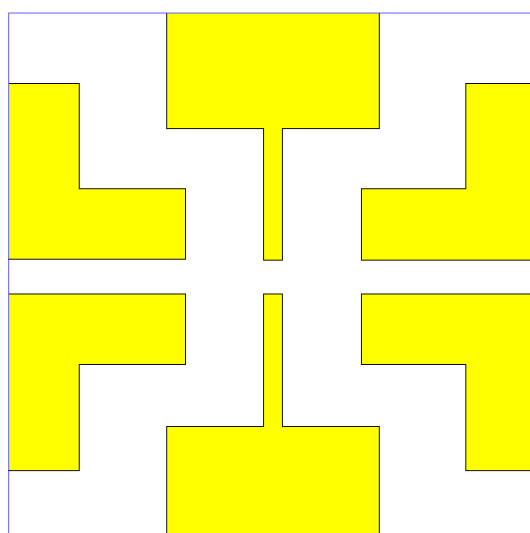


Figure 4.2 The defined emitter pattern with the ITO electrode.

A layer of (2000 Å) cross-linkable poly(4-vinyl phenol) (PVP) was spin coated onto the ITO substrate, and cross-linked at 200°C for 60 min in a glove box environment. Poly (melamine-co-formaldehyde) methylated (Aldrich, Mw~511) was used as a crosslinking agent for the PVP. The schematic structure of PVP and PMF is shown in **Figure 4.3**.

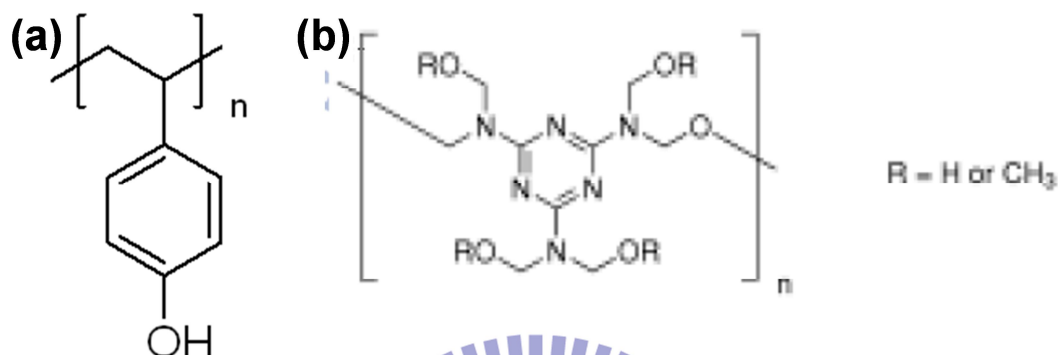


Figure 4.3 The chemical structure of insulator (a) PVP (poly(4-vinylphenol)) cross-linked with (b) PMF (poly(melamine-co-formaldehyde) methylated).

The surface of the PVP was made hydrophilic by short time exposure to 50 W O₂ plasma before the substrate was submerged in a dilute ethanol solution containing 0.8 wt % positively charged polystyrene spheres (Merck, K6-020). The polystyrene spheres were 200 nm in diameter, and were adsorbed by the surface of the PVP to serve as a shadow mask. After submerging the substrate for 3 min in the solution of polystyrene spheres, the substrate was transferred to a beaker with boiling isopropanolic (IPA) solution for 10 sec to avoid the accumulation of PS spheres.[11] The substrate was immediately blown dry to form two-dimensional colloidal arrays. Al and SiO_x was evaporated to a thicknesses of 400 Å and 500 Å to form metal base electrodes and upper insulators through the same mask. After removing the polystyrene spheres with adhesive tape (Scotch, 3M), a grid electrode with pore diameter of 200 nm was formed. **Figure 4.4** shows the scanning electron microscopy (SEM) image when the PS is removed by the tape.

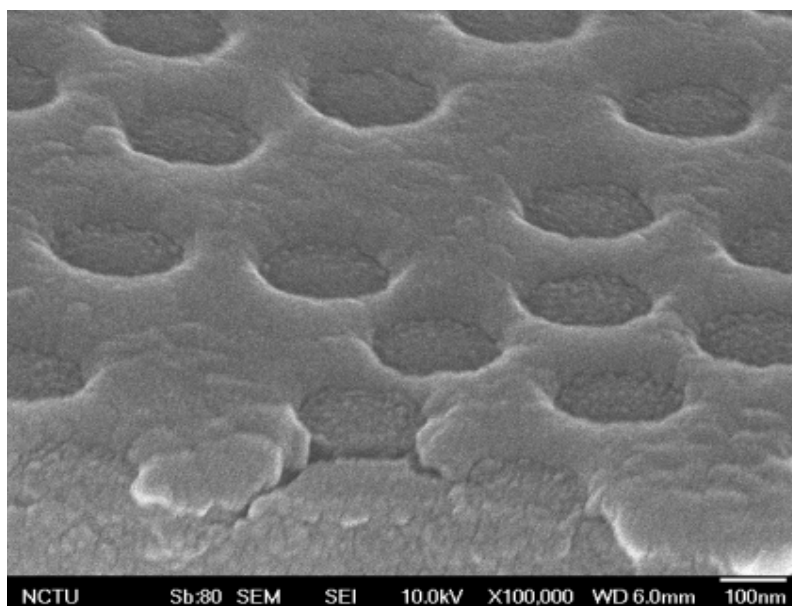


Figure 4.4 The scanning electron microscopy (SEM) image when the PS is removed by the tape.

The PVP at sites without Al coverage were removed through plasma treatment of 150 W O₂ for 13 min to open the channel region and the SEM image is shown in **Figure 4.5**.

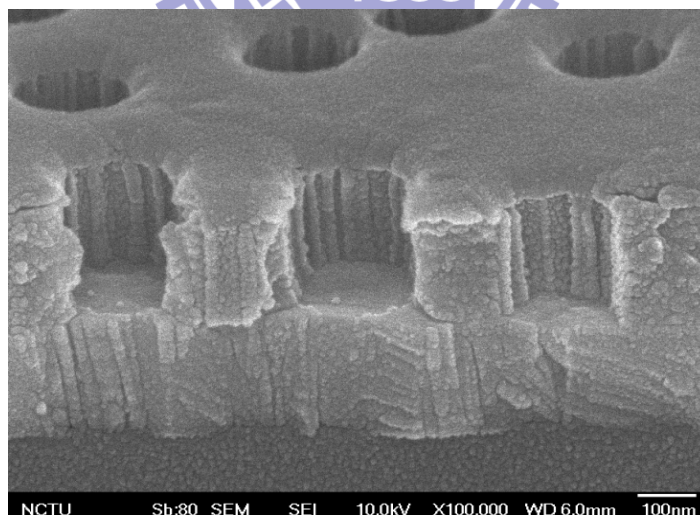


Figure 4.5 The PVP at sites without Al coverage were removed through plasma treatment of 150 W O₂ for 13 min to open the channel region.

The substrate was then stored in glove box and active layers were rapidly spin-coated onto the surface. Two kinds of active layer were used. One was P3HT of 3500 Å from

4.5 wt % chlorobenzene to form a conventional P3HT SCLT. The other was a blended P3HT:PCBM of 3500 Å from 4.5 wt % chlorobenzene to form a new P3HT:PCBM SCLT. The P3HT: PCBM blending ratio was 1:0.1 by weight. The schematic structure of P3HT and PCBM is shown in **Figure 4.6**.

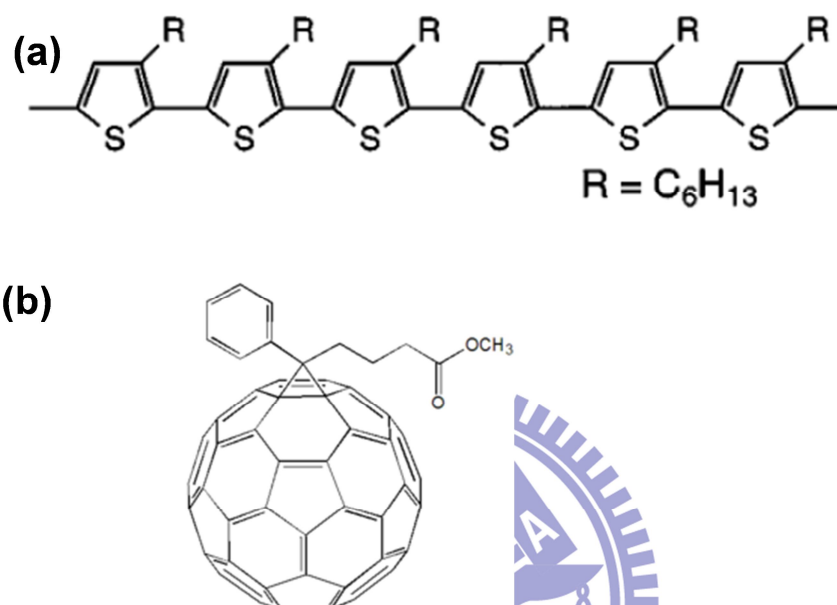


Figure 4.6 The chemical structure of (a) Polythiophene (P3HT) and (b) Phenyl-C₆₁-butyric acid methyl ester (PCBM).

Finally, Al was deposited to a depth of 40-nm for use as a collector electrode to complete a device with an active area of 1 mm². A light emitting diode backlight (LED) was used as the light source to irradiate the sample from the ITO electrode. The process flow is also shown in **Figure 4.7**.

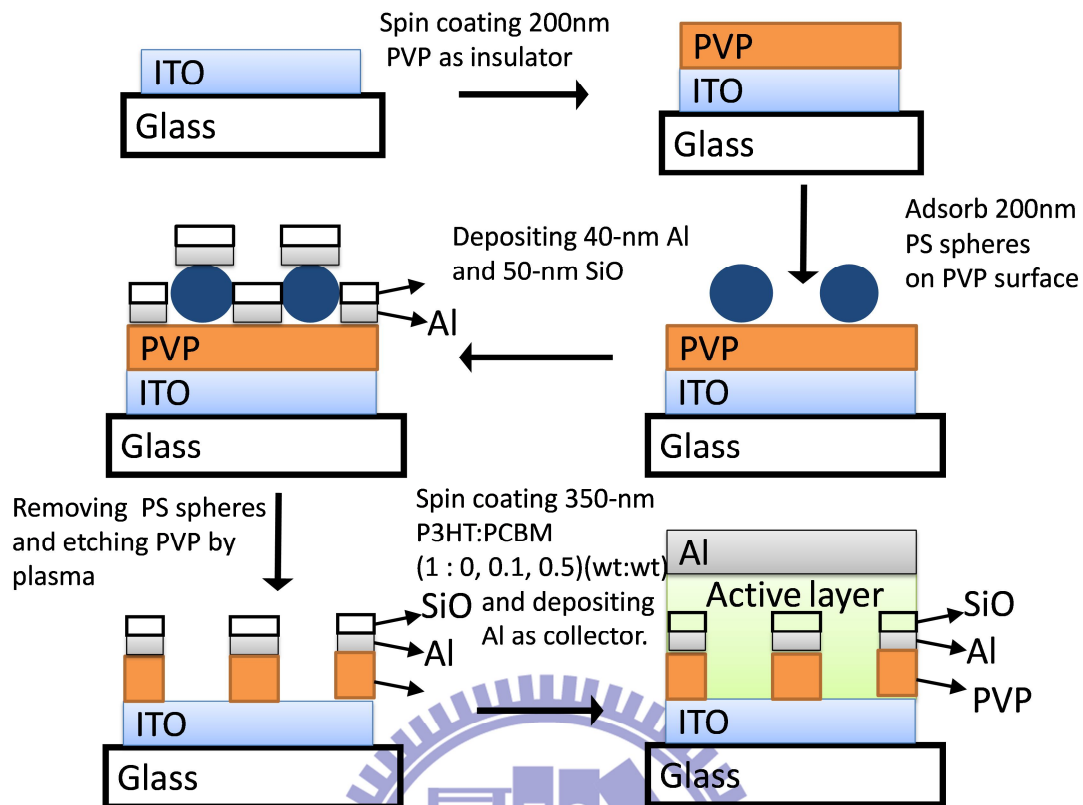


Figure 4.7 The processes flow of device fabrication.

4.2.2. Illumination System

The white light source comes from light-emitting diode (LED) backlight with a broad wavelength range. The light source was set up below the device to irradiate the sample from bottom. The light power was controlled by the power supply (PPT3615). The light intensity was adjusted by changing the applied voltage. The light intensity range is from 0.607 mW/cm^2 to 11 mW/cm^2 . **Figure 4.8** shows the illumination system.

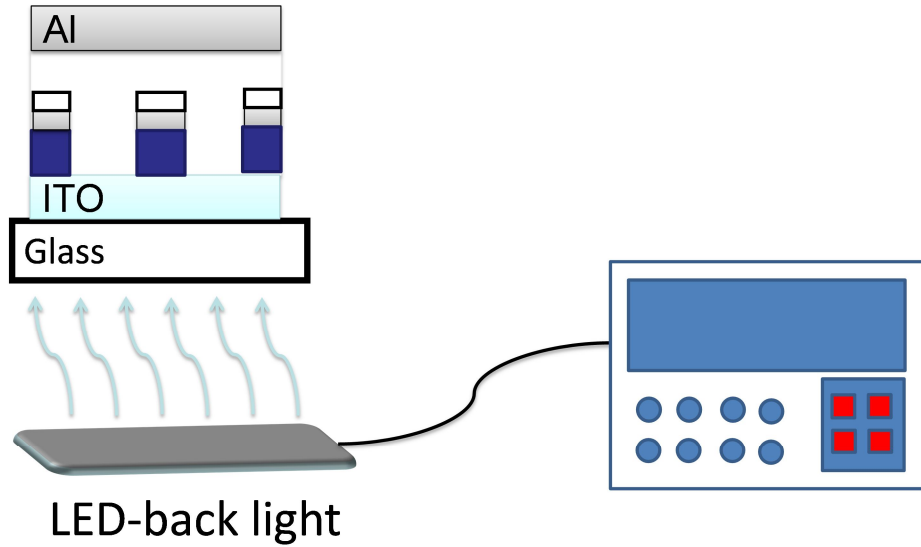


Figure 4.8 The illumination system and the vertical transistor. The organic active layer is P3HT or P3HT:PCBM. The thickness of the active layer is 350-nm.

4.3. Results and Discussions

SCLT is a solid-state triode using a metal grid as the base electrode to control the on/off state of the vertical channel between the emitter and collector electrodes.[7,12] In this study, P3HT SCLT exhibited characteristics similar to those reported in our previous study.[7] High on/off current ratio (> 10000) was obtained at a low collector-to-emitter operational voltage (V_{CE}) (~ -2.2 V). Also, the device output characteristic is shown in **Figure 4.9**.

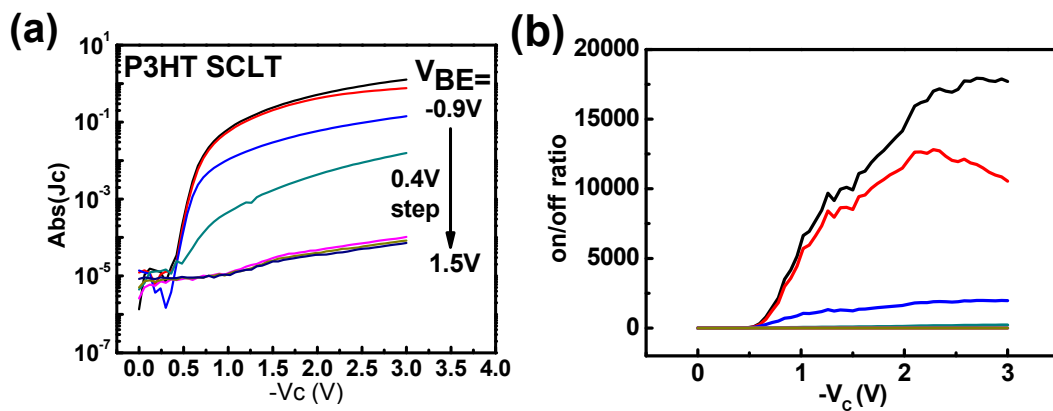


Figure 4.9 (a) Output characteristics of P3HT SCLT. The V_{CE} is sweep from 0 to -3V and the V_{BE} is step from -0.9 to 1.5 V. (b) The on/off current ratio of the P3HT SCLT.

In this study, the operational voltage (~ -2.2 V) was slightly higher than that in the previous report (~ -0.8 V) because the thickness of the PVP and P3HT was approximately 3 times greater than that of the previous report, thereby enabling greater control of the device current leakage. The transfer characteristics [i.e. collector current density (J_C) plotted as a function of the base-to-emitter voltage (V_{BE})] of P3HT SCLT in the total darkness, and under illumination when $V_{CE} = -1.5$ V are shown in

Figure 4.10.

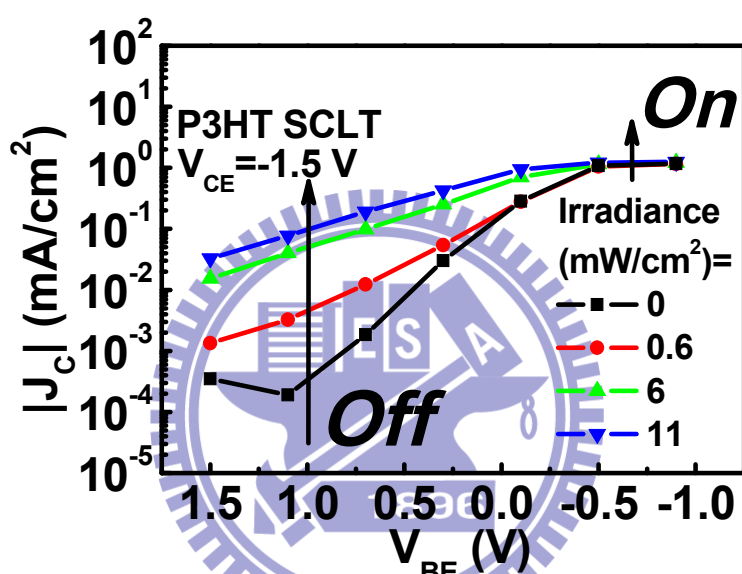


Figure 4.10 Transfer characteristics of a P3HT-SCLT in total darkness and under illumination. The light intensity is from 0 to 11 mW/cm².

In the total darkness, the *off* current was below 5×10^{-4} mA/cm². Under illumination, the *off* current increased significantly. If photo current density (J_{ph}) is defined as the current density under illumination minus the current density in total darkness (J_{dark}), J_{ph} as 1 mA/cm² is obtained when illumination intensity is 11 mW/cm², $V_{BE} = 1.5$ V, and $V_{CE} = -1.5$ V. We can assume that the high J_{ph} in P3HT SCLT was not produced by the photo-generated carriers in P3HT, due to the fact that exciton dissociation in P3HT without an acceptor blending is known to be poor. Poor exciton dissociation

was confirmed by measuring the J_C - V_{CE} curve in a reverse-biased EC diode with floating base potential in total darkness and under illumination (not shown). Low J_{ph} of 3×10^{-4} mA/cm² was obtained with illumination intensity of 11 mW/cm² and $V_{CE} = 1.5$ V.

To investigate the mechanism causing high J_{ph} in P3HT SCLT, we simulated carrier distribution and the potential channel profile with TCAD Silvaco Atlas software.

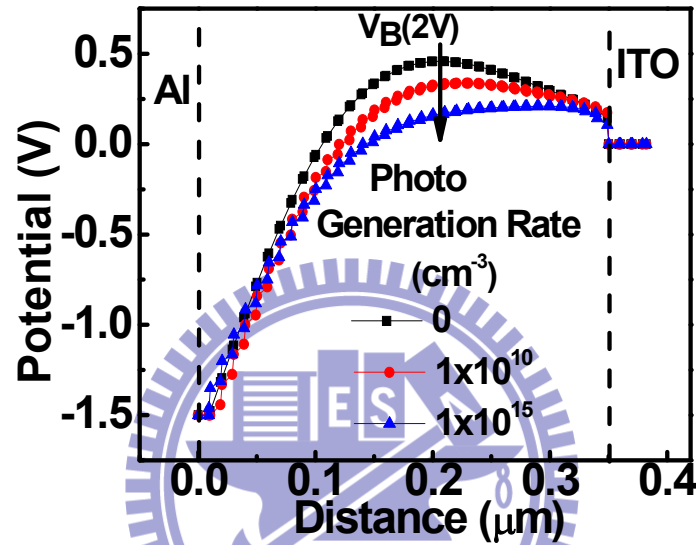


Figure 4.11 A simulated potential distribution at the central vertical channel.

The 2-dimensional simulation was performed by setting $V_{CE} = -1.5$ V and $V_{BE} = 2$ V to simulate the device operated in its *off* state. Material parameters were defined as in reference 13. The potential distribution in the central channel from emitter to collector is shown in **Figure 4.11**. In total darkness (i.e. photo generation rate = 0 cm⁻³), the emitter was unable to inject holes into the channel because the 2-V V_{BE} created a potential barrier to impede hole transport, whereby a low *off*-state current was achieved. Under illumination (i.e. photo generation rate = 10^{10} or 10^{15} cm⁻³), the potential barrier formed by the 2-V V_{BE} significantly dropped, and with a lower potential barrier, high *off*-state current was expected. A lower potential barrier under

illumination was explained by the 2-dimensional electron distribution plot shown in **Figure 4.12**.

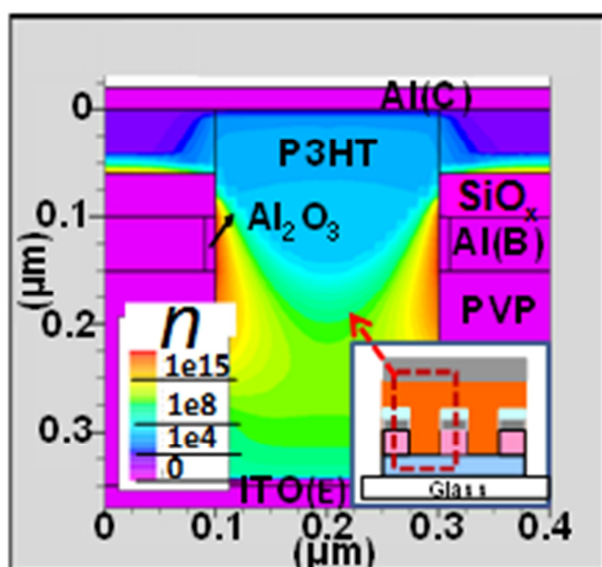


Figure 4.12 The 2-dimensional electron distribution of P3HT-SCLT with a photo generation rate = 10^{10} cm^{-3} and a $V_{BE} = 2 \text{ V}$. Electron concentration is denoted by n .

With a photo generation rate = 10^{15} cm^{-3} and a $V_{BE} = 2 \text{ V}$, the electrons generated by exciton dissociation accumulate around the base of the electrode. The accumulated electrons shield the base field and suppressed the influence of base bias on channel potential. As a result, the potential barrier caused by base bias was lowered under illumination. The *off*-state current, with exponential dependence on the potential barrier height, increased significantly. However, due to poor exciton dissociation in P3HT, the concentration of electrons around the base electrode was not high enough to completely shield the base-field. Therefore, in **Figure 4.10**, we see the *off*-state current density under irradiance as 11 mW/cm^2 is still 38 times lower than the *on*-state current density. If complete base-field shielding is expected for further enhancement of the photo response, the exciton dissociation in the channel region will need to be improved. In the following experiment, we added PCBM to P3HT to form a

donor/acceptor interface to improve exciton dissociation.

The characteristics of the P3HT:PCBM SCLT are shown in **Figure 4.13**. When base to emitter potential (V_{BE}) changed from -0.9 V to 1.5 V, the device was switched from *on* state to *off* state. Maximum on/off current ratio of approximately 5000 was obtained at a collector to emitter potential (V_{CE}) of -1.5 V. The on/off current ratio is inferior to that of P3HT SCLT because electron injection from the collector metal (aluminum) to PCBM caused a leakage in the current. An electron blocking layer between the collector and active layer could be applied to reduce the leakage in future studies.

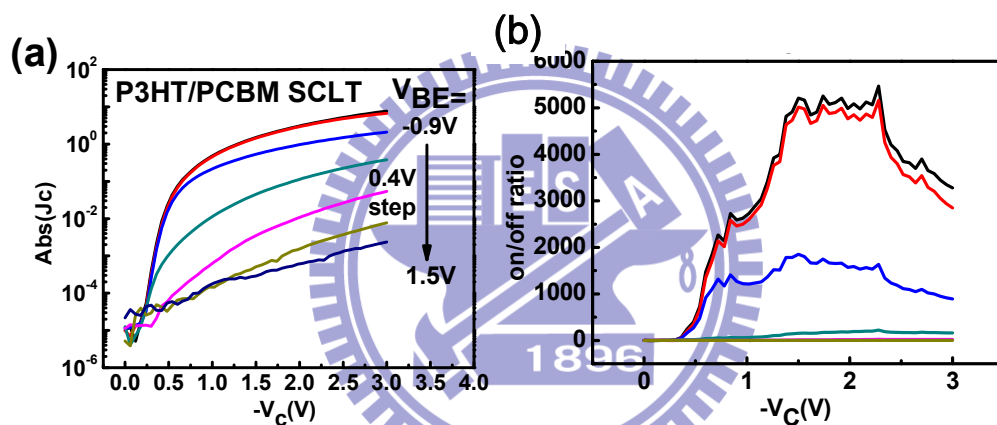


Figure 4.13 (a) Output characteristics of P3HT:PCBM (1 : 0.1) (wt : wt) SCLT. The V_{CE} is sweep from 0 to - 3V and the V_{BE} is step from - 0.9 to 1.5 V. (b) The on/off current ratio of the P3HT:PCBM (1 : 0.1) (wt : wt) SCLT.

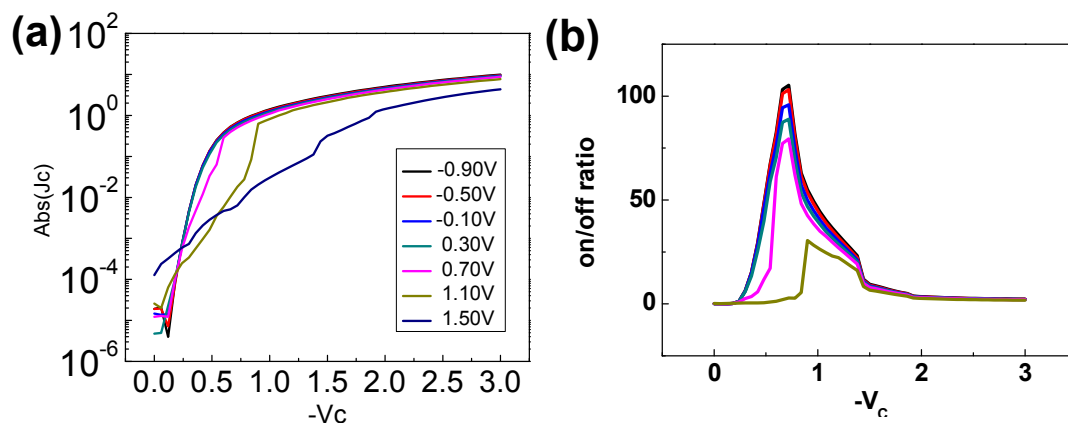


Figure 4.14 (a) Output characteristics of P3HT:PCBM (1 : 0.5) (wt : wt) SCLT. The V_{CE} is sweep from 0 to - 3V and the V_{BE} is step from - 0.9 to 1.5 V. (b) The on/off

current ratio of the P3HT:PCBM (1 : 0.5) (wt : wt) SCLT.

In this work, to maintain a reasonable on/off current ratio, the P3HT:PCBM blending ratio was kept to 1:0.1 by weight. If the P3HT:PCBM blending ratio were 1:0.5 or 1:1, the device would suffer from large leakage current, which would degrade switching performance. The output characteristics of 1:0.5 and 1:1 P3HT:PCBM is shown in **Figure 4.14**, respectively. The transfer characteristics of a P3HT:PCBM SCLT in total darkness and under illumination are shown in **Figure 4.15**. V_{CE} is fixed as -1.5 V. J_C in total darkness, represented by dark square symbols in **Figure 4.15**.

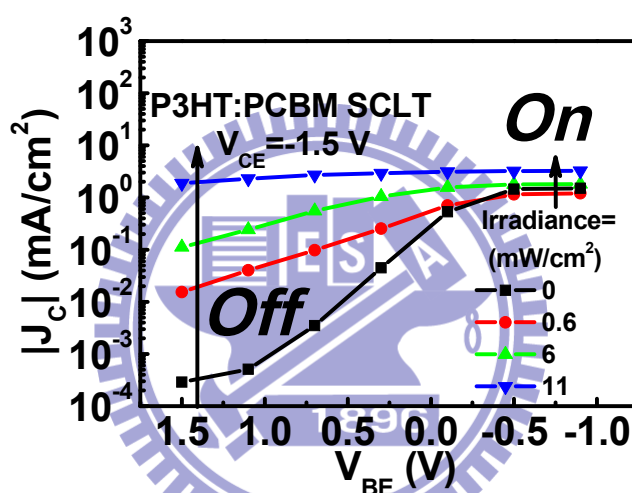


Figure 4.15 Transfer characteristics of a P3HT:PCBM SCLT in total darkness and under illumination. The light intensity is from 0 to 11 mW/cm².

This exhibits significant *on*-state and *off*-state when V_{BE} changes from negative to positive. Under illumination, both *on*-state J_C and *off*-state J_C increased with an increase in the intensity of illumination. On/off current ratio decreased with increases in the intensity of illumination, indicating a weaker base control over the channel. When light intensity was 11 mW/cm², the *off*-state J_C was nearly equal to the *on*-state J_C . The base field was completely shielded and V_{BE} lost control over J_C . To compare the effect of base-field shielding in P3HT:PCBM SCLT and in P3HT SCLT, transfer characteristics of P3HT under illumination (11 mW/cm²) are represented by a grey

line in **Figure 4.13**. *Off*-state J_C at $V_{BE} = 1.5$ V is one order lower than *on*-state J_C at $V_{BE} = -0.9$ V. P3HT SCLT, and has inferior base-field shielding to P3HT:PCBM SCLT. Blending 0.1 wt% PCBM with P3HT enhanced the effect of base-field shielding in SCLT. For the P3HT:PCBM-SCLT, there is a reasonable injection of electrons by the cathode and a reasonable conduction for electrons. The electrons injected by the cathode must therefore accumulate around the base region. The P3HT:PCBM device, however, can be switched off in dark because the accumulated electrons are removed by the base current. When the P3HT:PCBM device is operated in dark, the base current is about 10^{-4} mA/cm² and is approximately equal to the off current in dark as shown in **Figure 4.15**. When the P3HT:PCBM device is under irradiance as 11 mW/cm², the base current is about 10^{-1} mA/cm² and is one order smaller than the off current under irradiance as 11 mW/cm² as shown in **Figure 4.15**. It is proposed that the base current is not able to fully remove the accumulated electrons around the base electrode. The accumulated electrons then shield the base field. **Figure 4.16 (a) and 16 (b)** show the off current density of P3HT:PCBM-SCLT as a function of collector to emitter voltage. In **Figure 4.16 (a)**, the device is operated under off-state in total darkness and the collector current density is nearly equal to the base current density plus the emitter current (i.e. $J_C = J_E + J_B$). There are few electrons to accumulate around the base region, and therefore, the device can be switched off. On the contrary from the **Figure 4.16(b)**, the device is operated in off-state under illumination, the collector current density is nearly equal to the emitter current density and is much higher than the base current density. Therefore, the device cannot be switched off under illumination because there are enough electrons to accumulate around the base region and screen the base field.

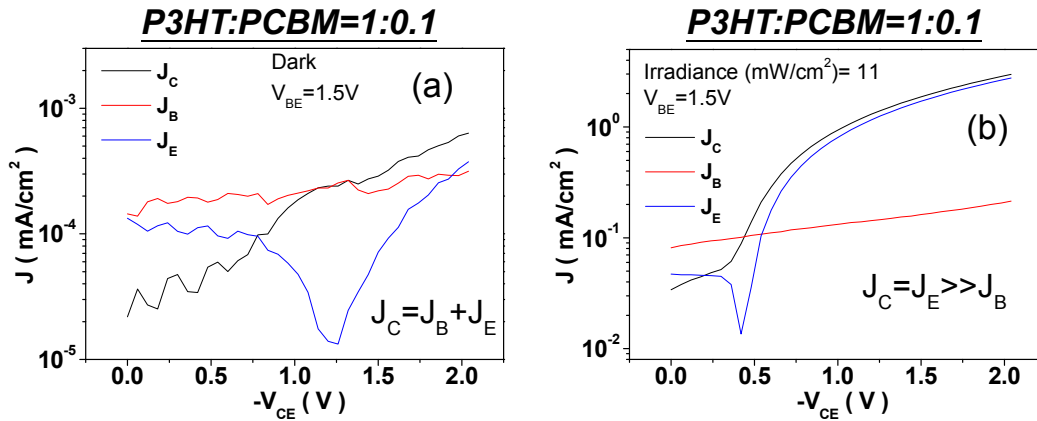


Figure 4.16 The off current density of P3HT:PCBM-SCLT as a function of collector to emitter voltage. (a) The device is operated under off-state in total darkness and the collector current density is nearly equal to the base current density plus the emitter current (i.e. $J_C = J_E + J_B$). (b) The device is operated in off-state under illumination, the collector current density is nearly equal to the emitter current density and is much higher than the base current density.

In **Figure 4.17**, it is interesting to note that the *on*-current also increases significantly under illumination. Because the SCLT operated in *on*-state is similar to a forward-biased diode, we needed to analyze the photo response of a P3HT:PCBM diode in both reverse and forward bias conditions. We fabricated two planar ITO/P3HT:PCBM/Al diodes. One with a P3HT:PCBM blending ratio of 1:0.1 (Diode-A), and the other with a P3HT:PCBM blending ratio of 1:1 (Diode-B). The J_{ph} (i.e. $J_{ill} - J_{dark}$) of these two diodes was plotted as a function of bias voltage in **Figure 4.17** wherein the intensity of illumination was 11 mW/cm². In reverse-biased conditions, Diode-A had a much lower J_{ph} than Diode-B, because the low PCBM percentage suppressed exciton dissociation. In forward-biased conditions, J_{ph} of Diode-A was 20 times higher than that of Diode-B. Obviously, exciton dissociation does not explain the large J_{ph} in forward-biased conditions. We propose that the hole

injection from ITO to P3HT is enhanced under illumination. In previous reports, photo-induced carrier injection was a result of carrier trapping at the injection interface to lower the injection barrier.[8] The J_{ph} of EC diode in P3HT:PCBM-SCLT is shown by a dotted line in **Figure 4.17**. We obtained a J_{ph} higher than 1 mA/cm^2 , when forward-biased voltage was 1.5 V (i.e. $V_{CE} = -1.5 \text{ V}$). Although the forward-biased Diode A and the forward-biased EC diode had high J_{ph} , their photo-to-dark current ratios [$J_{ph}/J_{dark}=(J_{ill}-J_{dark})/J_{dark}$] were smaller than 1, because of the high J_{dark} . In P3HT:PCBM-SCLT, the current flowing through a forward-biased EC diode (i.e. $V_{CE} = -1.5 \text{ V}$) was turned off by the base potential in total darkness, and as a result, a low J_{dark} was achieved. Under illumination, base electrodes lose control over channel current due to the effect of base-field shielding. At the same time, the effects of photo-enhanced hole injection in the forward-biased EC diode contribute to high channel current. The photo-to-dark current ratios (J_{ph}/J_{dark}) were 4×10^2 , 4×10^3 , and 6×10^3 , when illumination intensities were 0.6 , 6 , and 11 mW/cm^2 , respectively.

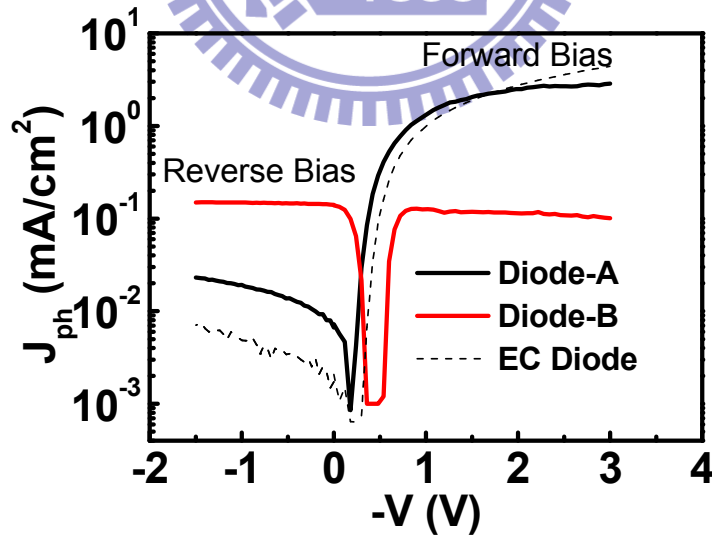


Figure 4.17 The J_{ph} of planar diode of P3HT:PCBM=1:0.1 (Diode-A), planar diode of P3HT:PCBM=1:1 (Diode-B), and EC diode in P3HT:PCBM-SCLT(P3HT:PCBM=1:0.1) plotted as a function of bias voltage. In reverse-biased conditions, Diode-A had a much lower J_{ph} than Diode-B, because the low PCBM percentage suppressed exciton dissociation. In forward-biased conditions,

J_{ph} of Diode-A was 20 times higher than that of Diode-B. Obviously, exciton dissociation does not explain the large J_{ph} in forward-biased conditions. We propose that the hole injection from ITO to P3HT is enhanced under illumination.

Also, we measured the external quantum efficiency (EQE) of the P3HT:PCBM-SCLT with an active area of 1 mm^2 , $V_{CE} = -1.5 \text{ V}$ and $V_{BE} = 1.5$ or 3 V , as shown in **Figure 4.18**. In SCLT, when irradiated from an ITO electrode, only a fraction of the active area comprised P3HT:PCBM material. The EQE measured in this case was actually an effective EQE per unit active area. The maximum EQE of P3HT:PCBM-SCLT was 110% and 360% at 620 nm when $V_{BE} = 1.5$ and 3 V , respectively. An EQE higher than 100, representing a photomultiplication (PM) phenomenon, was dominated by a base-field shielding effect. The high EQE, however, had a narrow bandwidth.

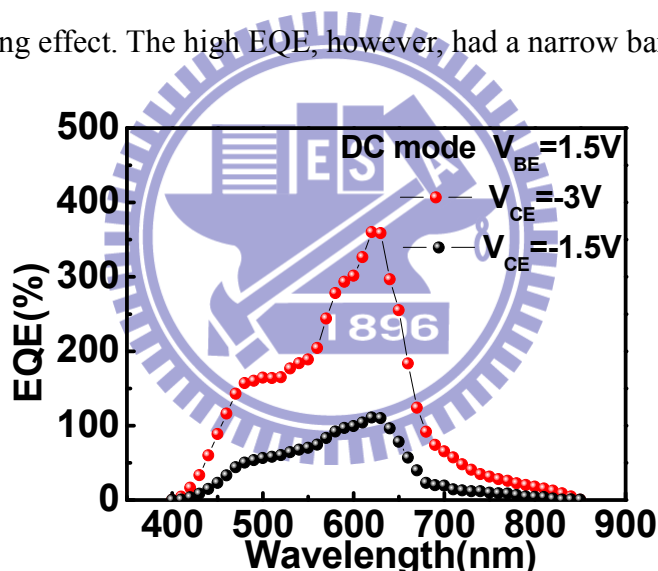


Figure 4.18 The EQE of P3HT:PCBM-SCLT. The V_{BE} is fixed at 1.5 V . The EQE measured in this case was actually an effective EQE per unit active area. The maximum EQE of P3HT:PCBM-SCLT was 110% and 360% at 620 nm when $V_{BE} = 1.5$ and 3 V , respectively.

When the measured EQE frequency increased to 80 and 160 Hz (shown as **Figure 4.19**), maximum EQE dropped to 15 and 12, respectively. The narrow bandwidth could be explained by slow electron accumulation surrounding the base electrode. Under illumination, excitons dissociated at P3HT:PCBM interface to generate free

electrons. Electrons moved from P3HT:PCBM interface to the base electrode to accumulate around the base. However, low electron mobility in P3HT blend with 0.1 wt% PCBM suppressed the rate of electron accumulation.

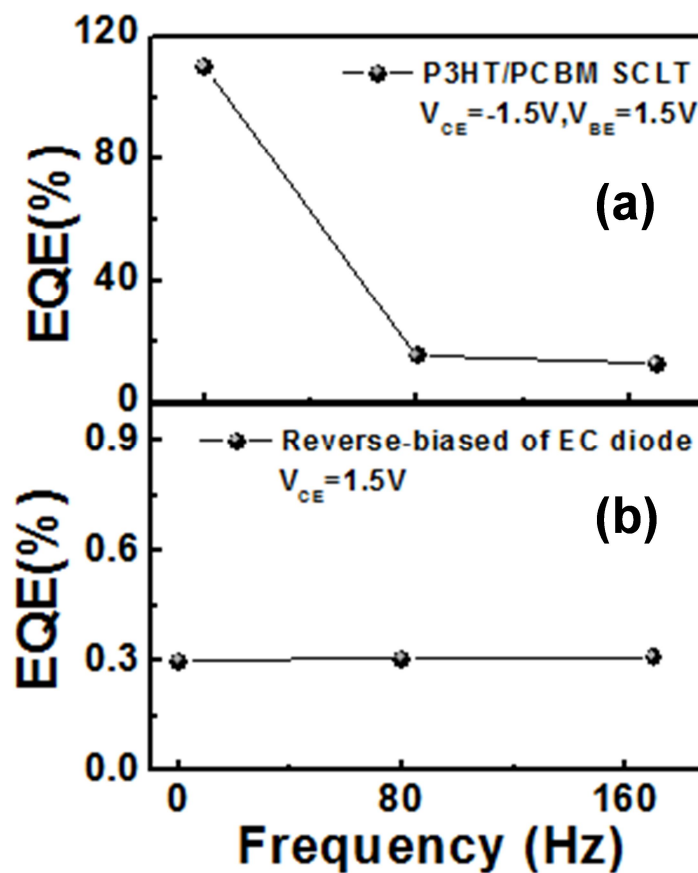


Figure 4.19 The (a) EQE of P3HT/PCBM SCLT and (b) EQE of device EC diode as a function of frequency response. . When the measured EQE frequency increased to 80 and 160 Hz, maximum EQE dropped to 15 and 12, respectively. The narrow bandwidth could be explained by slow electron accumulation surrounding the base electrode. However, the EC diode is not dependent on the frequency.

The response of the base-field shielding effect was therefore slow. In future studies, incorporating more PCBM into P3HT may succeed in enhancing the speed of the base-field shielding, while an electron blocking layer between the collector (aluminum) and active layer would be required to prevent leakage through PCBM. Finally, a 633nm laser diode source pulsing at a frequency of 1 Hz. Collector current density (J_C) of the P3HT:PCBM SCLT with blending ratio of 1: 0.1 (wt:wt) in the

turn-off condition was tracked as shown in **Figure 4.20**. For a P3HT:PCBM SCLT biased with $V_C = -3V$ and $V_B=1.5V$, rapid and significant current response was obtained.

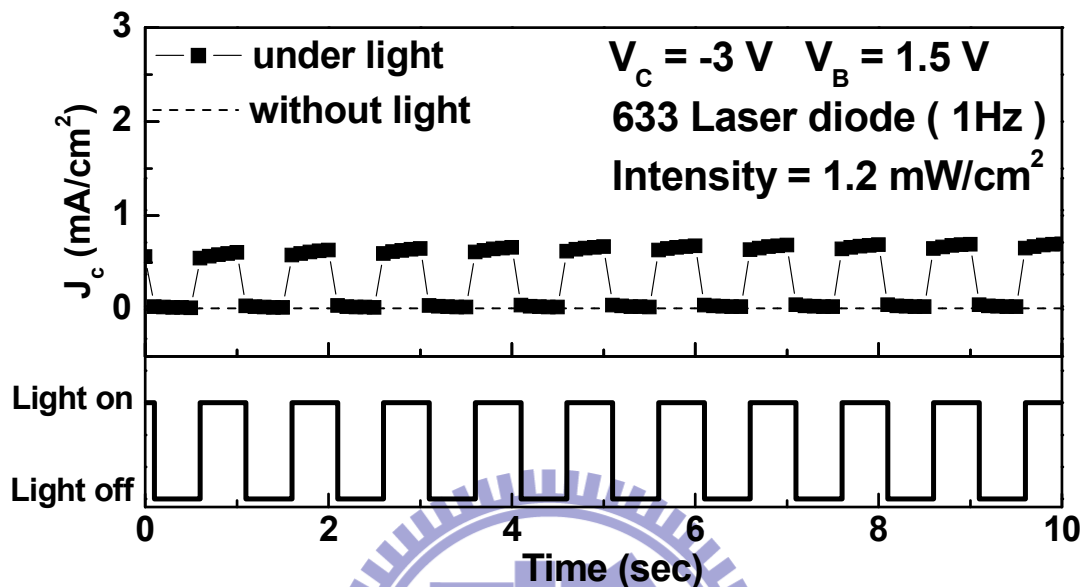


Figure 4.20 Off current density of P3HT:PCBM SCLT monitored under pulsed illumination of 1 Hz frequency. The light source is laser diode with 633 nm wavelength. The device was biased at $V_C = -3 V$ and $V_B=1.5 V$.

4.4. Conclusion

In summary, we demonstrated a vertical polymer phototransistor, based on the space-charge limited transistor (SCLT). The photo response in SCLT was governed by the following steps. First, the SCLT was operated in the *off*-state to provide a current in total darkness. The EC diode was forward biased and the base potential created a potential barrier to impede hole transport. Second, under illumination, excitons were generated in the polymer channel layer. In this study, the channel material was P3HT blended with PCBM at a blending ratio of 1:0.1, to enhance exciton dissociation. Third, after exciton dissociation, electrons flowed toward the base electrode. Electrons accumulated around the base electrode shield of the base field. As a result, the potential barrier was reduced. At the same time, the hole injection from ITO into

the channel is enhanced. Finally, with the reduction in the potential barrier and the enhancement of hole injection, a large photocurrent was obtained.

References:

- [1] R. D. Yang, T. Gredig, C. N. Colesniuc, J. Park, I. K. Schuller, W. C. Trogler, and A. C. Kummel, "Ultrathin organic transistors for chemical sensing" *Appl. Phys. Lett.* 90, 263506, (2007).
- [2] I. Manunza and A. Bonfiglio, "Pressure sensing using a completely flexible organic transistor" *Biosens. and Bioelectron.*, 22, 12, (2007).
- [3] Y. Y. Noh, D. Y. Kim, and K. Yase, "High-photosensitivity p-channel organic phototransistors based on a biphenyl end-capped fused bithiophene oligomer" *J. Appl. Phys.* 98, 074505, (2005).
- [4] P. Peumans, V. Bulovic, and S. R. Forrest, "Efficient, high-bandwidth organic multilayer photodetectors" *Appl. Phys. Lett.* 76, 3855, (2000).
- [5] W. W. Tsai, Y. C. Chao, E. C. Chen, H. W. Zan, H. F. Meng, and C. S. Hsu, "Increasing organic vertical carrier mobility for the application of high speed bilayered organic photodetector" *Appl. Phys. Lett.* 95, 213308, (2009).
- [6] M. Debucquoy, S. Verlaak, S. Steudel, K. Myny, J. Genoe, and P. Heremans, "Correlation between bias stress instability and phototransistor operation of pentacene thin-film transistors" *Appl. Phys. Lett.* 91, 103508, (2007).
- [7] Y. C. Chao, Y. C. Lin, M. Z. Dai, H. W. Zan, and H. F. Meng, "Reduced hole injection barrier for achieving ultralow voltage polymer space-charge-limited transistor with a high on/off current ratio" *Appl. Phys. Lett.* 95, 203305, (2009).
- [8] J. Reynaert, V. I. Arkhipov, P. Heremans, and J. Poortmans, "Photomultiplication in disordered unipolar organic materials" *Adv. Funct. Mater.* 16, 784, (2006).
- [9] M. Hiramoto, T. Imahigashi, and M. Yokoyama, "Photocurrent multiplication in

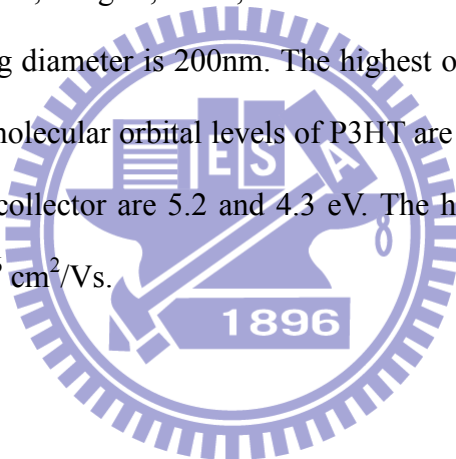
organic pigment films” *Appl. Phys. Lett.* 64, 187, (1994).

[10] J. Hunang and Y. Yang, “Origin of photomultiplication in C60 based devices” *Appl. Phys. Lett.* 91, 203505, (2007).

[11] Y. C. Chao, H. F. Meng, S. F. Horng, and C. S. Hsu, “High-performance solution-processed polymer space-charge-limited transistor” *Org. Elec.* 9, 310-316, (2008).

[12] Y. C. Chao, C. Y. Chen, H. W. Zan, and H. F. Meng, “The influences of device geometry and p-type doping on a solution-processed polymer space-charge-limited transistor” *J. Phys. D: Appl. Phys.* 43, 205101, (2010).

[13] The thickness of PVP, Al grid, SiO_x, and P3HT are 200, 40, 50 and 350 nm, respectively. The opening diameter is 200nm. The highest occupied molecular orbital and lowest unoccupied molecular orbital levels of P3HT are 5.2 and 3.0 eV. The work function of emitter and collector are 5.2 and 4.3 eV. The hole mobility and electron mobility are 10⁻⁵ and 10⁻⁶ cm²/Vs.



Chapter 5. Pentacene-based Organic Thin Film

Transistors for Ammonia Sensing

5.1. Introduction

Analyzing the chemical composition of human breath helps people to examine their health conditions. It is a convenient method for a non-invasive diagnosis of disease and has been used for centuries[1]. More than 200 organic or inorganic gaseous molecules[2] were examined in human breath. These gaseous species were produced through normal physiological processes or pathological conditions such as gastric ulcer, liver disease, cancer, or renal failure. A gas sensor that can monitor the unusual concentrations of these specific molecules in human breath can be very useful for the non-invasive diagnosis of these diseases.

Diagnosis of disease using human breath has been successfully demonstrated for *H. pylori* infection[3]. The target analyte is C13 labeled carbon dioxide ($^{13}\text{CO}_2$), which is produced when patient ingest C13 labeled urea. Another example is the diagnosis of diabetes using gas-sensitive LAPS (Light Addressable Potentiometric Sensors) for breath test[4]. However, both cases are limited in hospitals or medical centers for the readout of the sensing signals required expensive instruments. Facing with the ageing society and urgent need for personalized medicine, it is essential to develop cheap and portable gas sensors for patients and to trace their conditions at home.

Ammonia is an crucial indicator for uremia and chronic liver disease (**Table 2.1**). Breath ammonia level is significantly higher in cirrhotic patients (0.745 ppm) than that in normal person (0.278 pm)[5]. Patients who have renal failure even exhale 4.8 ppm ammonia in their breath[6]. Although these medical indicators suggest a convenient method for the diagnosis of these crucial diseases, suitable ammonia

sensor was not available. Current ammonia sensors such as polyaniline sensors, metal oxide sensors, catalytic sensors, and optical analyzers suffer from disadvantages such as high operation temperature, low sensitivity and high cost[7, 8]. Adequate ammonia sensor for biomedical application should be able to detect ammonia from around 0.5 ppm to 5 ppm at room temperature as described above for cirrhotic[5] and renal failure patients[6]. No ammonia sensor that fulfill the requirements has been reported.

Organic thin-film transistors (OTFTs) were reported to be a non-invasive, inexpensive, portable and disposable diagnostic device because of its low cost fabrication process and high sensitivity to gas molecules[9]. The molecular active channel in OTFTs enables the devices to exhibit rapid response in both gaseous[10] and aqueous[11] sensing environment. It is proposed that the gas molecules penetrate organic active layer through grain boundaries and diffuse into channel region to react with carriers[12, 13]. As a result, the sensitivity is high and is strongly dependent on the morphology and the grain boundary density of the organic film[14]. Compared with resistor-type sensors, OTFTs provide multiple sensing parameters such as field-effect mobility, turn-on conductivity, turn-off conductivity, threshold voltage and subthreshold swing[15]. Also, OTFTs with different active layer materials can form an OTFT array to provide sensing selectivity through a sensing map[9]. Some approaches have been demonstrated to increase the sensitivity and selectivity of OTFT gas sensor by changing the functional group, the grain structure of organic layer[16], or varying the device dimension[17]. However, they didn't study OTFT response to ammonia gas. Only one paper demonstrates OTFT response to ammonia gas[18]. However, the detection limitation was not defined. The feasibility of using OTFTs as non-invasive diagnostic sensor was not discussed.

In our study, for the first time, we demonstrate OTFT to be an ammonia sensor with the detection range of 0.5 ppm ~ 5 ppm. They are applicable on the breath test of

cirrhotic and renal failure patients. To increase the device sensitivity to ammonia molecules, we also propose a simple UV irradiation process to increase the dipole moment on gate dielectric surface. We successfully demonstrated that the increased dipole moment on dielectric surface effectively enlarge the OTFT response to ammonia molecules. OTFT sensitivity to low-concentration (0.5 ppm) ammonia gas is also significantly improved.

5.2. Experiment

5.2.1. Device Fabrication Process

The highly-doped p-type silicon wafers with 100 nm thick silicon oxide were used as the substrate. The p-type silicon was used as gate electrode, and the silicon oxide layer was used as gate insulator. After cleaned with 5 min de-ionized water, 5min acetone, and 5min de-ionized water, the particles and the impurities on the substrate were removed in order to avoid gate leakage which may cause instability [19]. Then, soluble poly (methyl methacrylate) (PMMA) was spun on the silicon oxide layer by the spin coater to improve the electric performance and increase the grain boundaries [20]. The PMMA was obtained from MicroChem. Corp. with a molecular weight of 95000 and was dissolved in anisole at 10 wt %. The spin speed was accelerated from 0 to 1000 rpm during the first 10 seconds and further increased to 7500 rpm during the following 10 seconds. After kept as 7500 rpm for 40 seconds, the spin speed was decreased from 7500 to 1000 in the following 10 seconds and further decreased to 0 rpm during 10 seconds. After the process of spin coating, the PMMA layer was annealed by hot plate with 90°C for 30 minutes. The capacity of PMMA/SiO₂ dielectric layer was about 23~24 nF/cm². Besides, some of the samples were then exposed to UV-light, whose wavelength is 175~285 nm and the output power is 40

mW, for 60 seconds to modify the functional group of PMMA. Then, the pentacene material obtained from Aldrich with 99.9% purity was evaporated through a shadow mask on the UV treated and un-UV treated PMMA/SiO₂ dielectric layer as the active layer. The deposition was started at the pressure around 3×10^{-6} torr and the temperature was kept at 25°C. The deposition rate of 1000-Å-thick pentacene was 0.1 Å/sec at the first 100Å and was smoothly increased to 0.5 Å/sec at the 200Å to the 1000Å. The deposition temperature, the deposition pressure and the deposition rate are the crucial parameters to decide the ordering quality of the organic film [21]. Finally, we used gold as the source and drain electrodes. Due to its similar work function with the HOMO level of pentacene, we can get better injection from gold to pentacene film. Before gold deposition, we deposited 50-Å-thick nickel through a shadow mask on the pentacene film as the adhesion layer. Then, we deposited 1000-Å-thick gold on the samples. The width (W) and length (L) of the device's channel were 800 μm and 1200 μm, respectively. Schematic cross-sectional view of STD- and UV-Treated OTFTs (UV-OTFTs) are shown in **Figure 5.1 (a) and (b)**, respectively. **Figure 5.2(a)** is the flowchart for the fabrication processes.



Figure 5.1 Device structure of (a) STD-OTFT and (b) UV-OTFT.

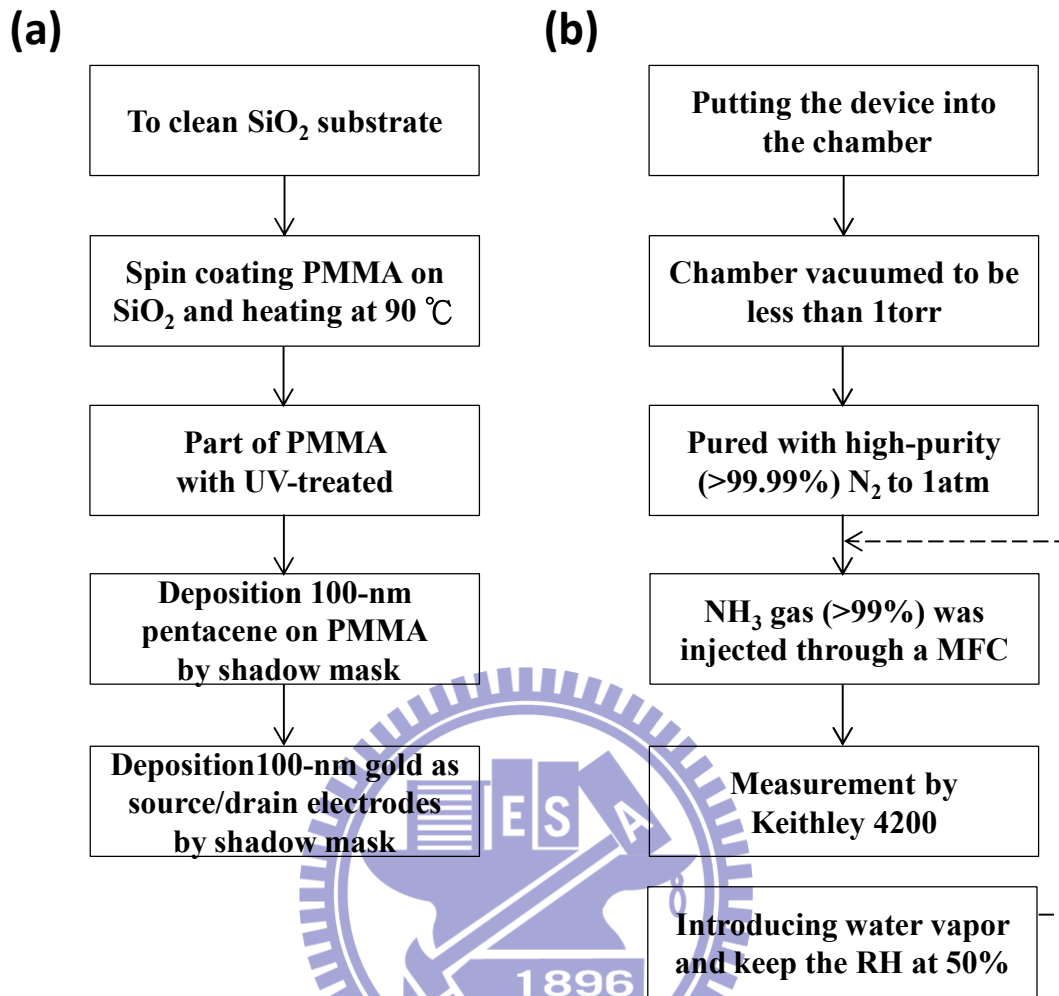


Figure 5.2(a) The flowchart for the fabrication processes and (b) for the measurement characterization.

5.2.2. Gas Sensing System

In this study, we used OTFTs devices to sense five different kinds of gas as following: ammonia (NH_3), methane (CH_4), acetone (CH_3COCH_3), alcohol ($\text{C}_2\text{H}_5\text{OH}$) and carbon dioxide (CO_2). To control the environment in the precise condition, we measured the devices with a semiconductor analyzer (Keithley 4200-SCS) in a sealed chamber. The inside volume of the chamber is about 42 L and its configuration image is shown in **Figure 5.3**. After putting the device into the chamber, we vacuumed it to the pressure of 10^{-6} torr and then purged it with high purity nitrogen (99.99% N_2) to the pressure of 1 atm. This process can avoid the influence of moisture and other

gases we did not want to sense. Thus, the data measured in the N_2 ambiance was the standard data. Then, we injected the gas we wanted into the chamber and measured the device's characteristic.

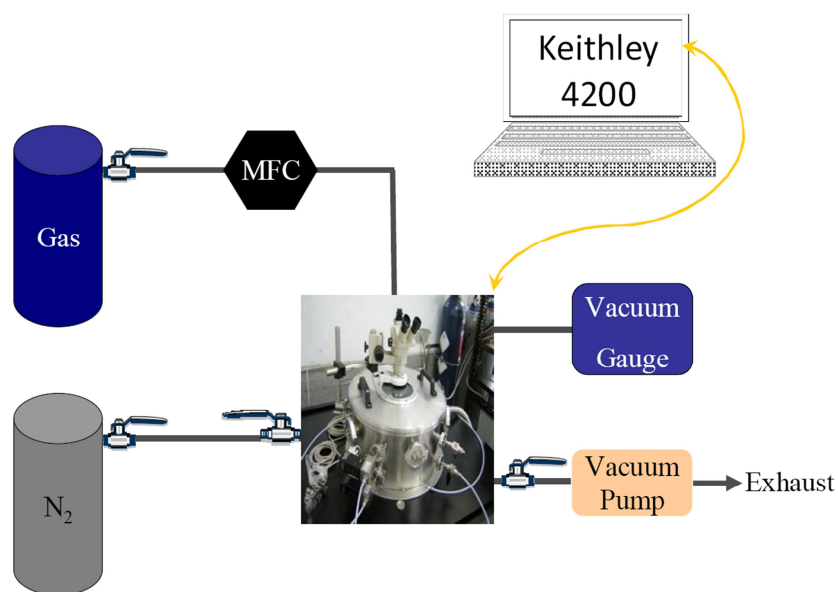


Figure 5.3 The gas sensing system. The chamber holder is surrounded by the 5 probing-stages and the injected gas is controlled by mass flow controller (MFC). Before starting the gas sensing experiment, we used the mechanical pump to pump down the chamber at a pressure less than 1 torr. Then we used the high-purity nitrogen gas (99.99%) to purge the chamber to a pressure about 1 atm and kept the chamber in the low moisture and oxygen. Then, we introduced ammonia gas through the mass flow controller.

The concentration of NH_3 was controlled as 0.5, 1, 3 and 5 ppm (mg/L) by a mass flow controller (MFC). CH_4 and CO_2 gases were also injected through a MFC and their concentrations were controlled as 2 ppm. To get CH_3COCH_3 and C_2H_5OH gases, we used a tedlar bag and put liquid CH_3COCH_3 and C_2H_5OH inside. After liquid CH_3COCH_3 and C_2H_5OH evaporated to saturate pressure, we injected the gases into the chamber with a syringe which can control the concentration as more than 2ppm.

To discuss the influence of moisture during the gas sensing process, we also provided

different relative humidity (RH) environment. By using a N₂ flow to pump water, water vapor can be introduced into the chamber. We controlled the RH value as 0% and 50% with different input time and measured the RH with a hygrometer. The flowchart for measurement characterization is shown in **Figure 5.2(b)**.

5.3. Parameter Extraction

It is crucial to analyze the data with a reasonable method. In this section, I introduce the method we used to extract the three crucial parameters of the devices from the electrical characteristics, such as field effect mobility, threshold voltage, and subthreshold swing.

5.3.1. Field Effect Mobility

Mobility (μ) is an crucial parameter in most electronic devices because it is directly related to the performance of a transistor. It is normalized for channel width, channel length, and dielectric capacitance.

Generally, mobility can be extracted from the transconductance maximum g_m in the linear region:

$$g_m = \left[\frac{\partial I_D}{\partial V_G} \right]_{V_D = \text{constant}} = \frac{WC_{ox}}{L} \mu V_D \quad (5.1)$$

$$\mu = \frac{g_m}{\left(\frac{W}{L} C_{ox} V_D \right)} \quad (5.2)$$

, where W is the width, L is the length of the channel, and C_{ox} is the capacitance of the dielectric layer.

5.3.2. Threshold Voltage

In inorganic electric devices, threshold voltage (V_{th}) is defined as the point at which the channel has been completely inverted. That means when the concentration of inversion charge in the channel equals the equilibrium majority charge carrier concentration in the bulk. But the most commonly used definition for threshold voltage (V_{th}) of an OTFT is extracted from equation (5.3), by extrapolating the linear I_D - V_G plot at $I_D=0$.

$$I_D = \frac{W \mu C_{ox}}{L} [(V_G - V_T)V_D - \frac{V_D^2}{2}] \quad (5.3)$$

In organic semiconductor, the V_{th} is determined primarily by the relative work-function of the gate, source/drain contacts and the organic layer, as well as the fixed charge and trap distributions in the organic layer. Because of run-to-run variations, the parameters can be difficult to suppress. Thus, V_{th} control is an crucial hurdle to commercialization of OTFTs.

5.3.3. Subthreshold Swing

Subthreshold swing is also crucial characteristics for device application. It is a measure of how rapidly the device switches from the off state to the on state in the region of exponential current increase. Moreover, the subthreshold swing also represents the interface quality and the defect density. High performance TFTs mean lower subthreshold swing of transistors.

$$S = \left. \frac{\partial V_G}{\partial (\log I_D)} \right|_{V_D = \text{constant}}, \text{ when } V_G < V_T \text{ for p-type.} \quad (5.4)$$

5.4. Comparisons of Ammonia-Sensing Phenomenon in STD-OTFTs and UV-OTFTs

5.4.1. Electrical Properties of STD-OTFTs and UV-OTFTs

The transfer characteristics of STD-OTFTs and UV-OTFTs are compared in **Figure 5.4**.

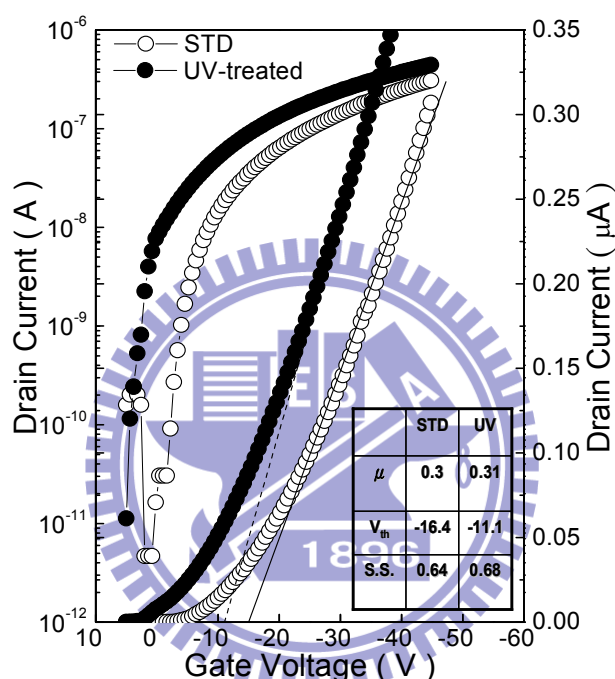


Figure 5.4 The transfer characteristics of STD and UV-OTFTs. Drain current (I_d) was measured at a constant drain voltage ($V_d = -3$ V) while gate bias (V_g) sweeps from 5 to -45 volts. Field effect mobility and threshold voltage were calculated in the linear regime ($V_d = -3$ V) defined by standard metal-oxide-semiconductor FET model. S.S was also extracted from the transfer characteristics. The extracted typical electrical parameters [mobility ($\mu(\text{cm}^2/\text{Vs})$), threshold voltage ($V_{th}(\text{V})$), subthreshold swing($S.S.(\text{mV}/\text{decade})$)] are summarized in the inset table.

Though the current-voltage model of OTFTs is still not well-developed, formula borrowed from MOSFET are widely used to analyze OTFT characteristics from macroscopic point of views[22, 23]. In linear region, drain current (I_d) can be expressed as Eq. (2.3)[22]:

$$I_d = \frac{W\mu}{L} C_i \left[(V_g - V_{th}) \cdot V_d - \frac{1}{2} V_d^2 \right] \quad (5.3)$$

Typical parameters extracted from transfer characteristics are listed in inset of **Figure 5.4**. V_{th} of UV-OTFTs was more positive than that of STD-OTFTs. A plausible explanation is that the UV-treated PMMA produces excess negatively charges that enhanced the accumulation of holes. Accordingly, compared with STD-OTFTs subthreshold swing ($S.S.$) was enlarged and the V_{th} was positively shifted. It may due to the change of functional end-groups (from $-\text{CH}_3$ to $-\text{COOOH}$) produced by UV-treatment on PMMA surface, which will result in the negative charged-states near PMMA surface. **Figure 5.5 (a)** and **(b)** compares the energy-band diagram of STD-OTFTs and UV-OTFTs, respectively.

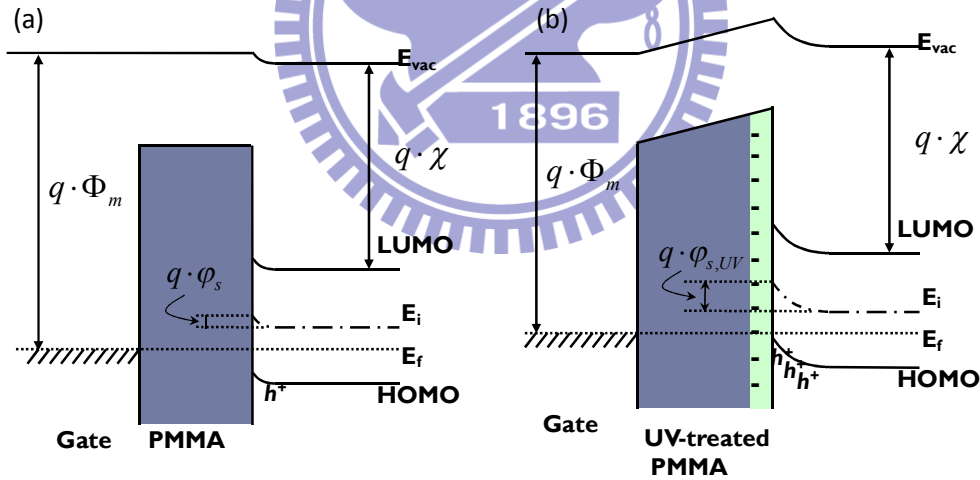


Figure 5.5 Energy-band diagram of (a) STD-OTFTs and (b) UV-OTFTs.

The negative charge sites, which produced by UV treatment, caused a surface potential changed that induced a bending of the HOMO level at the interface and increased the carrier density in the channel. These results are consistent with

previously reported data [24]. Both STD- and UV-OTFTs exhibited a mobility (μ) around $0.3 \text{ cm}^2/\text{Vs}$ (inset table of Figure 1), indicating that the pentacene film structure and the carrier transport were not significantly affected following UV treatment. **Figures 5.6 (a) and (b)** are the AFM images of pentacene film deposited on PMMA and UV-treated PMMA, respectively. We can find that the grains and roughness were almost the same.

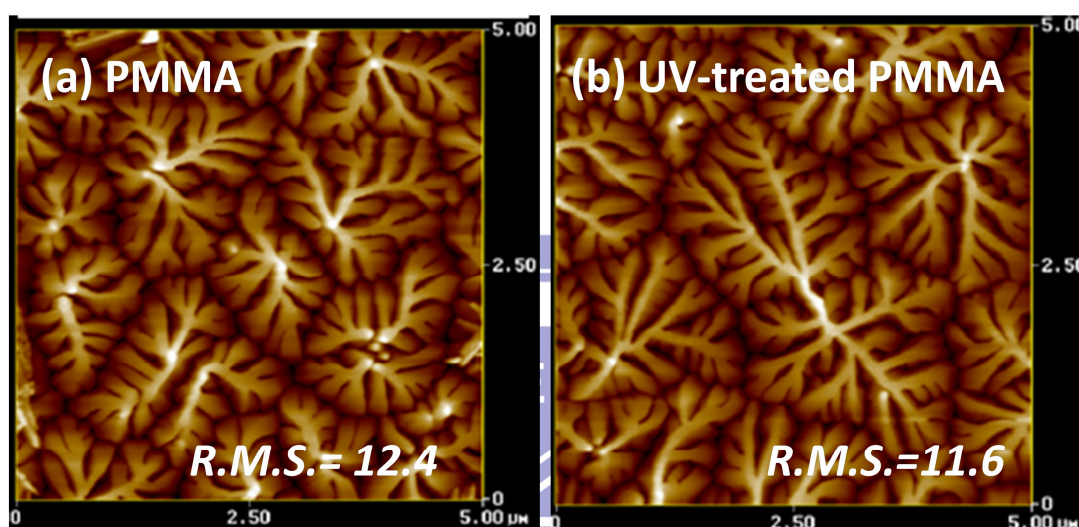


Figure 5.6 The AFM images of pentacene film deposited on PMMA and UV-treated PMMA, respectively.

5.4.2. Gas Diffusion Model

Figures 5.7 (a) and (b) presents the transfer characteristics of STD-OTFTs and UV-OTFTs under 1 ppm NH_3 condition with period time of 500 sec.

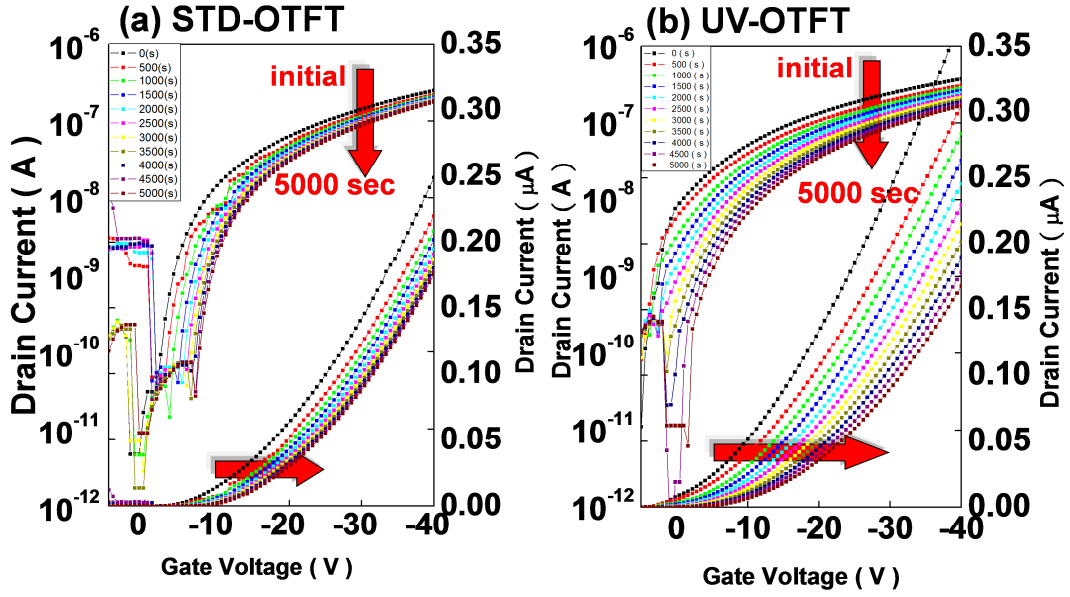


Figure 5.7 The transfer characteristics of (a) STD-OTFTs and (b) UV-OTFTs under 1 ppm NH_3 condition with period time of 500 sec.

The responses of STD- and UV-OTFTs to nitrogen ambient and to 1-ppm ammonia gas in nitrogen ambient as a function of sensing time were determined, respectively. Four typical parameters (turn-on current, intrinsic mobility, V_{th} , and $S.S.$) were extracted and plotted as a function of sensing time as shown in **Figure 5.8**. Both STD- and UV-OTFTs keep almost unchanged characteristics in nitrogen ambient. In the presence of 1-ppm ammonia gas, significant variations of the turn-on current, intrinsic mobility, and V_{th} were observed while $S.S.$ was almost unchanged. The turn-on current variation (I_d/I_{d0}), according to **Eq. (5.3)**, is affected by both threshold voltage shift (ΔV_{th}) and mobility variation (μ/μ_0), where I_{d0} and μ_0 are the initial drain current and the initial field-effect mobility. $S.S.$ is usually referred to the interface trap density[25] and constant $S.S.$ indicated that 1-ppm NH_3 did not drastically change the interface trap density of the device.

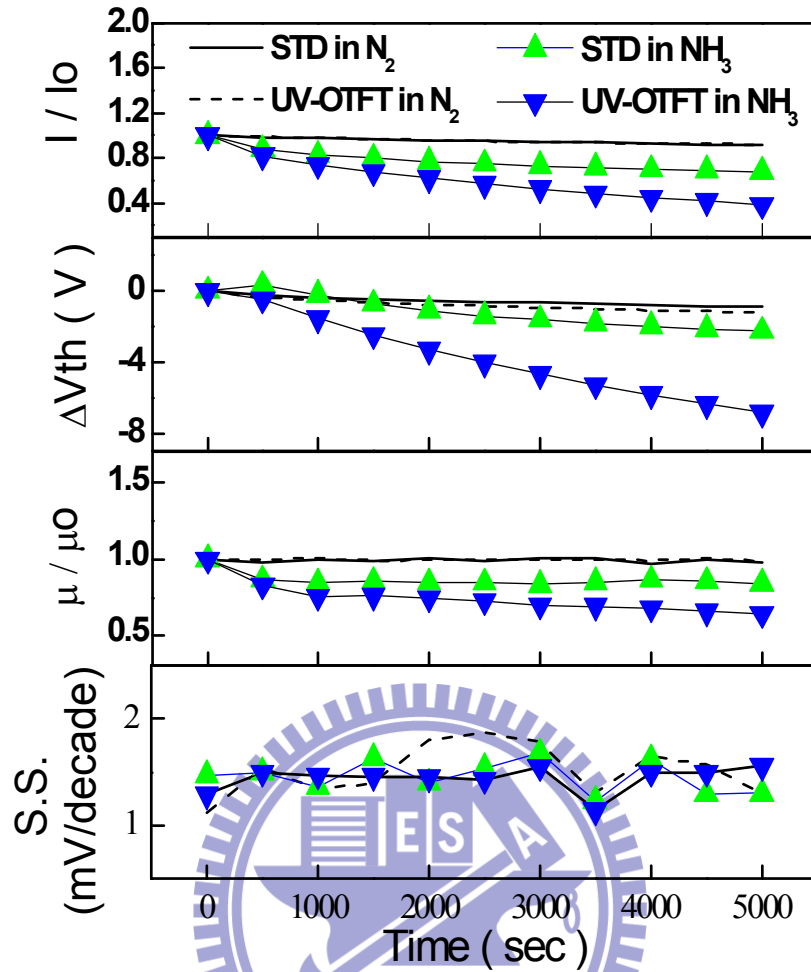


Figure 5.8 Ammonia sensing responses of OTFTs with multi-parameters. The multi-parameters, I/I_0 (turn on current variation), ΔV_{th} (threshold voltage shift), μ/μ_0 (mobility variation), and S.S. (subthreshold swing), of standard (STD) and UV-treated OTFTs are plotted as a function of time in N_2 and NH_3 (1ppm) ambiances. Each data point was extracted from the transfer characteristics measured at $V_g=-40V$, $V_d=-3V$ with the interval of 500 sec within a total sensing time of 5000 sec.

Figure 5.9 shows that when ammonia molecules diffuse into the active layer through grain boundaries, the decrease in mobility may result from the increase of scattering centers or the increase of energy barrier for charge transport. It was reported that the polar molecules disturb charge transport in organic materials by increasing the amount of energetic disorder through charge-dipole interactions[26]. Because the concentration of ammonia was fixed, the mobility decreased could be saturated. Therefore, after exposing to 1-ppm ammonia gas for 1000 sec, mobility of

STD-OTFT and UV-OTFT degraded about 20% and 30%, respectively. However, the threshold voltage shifted was decreased gradually. The reason may be the hole-traps, which were attributed to the NH_3 or NH_4^+ near dielectric interface and caused lower concentration of gate-induced mobile carriers [27].

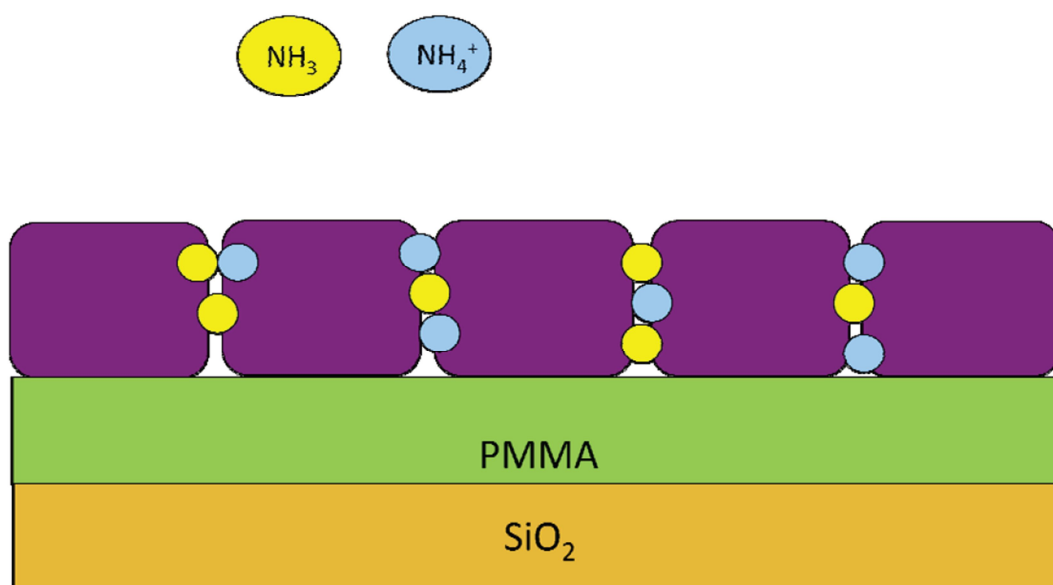


Figure 5.9 When ammonia molecules diffuse into the active layer through grain boundaries, the decrease in mobility may result from the increase of scattering centers or the increase of energy barrier for charge transport. It was reported that the polar molecules disturb charge transport in organic materials by increasing the amount of energetic disorder through charge-dipole interactions.

Figure 5.10 shows the hole-traps near the dielectric interface. This result implied that the increased dipole moment on PMMA surface following UV treatment may facilitate the absorption of ammonia molecules.

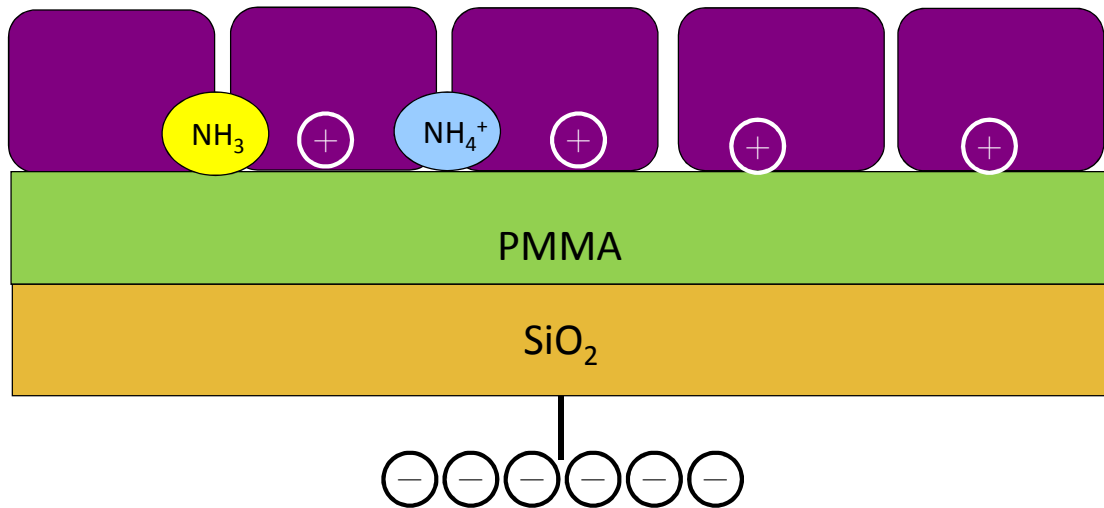


Figure 5.10 The hole-traps, which were attributed to the NH_3 or NH_4^+ near dielectric interface and caused lower concentration of gate-induced mobile carriers.

5.4.3. Ammonia Concentration Effect

To confirm the gas sensing model, we exposed the devices to different ammonia concentration from 0.5ppm to 5ppm. **Figures 5.11 (a) and (b)** shows the threshold voltage shift and mobility variation as function of different ammonia concentration measured in different time (1000 seconds and 2000 seconds). It obviously shows that the threshold voltage shift and mobility variation were increased with the increasing of ammonia concentration, which caused more NH_4^+ or NH_3 penetrate through the grain boundaries of pentacene film. We can also find that the threshold voltage shifted of 2000 seconds is more than 1000 seconds. However, the mobility variation did not change as a function of time. The phenomenon conformed to the gas sensing model we mentioned above. For application to non-invasive diagnostic sensor for cirrhotic patients, it is necessary to monitor ammonia concentration at 0.5 ppm or lower so that the breath samples between healthy person (breath ammonia level: 0.278 ppm) and a patient (breath ammonia level: 0.745 ppm) can be distinguished [5]. For the patients with renal failure, we need to monitor ammonia concentration at 1 ppm (relieve) to 5 ppm (dangerous) [28]. However, it was hard to distinguish the variation difference

between 0.5 ppm and 1 ppm ammonia with the STD-OTFTs. Thus, we need to find another solution to improve the sensing ability.

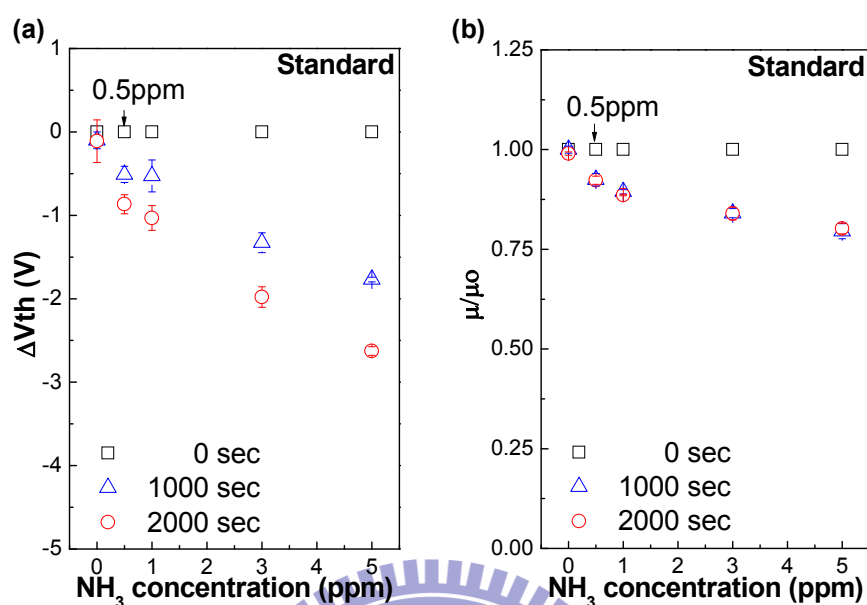


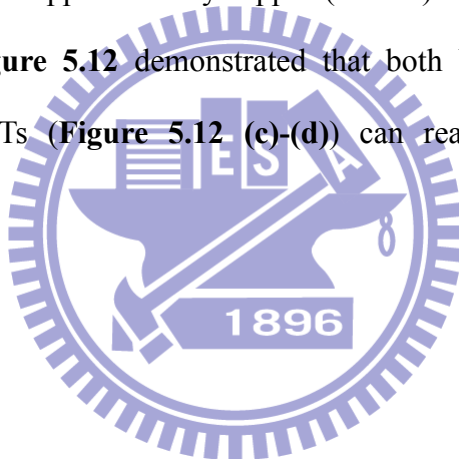
Figure 5.11 Concentration dependent ammonia sensing response. (a) Threshold voltage shift and (b) mobility variations for STD-OTFTs are shown when devices were exposed to NH_3 with concentrations varied from 0 ppm to 5 ppm. Sensing periods were fixed at 1000 sec and 2000 sec. Each data was the average of three independent measurements.

5.4.4. Sensing Phenomenon of UV-OTFTs

We measured the UV-OTFTs at the same condition. After extracting the parameters from I-V curve, the threshold voltage was more negatively shifted; the mobility and drain current were also decreased more than compared STD-OTFTs. **Figures 5.12 (a) and (b)** compares the threshold voltage shift and mobility variation of STD-OTFTs and of UV-OTFTs as a function of sensing time in NH_3 (1 ppm) and N_2 ambiances, respectively. We proposed that UV radiation increased the dipole moment of dielectric surface and attracted ammonia gas molecules to accumulate near the dielectric surface. Also, the negative charge sites which caused by UV treatment enhanced the attraction of positive ammonia ions (NH_4^+), therefore gave stronger electric responses on UV-OTFTs than those of STD-OTFTs. The variation of mobility

and threshold voltage shifted between 0.5 ppm and 1 ppm ammonia can be distinguished. Therefore, after UV treatment, PMMA surface becomes more hydrophilic and may attract more ammonia.

The variation of μ/μ_0 and ΔV_{th} to ammonia concentration indicated that the difference of less than 0.5 ppm ammonia can be clearly distinguished by UV-OTFTs. As a non-invasive diagnostic sensor for cirrhotic patients, it is necessary to monitor ammonia concentration at 0.5 ppm or lower so that the breath samples between healthy person (breath ammonia level: 0.278 ppm) and a patient (breath ammonia level: 0.745 ppm)[5] can be distinguished. For the patients with renal failure, the target ammonia levels are approximately 1 ppm (relieve) to 5 ppm (dangerous)[28]. Our data shown in **Figure 5.12** demonstrated that both UV-OTFTs (**Figure 5.12 (a)-(b)**) and STD-OTFTs (**Figure 5.12 (c)-(d)**) can reach this requirement for ammonia sensitivity.



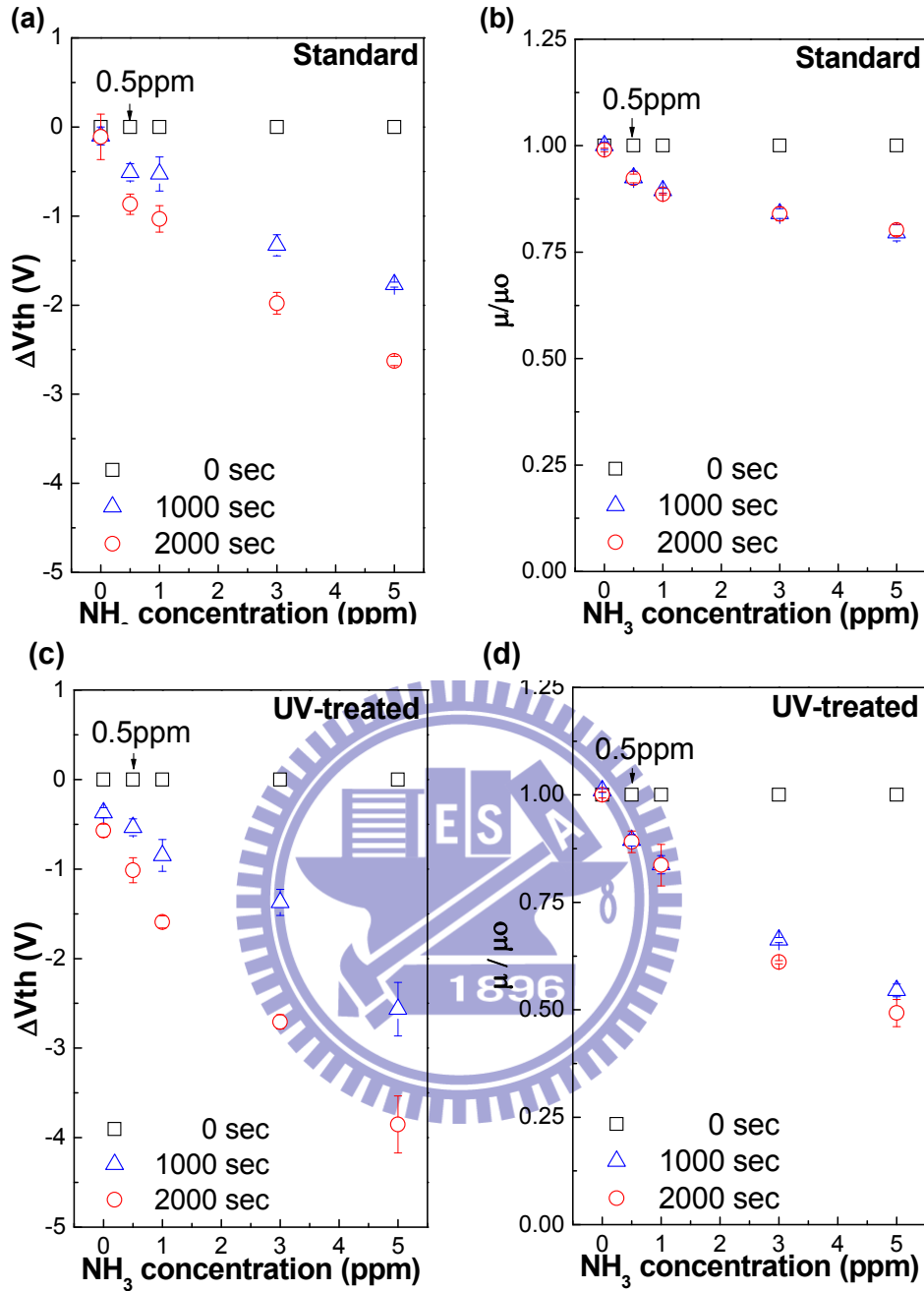


Figure 5.12 Concentration dependent ammonia sensing response. (a) Threshold voltage shift and (b) mobility variations for STD-OTFTs are shown when devices were exposed to NH₃ with concentrations varied from 0 ppm to 5 ppm. (c) Threshold voltage shift and (d) mobility variations for UV-OTFTs are shown when devices were exposed to NH₃ with concentrations varied from 0 ppm to 5 ppm. Sensing periods were fixed at 1000 sec and 2000 sec. Each data was the average of three independent measurements.

5.4.5. Selectivity of Gas Sensing

The specificity of OTFT as gas sensor was further investigated with some gases

that may exist in human breath or may interfere with ammonia sensing. The effects of carbon dioxide (CO_2), alcohol ($\text{C}_2\text{H}_5\text{OH}$), methane (CH_4), and acetone (CH_3COCH_3) on μ/μ_0 and ΔV_{th} of UV- and STD-OTFTs were shown in **Figure 5.13 (a)-(b)** and **Figure 5.13 (c)-(d)**, respectively. These gases were relatively inert to OTFTs and only ammonia caused significant variation in both μ/μ_0 and ΔV_{th} .

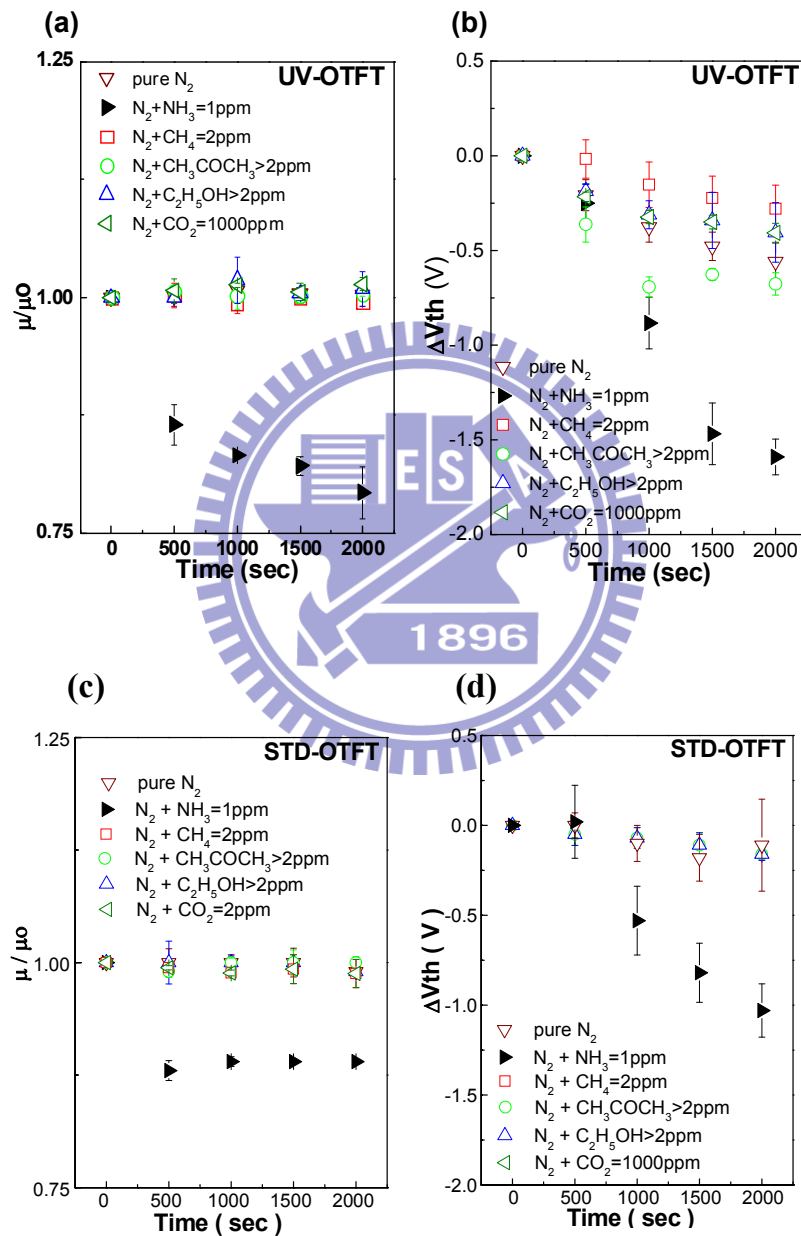


Figure 5.13 Target dependent OTFT responses. (a) and (b) Variations of μ/μ_0 and ΔV_{th} as a function of sensing time for UV-OTFTs. (c) and (d) Variations of μ/μ_0 and ΔV_{th} as a function of sensing time for STD-OTFTs. Each data was the average of three independent measurements.

5.4.6. Phenomenon of Recovery

In order to verify the sensing mechanism, we discuss the phenomenon of recovery. At 0 second, both the standard and UV-treated devices were exposed to nitrogen. Then, during 0 to 3000 seconds, the devices were exposed to 0 ppm (nitrogen), 1 ppm, 3 ppm, 5ppm ammonia gas individually. After that, during 3000 to 4500 seconds, the ambience was purged with nitrogen. From **Figures 5.14 (a) and (b)**, we can find that the mobility of both the STD-OTFTs and UV-OTFTs can be recovery.

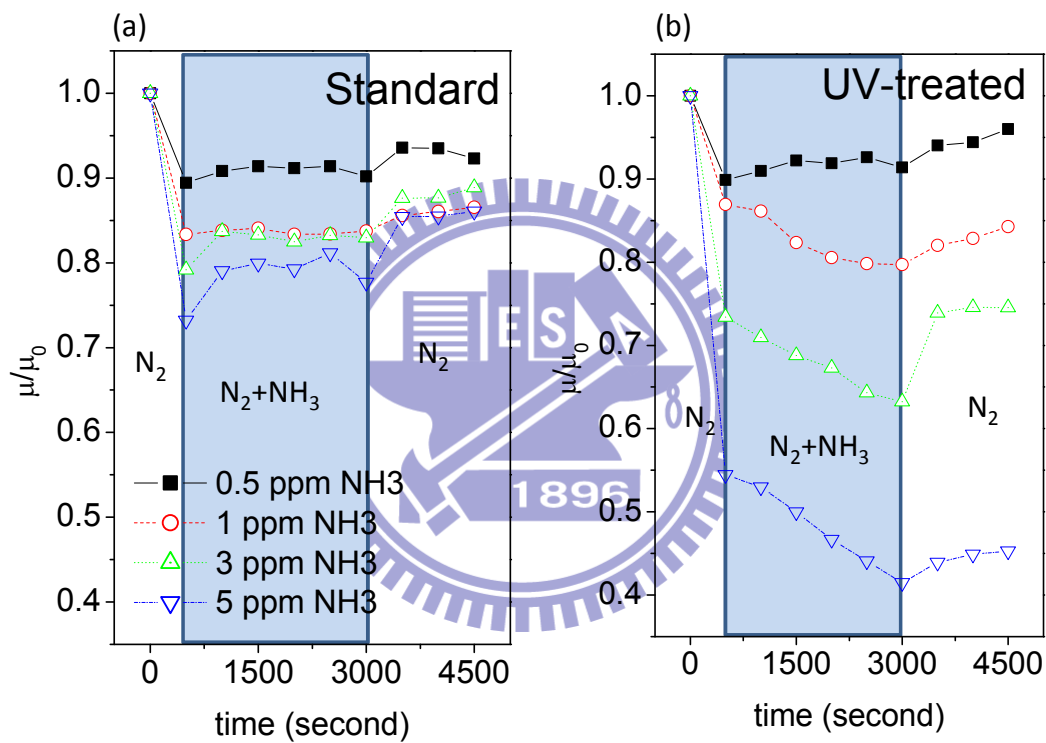


Figure 5.14 Recovery dependent ammonia sensing response. Mobility variation of (a) STD-OTFTs and (b) UV-OTFTs as a function of sensing time. Each data point was extracted from the transfer characteristics measured at $V_g=-40V$, $V_d=-3V$ with the interval of 500 sec within a total sensing time of 4500 sec.

Although the value could not recover to the beginning, the phenomenon were immediately when the ammonia was purged out. The recovery of mobility may due to the decreasing of ammonia which may create scattering centers or traps [26].

However, from **Figures 5.15 (a) and (b)**, the threshold voltage shift of both devices did not have evident recovery. Although the slope of threshold voltage shift was gradual when the ammonia was purged out, the value could not be increased. The reason may be that the ammonia molecular NH_3 or ammonia ions NH_4^+ had been trapped on the interface of the dielectric and pentacene layer. Thus, the reaction could not be reversed.

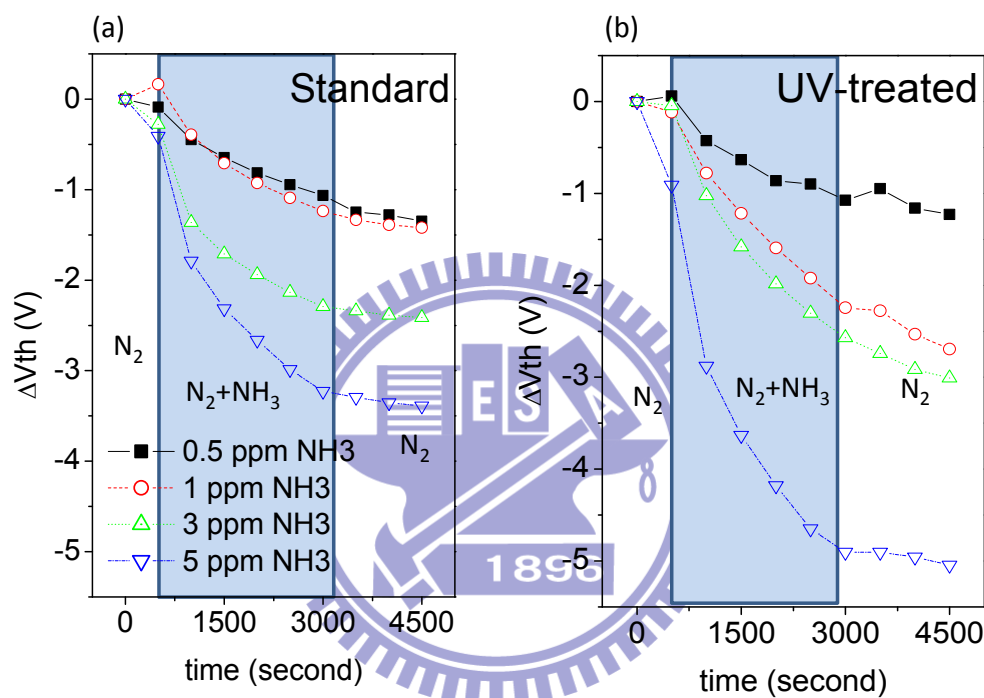


Figure 5.15 Recovery dependent ammonia sensing response. Threshold voltage shifted of (a) STD-OTFTs and (b) UV-OTFTs as a function of sensing time. Each data point was extracted from the transfer characteristics measured at $V_g = -40\text{V}$, $V_d = -3\text{V}$ with the interval of 500 sec within a total sensing time of 4500 sec.

5.4.7. Humidity Effect

The most sensitive parameter of OTFT for ammonia sensing was threshold voltage shift (ΔV_{th}) as described above. ΔV_{th} was proposed to relate to the polar molecules screen the vertical electric at the channel, UV-OTFTs especially. In aqueous environment, uncharged ammonia (NH_3) gas become positively charged ammonium ions (NH_4^+). It is reasonable to expect that ammonia molecules convert to

NH_4^+ when reacting with moisture in ambience or in organic active layer and humidity may contribute to the sensitivity of ammonia sensing by OTFTs. RH gave opposite effects (shown as dash lines in **Figure 5.16**) to the sensitivity of ammonia sensing when ΔV_{th} and μ/μ_0 were used as sensing parameters of OTFT devices. Higher RH increased ΔV_{th} but decreased μ/μ_0 in the absence of ammonia (at 0 ppm). These results are consistent with previous reports[29] that the more positive threshold voltage in the absence of ammonia was because water vapor induced more mobile charges in the organic semiconductor layer (water molecules doping effect). Therefore, a large positive gate bias was needed to compensate for the holes in the channel and to turn off the device[30]. The reduction of carrier mobility was because polar water molecules residing at grain boundaries interact with hole carriers. Scattering effect or the field screening effect may be the plausible mechanism to describe interactions between polar water molecules and carriers.

The water molecules doping effect described above was diminishing in the presence of ammonia. The humidity effect on ΔV_{th} represented by $\Delta V_{\text{th,RH=50\%}} - \Delta V_{\text{th,RH<20\%}}$ became more pronounced when ammonia concentration increased from 1 ppm to 5 ppm as shown in **Figure 5.16 (a)**. A possible reason was that water molecules react with ammonia to form ammonium ions (NH_4^+) and suppress the water doping effect. The opposite effect of water and ammonium ion on ΔV_{th} made it a sensitive parameter for ammonia sensing at higher RH. Carrier mobility of OTFT was influenced by RH in a different manner (**Figure 5.16 (b)**). The ammonia effect on mobility of OTFT was not significantly influenced by the RH. The humidity effect on μ/μ_0 represented by $|\mu/\mu_{0,\text{RH=50\%}} - \mu/\mu_{0,\text{RH<20\%}}|$ was relatively constant when ammonia concentration was increased from 1 ppm to 5 ppm.

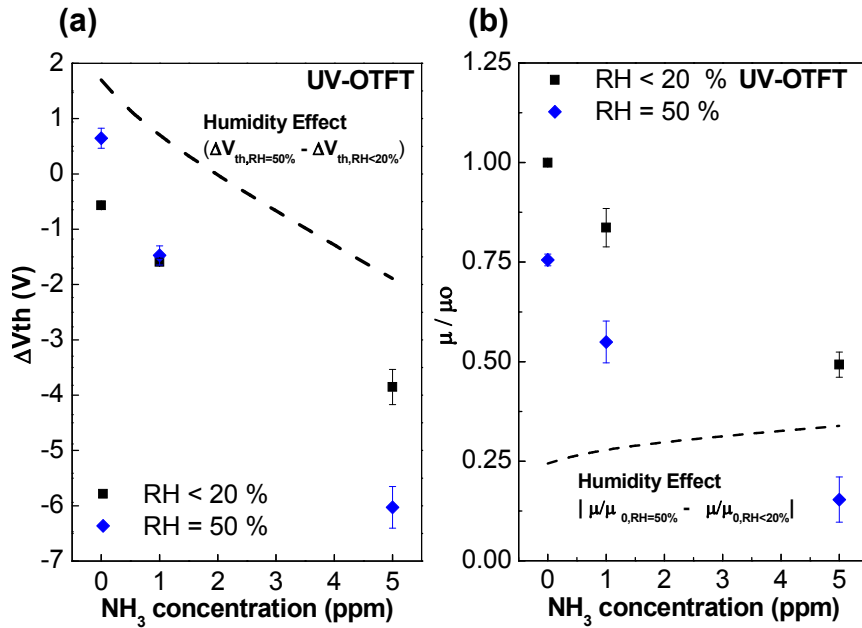


Figure 5.16 Humidity effect on ammonia sensing using UV-OTFTs.. (a) ΔV_{th} and (b) μ/μ_0 of UV-OTFTs were determined when devices were exposed to different concentrations of NH_3 gas with RH less than 20% or equal to 50%. Humidity effect (shown as dashed lines) is defined as $\Delta V_{th,RH=50\%} - \Delta V_{th,RH<20\%}$ and $|\mu/\mu_{0,RH=50\%} - \mu/\mu_{0,RH<20\%}|$ for ΔV_{th} and μ/μ_0 , respectively. The sensing time was fixed at 2000 sec. RH of the sealed sensing chamber was controlled at RH < 20% and RH = 50%, respectively. Each data was the average of three independent measurements by using three samples with identical initial characteristics.

5.5. Conclusions

A pentacene-based OTFT is shown to be highly sensitive for ammonia sensing from 0.5 to 5 ppm, a critical range for the diagnosis of patients with chronic liver diseases and renal failure. This demonstrated that OTFT devices, which can be fabricated by simple and cheap process and exhibited channel length and width as large as several hundreds of microns, are useful as non-invasive biomedical sensors. This is on the contrary to inorganic MOSFET devices that require high fabrication cost and complicated fabrication process and the dimension of the devices has to be scaled down to the range of nanometers to increase the gas sensing sensitivity. The sensitivity and selectivity of OTFTs as gas sensor can be further improved by the

modification of the PMMA dielectric layer, selecting suitable measuring parameters and providing additional local electric field. Due to the simple fabrication processes of the devices, OTFTs are promising to be developed to a portable and disposable gas sensor.

References

- [1] R. B. Northrop, “Noninvasive instrumentation and measurement in medical diagnosis” *The Biomedical Engineering*, 1st ed; CRC Press: New York, (2002).
- [2] J. P. Conkle, B. J. Camp, B. E. Welch, “Trace composition of human respiratory gas” *Arch. Environ. Health*. 30, 290-295, (1975).
- [3] W.D. Chey, B.C. Wong “American College of Gastroenterology guideline on the management of Helicobacter pylori infection” *American Journal of Gastroenterology*. 102, 1808–1825, (2007).
- [4] Q. Zhang, P. Wang, J. Li, X. Gao, “Diagnosis of diabetes by image detection of breath using gas-sensitive IAPS” *Biosens. Bioelectron*. 15, 249, (2010).
- [5] C. Shimamoto, I. Hirata, K. Katsu, “Breath and blood ammonia in liver cirrhosis” *Hepato-Gastroenteral*. 47, 443, (2000).
- [6] S. Davies, P. Spanel, D. Smith, “Quantitative analysis of ammonia on the breath of patients in end-stage renal failure” *Kidney International*. 52, 233, (1997).
- [7] G. K. Prasad, T. P. Radhakrishnan, D. Sravan Kumar, M. G. Hanashyam Krishna, “Ammonia sensing characteristics of thin film based on polyelectrolyte templated polyaniline” *Sens. Actuators B*. 28, 106 626–631, (2005).
- [8] B. Timmer, W. Olthuis, V. D. B. Albert, “Ammonia sensors and their applications—a review” *Sens. Actuators B*. 107, 666–677, (2005).
- [9] B. Crone, A. Dodabalapur, A. Gelperin, L. Torsi, H. E. Katz, A. J. Lovinger, Z.

- Bao, "Electronic sensing of vapors with organic transistors" *Appl. Phys. Lett.* **78**, 2229, (2001).
- [10] J. T. Mabeck, G. G. Malliaras, "Chemical and biological sensors based on organic thin-film transistors" *Anal. Bioanal. Chem.* **384**, 343-353, (2006).
- [11] T. Someya, A. Dodabalapur, H. E. Gelperin, Z. B. Katz, "Integration and response of organic electronics with aqueous microfluidics" *Langmuir*. **18**, 5299-5302, (2002).
- [12] D. H. Dunlap, P. E. Parris, V. M. Kenkre, "Charge-dipole model for the universal field dependence of mobilities in molecularly doped polymers" *Phys. Rev. Lett.* **77**, 542, (1996).
- [13] D. J. Gundlach, T. N. Jackson, D. G. Schlom, S. F. Nelson, "Solvent-induced phase transition in thermally evaporated pentacene films" *Appl. Phys. Lett.* **74**, 3302, (1999).
- [14] T. Someya, H. E. Katz, A. Gelperin, A. J. Lovinger and A. Dodabalapur, "Vapor sensing with α,ω -dihexylquarterthiophene field-effect transistors: The role of grain boundaries" *Appl. Phys. Lett.* **81**, 3079-3081, (2002b).
- [15] L. Torsi, A. Dodabalapur, L. Sabbatini and P. G. Zambonin, "Multi-parameter gas sensors based on organic thin-film-transistors" *Sens. Actuatr B.* **67**, 312-316, (2000).
- [16] J. Locklin and Z. Bao, "Effect of morphology on organic thin film transistor sensors" *Anal. Bioanal. Chem.* **384**, 336-342, (2006).
- [17] L. Wang, D. Fine, D. Sharma, L. Torsi and A. Dodabalapur, "Nanoscale organic and polymeric field-effect transistors as chemical sensors" *Anal. Bioanal. Chem.* **384**, 310-320, (2006).
- [18] A. Assadi, G. Gustafsson, M. Willander, C. Svensson and O. Inganas, "Determination of field-effect mobility of poly (3-hexylthiophene) upon exposure to NH₃ gas" *Synth. Met.* **37**, 123-130, (1990).

- [19] M. J. Powell, "Charge trapping instabilities in amorphous silicon-silicon nitride thin-film transistors" *Appl. Phys. Lett.* 43, 597-599, (1983).
- [20] H. L. Cheng, Y. S. Mai, W. Y. Chou, and L. R. Chang, "Influence of molecular structure and microstructure on device performance of polycrystalline pentacene thin-film transistors" *Appl. Phys. Lett.* 90, 171926, (2007).
- [21] C. D. Dimitrakopoulos, A. R. Brown, A. Pomp, "Molecular beam deposited thin films of pentacene for organic field effect transistor applications" *J. Appl. Phys.* 80, 2501, (1996).
- [22] C. Kim, A. Facchetti, T. J. Marks, "Polymer gate dielectric surface viscoelasticity modulates pentacene transistor performance" *Science* 318, 76, (2007)
- [23] H. Yan, Z. H. Chen, 1, Y. Zheng, C. Newman, J. R. Quinn, F. Dötz, M. Kastler, and A. Facchetti, "A high-mobility electron-transporting polymer for printed transistors" *Nature* 457, 679, (2009).
- [24] I. Lundström, S. Shivaraman, C. Svensson, L. Lundkvist, "A hydrogen-sensitive MOS field-effect transistor" *Appl. Phys. Lett.* 26, 55, (1975).
- [25] J. Takeya, T. Nishikawa, T. Takenobu, S. Kobayashi, Y. Iwaea, T. Mitani, "Effects of polarized organosilane self-assembled monolayers on organic single-crystal field-effect transistors" *Appl. Phys. Lett.* 85, 5078, (2004)
- [26] D. J. Gundlach, T. N. Jackson, D. G. Schlön, and S. F. Nelson, "Solvent-induced phase transition in thermally evaporated pentacene films" *Appl. Phys. Lett.* 74, 3302, (1999).
- [27] S. V. Novikov, D. H. Dunlap, V. M. Kenkre, P. E. Parris, and A. V. Vannikov, "Essential role of correlations in governing charge transport in disordered organic materials" *Phys. Rev. Lett.* 81, 4472, (1998)
- [28] A. Manolis, "The Diagnostic Potential of Breath Analysis" *Clin. Chem.* 29, 5, (1983).

- [29] H.-W. Zan, S.-C. Kao, “New Organic Phototransistor With Bias-Modulated Photosensitivity and Bias-Enhanced Memory Effect” *IEEE Trans. Electron Devices*, 30, 721-723, (2009).
- [30] A. R. Völkel, R. A. Street, and D. Knipp, “Carrier transport and density of state distributions in pentacene transistors” *Phys. Rev. B* 2002. 66, 195336, (2002).
- [31] S. Scheinert, G. Paasch, M. Schrodner, H. -K. Roth, S. Sensfuss, Th. Doll, “Subthreshold characteristics of field effect transistors based on poly(3-dodecylthiophene) and an organic insulator” *J. Appl. Phys.* 92, 330, (2002).
- [32] K. P. Pernstich, S. Haas, D. Oberhoff, C. Goldmann, D. J. Gundlach, B. Batlogg, A. N. Rashid, G. Schitter, “Threshold voltage shift in organic field effect transistors by dipole monolayers on the gate insulator” *J. Appl. Phys.* 96, 6431, (2004).
- [33] J. Takeya, T. Nishikawa, T. Takenobu, S. Kobayashi, Y. Iwasa, T. Mitani, C. Goldmann, C. Krellner, B. Batlogg, “Effects of polarized organosilane self-assembled monolayers on organic single-crystal field-effect transistors” *Appl. Phys. Lett.* 85, 5078, (2004).
- [34] Y. S. Yang, S. H. Kim, S. C. Lim, J. -I. Lee, J. H. Lee, L. -M. Do, T. Zyung, “Electric characteristics of poly(3-hexylthiophene) organic field-effect transistors fabricated on O₂ plasma-treated substrates” *Appl. Phys. Lett.* 83, 3939, (2003)
- [35] D. Li, E. J. Borkent, R. Nortrup, H. Moon, H. Katz, and Z. Bao, “Humidity effect on electrical performance of organic thin-film transistors” *Appl. Phys. Lett.* 86, 042105, (2005).
- [36] K. N. Narayanan Unni, D. S. Sylvie, J. M. Nunzi, “Improved performance of pentacene field-effect transistors using a polyimide gate dielectric layer” *J. Phys. D: Appl. Phys.* 38, 1148, (2005).
- [37] S. H. Kim, H. Yang, S. Y. Yang, K. Hong, D. Choi, C. Yang, D. S. Chung, and C.E. Park, “Effect of water in ambient air on hysteresis in pentacene field-effect

transistors containing gate dielectrics coated with polymers with different functional groups” *Organic electronics* 9, 673-677, (2008).

[38] D. H. Dunlap, P. E. Parris, and V. M. Kenkre, “Charge-dipole model for the universal field dependence of mobilities in molecularly doped polymers” *Phys. Rev. Lett.* 77, 542, (1996).

[39] D. Zou and T. Tsutsui, “Voltage shift phenomena introduced by reverse-bias application in multilayer organic light emitting diodes” *J. Appl. Phys.* 87, 1951, (2000).



Chapter 6. Low Operated Polymer Vertical Transistors with High On/Off Current Ratio

6.1. Introduction

Since the late 19th century, scientists have researched technologies that provide electronic switch and signal amplifier. The vacuum tube is a triode with a hot cathode, plate anode, and a controlling grid inside an evacuated glass tube. Yet even today, vacuum tubes survive in specialist areas, including high-power applications, audio amplifiers, and in military applications due to its resistance to electromagnetic pulse. It is thus interesting to ask whether the vacuum tube concept can see a revival in this era of solid-state electronics, and once again prove its unique advantages. Attempts during the 1950s and 1960s, to build vacuum tubes using inorganic semiconductors, proved unsuccessful because of difficulties with the dopant diffusion process in forming the grid structure.[1],[2] Several reports, since the 1990s, describe research into intrinsic organic semiconductor designs that deliver vacuum tube functionality.[3],[4] Fabrication of the grid, by deposition through a shadow mask, with openings on the micron-scale, results in poor current density and on/off ratio.[3] Improvements in grid design, using high density nanometer scale openings increased output current density to greater than 1 mA/cm^2 , [5],[6] sufficient for most applications. The difficulty regarding the on/off ratio of solid state vacuum tubes lies in the large spatial overlap between the grid and collector electrode. In an early solid-state device design,[6] the on/off ratio was only 10^2 ; recently we raised it to 10^4 by introducing an insulator to surround the grid, this being the generally accepted ratio required for practical applications.[7] **Figure 6.1** compares three representative structures of latest organic vertical transistors.

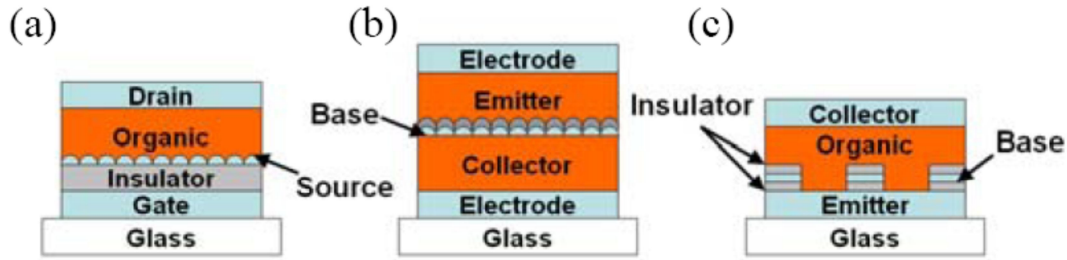


Figure 6.1 Schematic device structures. (a) Vertical transistor with rough source metal [8]. (b) Vertical transistor with thin or porous base metal [9],[10]. (c) Vertical transistor which named as “SCLT”. The base metal is embedded in organic layer surrounded with insulator.

Structure A as shown in **Figure 6.1(a)** has one organic layer between source and drain metal. Thin (17 nm in Ref.[8]) and rough source metal is required to enable the gate field penetration. Structure B in **Figure 6.1(b)** is similar to a vertical bipolar transistor, thin (8 nm in Ref.[9]) or porous (Ref.[10]) base metal is needed to enable current flow. Structures A and B have difficulty in thin-metal process control. In our study, a simple structure (structure C) as shown in **Figure 6.1(c)** is used. This is an improved structure based on previous studies [11], [12]. The organic layer is sandwiched between emitter and collector metals to form a simple diode. The base control is realized by a grid metal with high-density holes patterned by the spontaneous patterning of higher order nanostructures (SPHOS). The grid metal is well isolated from emitter and collector metals by putting insulators above and beneath the grid metal. In this study, low operated voltage solution-processed polymer vertical transistor with on/off current ratio higher than 2×10^4 is firstly demonstrated. The channel length is 200 nm. A new structure is used to perform reliable leakage control. Significant impacts of thin film morphology and metal doping effect on the leakage current of organic vertical transistors are firstly observed and recognized as two new leakage phenomena. The complete leakage control and the reliable process in our

report enable polymer vertical transistors for real applications.

6.2. Experiment

6.2.1. Device Fabrication Process

Figure 6.2 shows the structure of space-charge-limited transistors (SCLT). In this device, the Au, SiO_x, middle Al, and top Al is utilized as emitter, insulator, base, collector, respectively. The function of bottom silicon oxide (SiO_x) was used to block the leakage current between Al and Au; and the function of top (SiO_x) is used to block the leakage current between Al and Al.

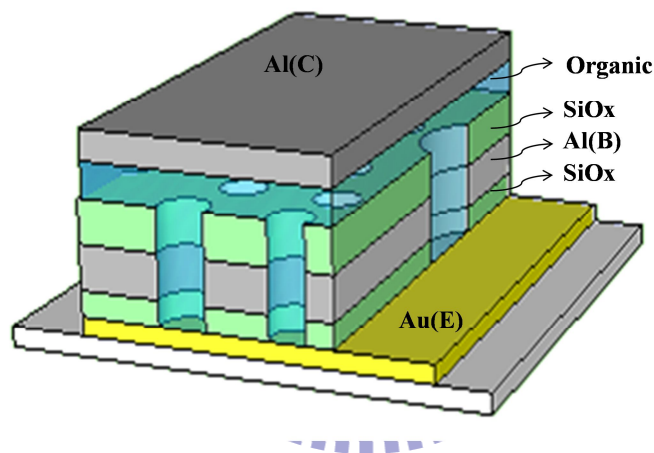


Figure 6.2 The structure of the proposed vertical transistor.

Figure 6.3 shows the process flow of the vertical transistor proposed in this work.

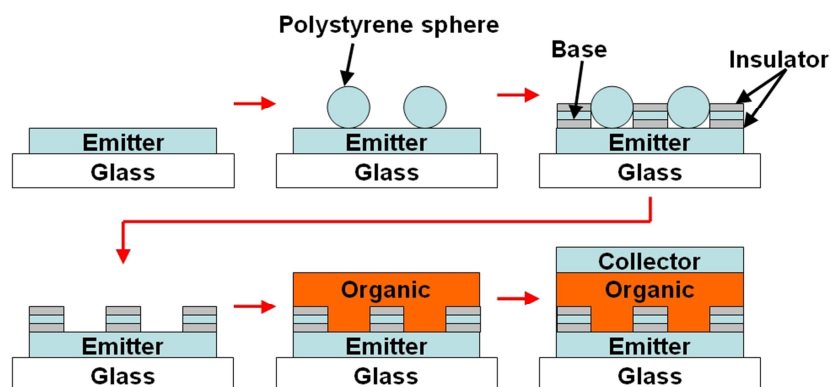
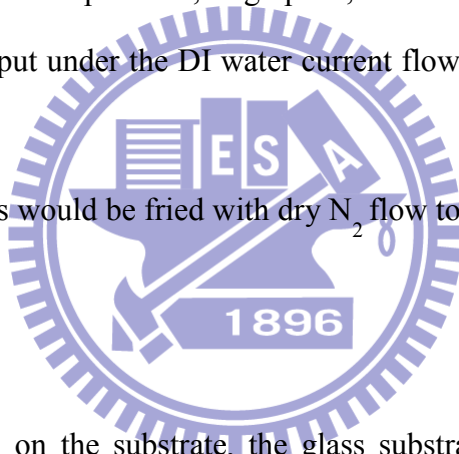


Figure 6.3 The process flow of the vertical transistor.

Glass substrate (CORNING Eagle 2000) must keep clean or films may become rough. The rough surface would cause point discharge between the insulator and metal. The steps of clean glass substrate are shown follow.

Steps:

- (1) De Ion (DI) water current flows for 5 minutes in order to remove the particles.
- (2) The substrates should be placed under the in the acetone and ultrasonic resonance for 5 minutes in order to remove the organic pollution. Then, the substrates have to put under the DI water current flow for 5 minutes in order to remove the solvent.
- (4) The substrates were put in the KG detergent bath with ultrasonic resonance for 5 minutes in order to remove the particles, fingerprint, and ionic.
- (5) The substrates were put under the DI water current flow for 5 minutes in order to remove the solvent.
- (6) Finally, the substrates would be fried with dry N_2 flow to blow off the water on the substrates.



Before deposition metal on the substrate, the glass substrates were exposed to the UV-light by UVO_3 clean machine that keep the substrate surface clean. Nickel(99.99%) was deposited to increase the adhesion of the Gold by thermal evaporator. The deposition rate was controlled at $1\text{\AA}/\text{sec}$ and the thickness of nickel was about 100\AA . After deposition of adhesion layer, Gold (99.99%) was deposited by thermal evaporator. Both of two processes the deposition pressure was started at 5×10^{-6} torr and the substrates temperature fixed at 50°C . The metal region was defined through shadow mask.

It could fabricate a microstructure in the lateral direction within a large scale organic device using non-photolithographic processes according to Spontaneous

Patterning of Higher Order Structures' (SPHOS) [13],[14]. Colloidal lithography [15], one of the techniques adopted in the SPHOS forms porous films by removing particles after the film deposition. Positively charged polystyrene particles shown in **Figure 6.4(a)** (200 nm, tetramethylammonium latex) were adsorbed onto the substrates from dispersion by electrostatic interactions. Particles concentration diluted with ethanol to 0.6 wt%. **Figure 6.4(b)** shows polystyrene spheres are absorbed on the Au film surface. After the $\text{SiO}_x/\text{Al}/\text{SiO}_x$ deposition, the polystyrene spheres are removed by an adhesive tape (Scotch, 3M) without damage to the base metal. The images of the Al grid with 2000 Å opening diameter are shown in **Figure 6.4(c)**. The key procedure in this fabrication is that the substrate is then transferred to a beaker with boiling isopropanol solution for ten seconds. Similar to the method of Fujimoto et al [5], the substrate is finally blown dry immediately in a unidirectional nitrogen flow. The boiling isopropanol treatment is a critical step to achieve a high density yet separated array of holes, required for vacuum tube triode as well as SCLT. When the substrate is submerged in polystyrene solution, the charged polystyrene spheres are absorbed on the Au surface without aggregation due to the electrostatic repulsion force. The polystyrene spheres without the boiling isopropanol treatment shown in **Figure 6.4(d)** are easy to aggregate during the drying process and cause unwanted non-uniform and connected distribution.

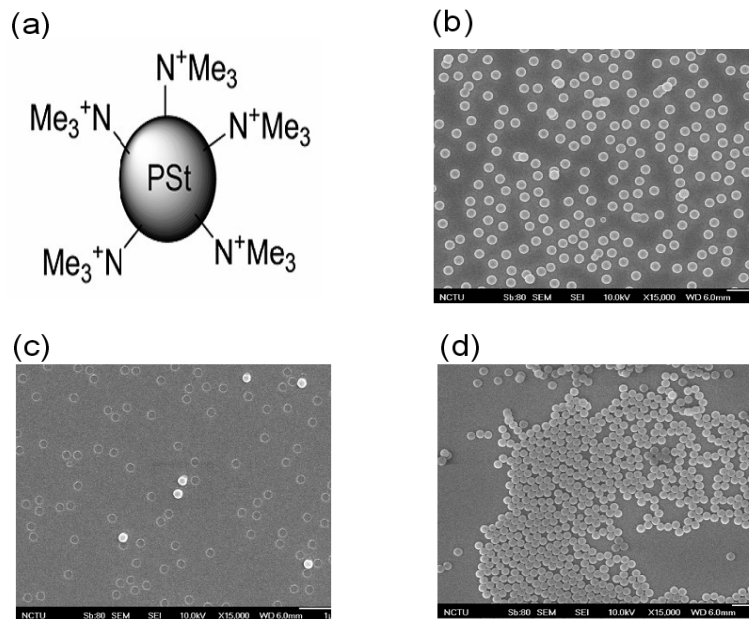


Figure 6.4 (a) The structure of polystyrene spheres. (b) The polystyrene spheres on the Au film surface. (c) The polystyrene spheres are removed by an adhesive tape (Scotch, 3M) without damage to the metal. (d) The gold surface without the boiling IPA treatment. (from ref. 15)

This may be attributed to the capillary force which pulls spheres into aggregates before the spheres are immobile during the period of vaporized solvent. The importance of the boiling isopropanol treatment is presumed to increase the evaporation rate of the solvent during the nitrogen blow dry such that the spheres do not have enough time to move to one another and form aggregate during evaporation. By tuning the solution concentration and submerging time, the condition to prepare Al grid with maximum opening density with minimum unwanted openings can be found in spite of some occurrence of the unwanted irregular openings. The benefit of this method is the possibility to process large areas in a short processing time without photolithography.

After immersed polystyrene spheres as shadow mask, the deposition is started at the pressure around 3×10^{-6} torr. Slower deposition rate is expected to obtain a smoother and better ordering of the insulator than fast one. The 50-nm-thick silicon oxide was deposited by thermal evaporation at a deposition rate of 0.1 \AA/s . It is

evaporated to prevent large leakage current from Al to Au. The insulator region was defined through shadow mask. Then we deposited aluminum as base metal. The deposition is started at the pressure around 5×10^{-6} torr. The 30-nm-thick Al was deposited by thermal evaporation at a deposition rate of $1 \text{ \AA}/\text{s}$.

In the section, we introduced each of the organic layer deposition respectively:

1. P3HT:

The substrate was exposed under the ultra-violet light for 15min to keep surface clean. P3HT was spin coated from chlorobenzene solution (2.5 wt% 1000rpm) on the Au layer, and baked at $200 \text{ }^\circ\text{C}$ for 10min in vacuum. After we spin coated the P3HT film, we use acetone to clean the unnecessary area. Then, a thin P3HT layer of about 1338 \AA was obtained.

2. Pentacene

The substrate was exposed under the ultra-violet light for 15min to keep surface clean. The pentacene material obtained from *Aldrich* without any purification. The deposition was started at the pressure around 3×10^{-6} torr. The 180-nm-thick pentacene was deposited by thermal evaporation at a deposition rate of $1 \text{ \AA}/\text{s}$. The active region was defined by shadow mask.

3. C60

The substrate was exposed under the ultra-violet light for 15min to keep surface clean. The deposition was started at the pressure around 3×10^{-6} torr. The 200-nm-thick C60 was deposited by thermal evaporation at a deposition rate of $1 \text{ \AA}/\text{s}$. The active region was defined by shadow mask.

Finally, Al was deposited as the top metal. The deposition was started at the pressure around 5×10^{-6} torr. The 50-nm-thick Al was deposited by thermal evaporation at a deposition rate of $1 \text{ \AA}/\text{s}$. The devices are encapsulated by glass cap with UV glue in a

glovebox, and measured in ambient condition.

6.3. Result and Discussions

6.3.1. Dielectric Characteristics

From **Figure 6.5(a)**, we can get the different breakdown voltage corresponding to different thickness of silicon oxide. When the operating voltage is 1V with thickness of bottom dielectric is 50 nm, the leakage current level is 10^{-3} mA/cm². When the operating voltage is 1V the leakage with thickness of top dielectric is 30 nm, the leakage current level is 10^{-2} to 10^{-3} mA/cm². The current of transistor can be low off depending on these measurement results.

Figure 6.5(b) shows that the leakage current of silicon oxide significantly increase after used Polystyrene spheres as mask. The reason is Polystyrene Spheres occupied the location of silicon oxide. It is inevitable in the process of Polystyrene Spheres.

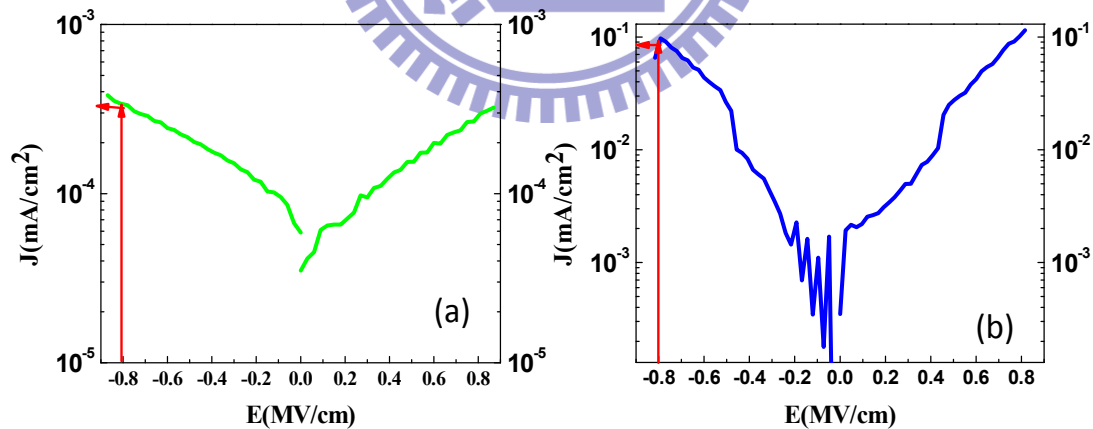


Figure 6.5 (a) The characteristics of silicon oxide with Polystyrene Spheres. (b) The characteristics of silicon oxide without Polystyrene Spheres.

6.3.2. Output Current Characteristics of SCLT

6.3.2.1. P3HT-based SCLT

P3HT-based SCLT was fabricated by steps according to chapter 2. The

characteristics of P3HT-based SCLT with opening diameters of 2000 Å on the top insulator (SIO) are shown in **Figure 6.6(a)**. In P3HT-based SCLT the carriers in the Al grid are blocked by the 30-nm silicon oxide and 14-nm P3HT between Al (base) and Al (collector). The grid current is the reverse current of the Al/SIO/P3HT/Al diode which is small but not zero. The current gain is therefore an crucial value to be maximized. As shown in **Figure 6.6(a)** and **Figure 6.6(b)**, the grid current density (J_G) of P3HT-based devices is in the order of 10^{-4} A which is much smaller than J_C . The current gain which is defined J_C/J_G is as large as 10^4 .

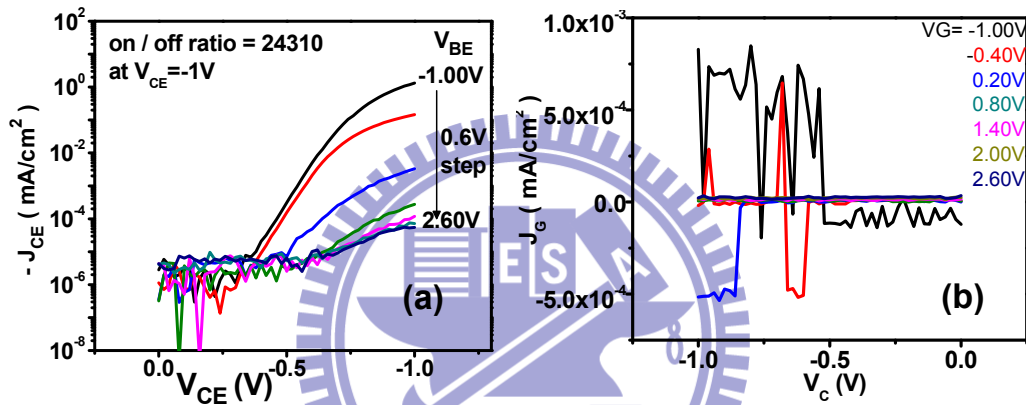


Figure 6.6 The electric characteristics of the P3HT-based SCLT with various grid voltages applied. The Au electrode is commonly grounded and the Al collector is negatively biased at V_C with respect to Au. The negative collector current I_C means the holes are collected by the Al collector and flows out from the transistor. The gate current I_G is no more than a few nA for all measurements. (a) The collector current as a function of the collector voltage varies by step V_G . (b) The grid current as a function of the collector voltage of the transistor.

For fixed collector voltage the collector current (J_C) is modulated by the grid voltage (V_G) and the Au (emitter) is the common ground. The positive V_G is used to introduce energy barrier for holes at the openings, and the off current can be reduced by increasing V_G until a large leakage current between the grid and collector occurs. **Figure 6.6(a)** shows the on/off ratio of J_C is 24310 at $V_C = -1$ V for transistors with opening diameters of 2000 Å on the top insulator and the highest J_C output is

1.331 mA/cm² in for device dimension of 1 mm². Note the total output current can be scaled up by using a larger area. In order to look for the signature of SCLC, the device characteristics in double logarithmic scale with fixed V_G are shown in the inset of **Figure 6.7**. Three regions belonging to ohmic, trap filling and SCLC can be distinguished.[16] The slope of $\log I - \log V$ is equal to 1 for ohmic conduction, while the slope is equal to 2 for SCLC. The dashed lines with slope equal to 1 and 2 are drawn in the inset of **Figure 6.7**. Indeed, the current follows the SCLC once the barrier at the opening is suppressed by a negative enough V_C . At low voltage there is always a small ohmic current. The polymer diode has a turn-on voltage where the current switches from a small leakage ohmic current into a quadratic SCLC current. The turn-on voltage is determined by both the level of the leakage and the difference between the work functions of the cathode and anode. **Figure 6.7** is shown the P3HT-based emitter-collector diode and the SCLC is about 3V.

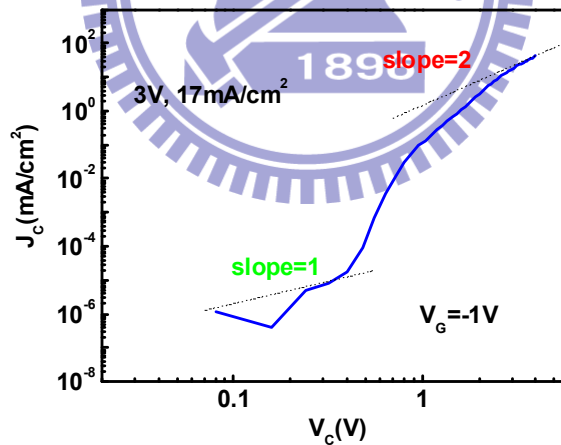


Figure 6.7 The electric characteristics of the P3HT-based SCLT in double logarithmic scale with fixed V_G .

6.3.2.2. Pentacene-based SCLT

Pentacene-based SCLT was fabricated by steps according to chapter 2. The characteristics of Pentacene-based SCLT with opening diameters of 2000 Å on the top

insulator are shown in **Figure 6.8(a)**. In Pentacene-based SCLT the carriers in the Al grid are blocked by the 30-nm silicon oxide and 60-nm Pentacene between Al (base) and Al (collector). The grid current is the reverse current of the Al/SiO/Pentacene/Al diode which is small but not zero. The current gain is therefore an crucial value to be maximized. As shown in **Figure 6.8(a)** and **Figure 6.8(b)**, the grid current density J_G of Pentacene-based devices is in the order of 10^{-3} A which is much smaller than J_C . The current gain which is defined J_C/J_G is as large as 10^3 . For fixed collector voltage the collector current (J_C) is modulated by the grid voltage (V_G) and the Au (emitter) is the common ground. The positive V_G is used to introduce energy barrier for holes at the openings, and the off current can be reduced by increasing V_G until a large leakage current between the grid and collector occurs.

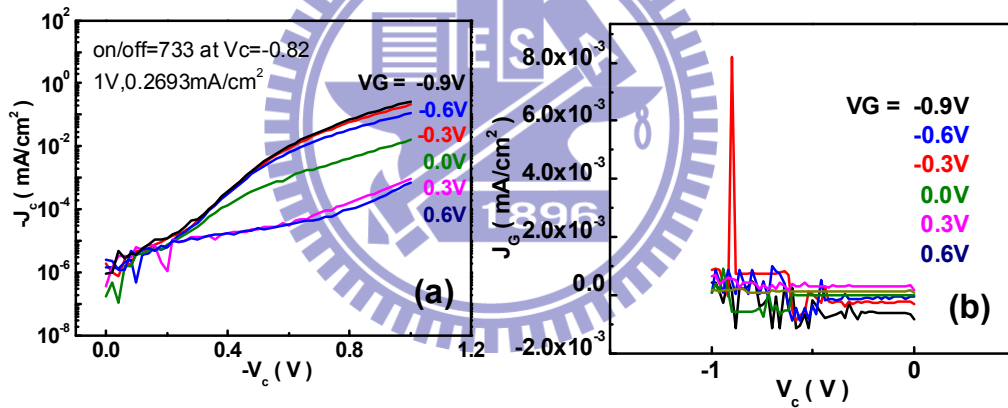


Figure 6.8 The electric characteristics of the Pentacene-based SCLT with various grid voltages applied. The Au electrode is commonly grounded and the Al collector is negatively biased at V_C with respect to Au. The negative collector current I_C means the holes are collected by the Al collector and flows out from the transistor. (a) The collector current as a function of the collector voltage varies by step V_G . (b) The grid current as a function of the collector voltage of the transistor.

Figure 6.8(a) shows the on/off ratio of J_C is 390 at $V_C = -1$ V for transistors with opening diameters of 2000 Å on the top insulator and the highest J_C output is 0.2693 mA/cm^2 for device dimension of 1 mm^2 . In order to look for the signature of SCLC, the device characteristics in double logarithmic scale with fixed V_G are shown

in the inset of **Figure 6.9**. The dashed lines with slope equal to 1 and 2 are drawn in the inset of **Figure 6.9** for indication.

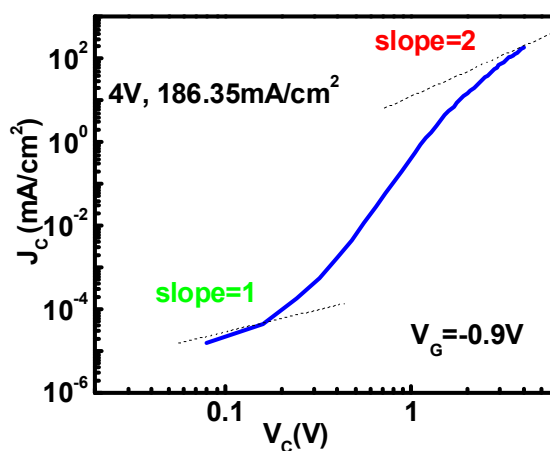


Figure 6.9 The electric characteristics of the Pentacene-based SCLT in double logarithmic scale with fixed V_G .

Indeed, the current follows the SCLC once the barrier at the opening is suppressed by a negative enough V_C . At low voltage there is always a small ohmic current. The polymer diode has a turn-on voltage where the current switches from a small leakage ohmic current into a quadratic SCLC current. The turn-on voltage is determined by both the level of the leakage and the difference between the work functions of the cathode and anode.

6.3.2.3. C60-based SCLT

C60-based SCLT was fabricated by steps according to chapter 2. The characteristics of C60-based SCLT with opening diameters of 2000 Å on the top insulator are shown in **Figure 6.10(a)**. In C60-based SCLT the carriers in the Al grid are blocked by the 30-nm silicon oxide and 80-nm C60 between Al (base) and Al (emitter). The grid current of Al/SiO/C60/Al diode is small but not zero. The current gain is therefore an crucial value to be maximized. As shown in **Figure 6.10(a)** and **Figure 6.10(b)**, the

grid current density (J_G) of C60-based devices is in the order of 10^{-3} which is smaller than J_C .

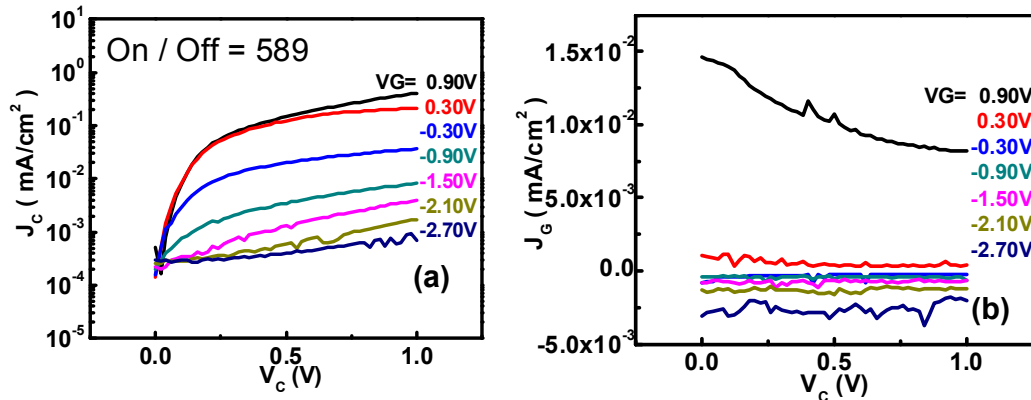


Figure 6.10 The electric characteristics of the C60-based SCLT with various grid voltages applied. The Al electrode is commonly grounded and the Au collector is positive biased at V_C with respect to Au. The collector current I_C means the electrons are collected by the Au collector. (a) The collector current as a function of the collector voltage various by step V_G . (b) The grid current as a function of the collector voltage of the transistor.

The current gain J_C/J_G is as 10^2 . For fixed collector voltage the collector current (J_C) is modulated by the grid voltage (V_G) and the Al (emitter) is the common ground. The negative V_G is used to introduce energy barrier for electrons at the openings, and the off current can be reduced by decreasing V_G . **Figure 6.10(a)** shows the on/off ratio of J_C is 589 at $V_C = 1$ V for transistors with opening diameters of 2000 Å on the top insulator and the highest J_C output is 0.411 mA/cm² for device dimension area of 1 mm². The total output current can be scaled up by using a larger area. In order to look for the signature of SCLC, the device characteristics in double logarithmic scale with fixed V_G are shown in the inset of **Figure 6.11**. The dashed lines with slope equal to 1 and 2 are drawn in the inset of **Figure 6.11** for indication.

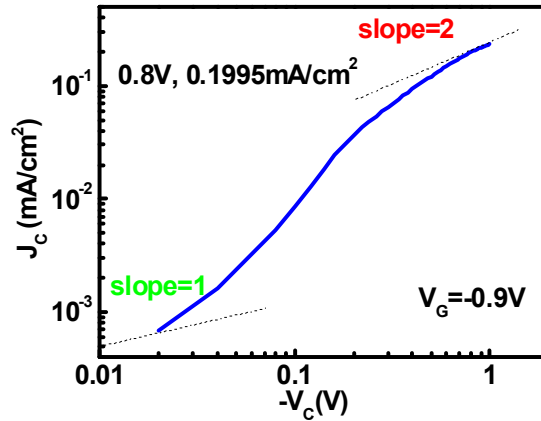


Figure 6.11 The electric characteristics of the C60-based SCLT in double logarithmic scale with fixed V_G .

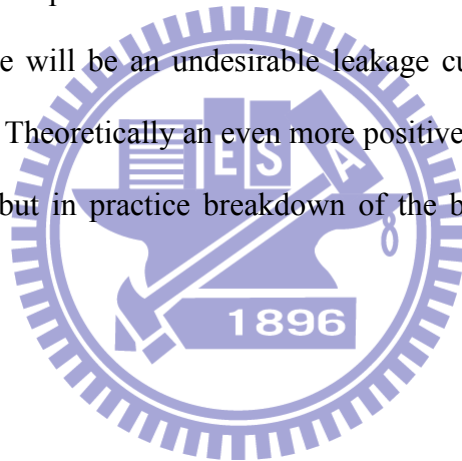
Indeed, the current follows the SCLC once the barrier at the opening is suppressed by a positive enough V_C . At low voltage there is always a small ohmic current. The polymer diode has a turn-on voltage where the current switches from a small leakage ohmic current into a quadratic SCLC current. The turn-on voltage is determined by both the level of the leakage and the difference between the work functions of the cathode and anode. Figure 3.6 is shown the P3HT-based emitter-collector diode and the SCLC is about 2V.

6.3.3. Operation Mechanism of SCLT

6.3.3.1. P3HT and Pentacene

The grid(base) control of the current can be further illustrated by looking at the spatial distribution of the current across the opening. For P3HT and pentacene, some region near the center of the opening has negative potential for holes to pass through. Near the edge the effect of the grid is so strong that a potential barrier forms despite of the negative potential of the collector. The current is therefore confined in an area controlled by the grid potential. As the transistor is in the on state, there is no barrier in all the area. The emitter-collector path through A position at the center and the path

through B position (**Figure 6.12(a)**) near the edge of the opening have the potential profiles as the curves (x) and (y) in **Figure 6.12(b)**, respectively. Assuming that the collector current is roughly a superposition of the currents of many small diodes given by the paths through different positions, the small diodes at position A contributing to a high current (A_{ON}) and those at position B are just about to be turned on (B_{ON}), as indicated in **Figure 6.12(c)**. On the other hand as the device is in the off state, the grid potential is positive and there is a potential barrier at the B position as the curve (z) in **Figure 6.12(b)**, and the small diodes there is reverse biased (B_{OFF}). As for A position, if it also has the potential profile like curve (z) in **Figure 6.12(b)**, the off current comes from small diodes at position A will be small. However, if the potential profile is as the curve (y), there will be an undesirable leakage current from the barely-on small diode at A (A_{OFF}). Theoretically an even more positive grid potential can always drive it into curve (z), but in practice breakdown of the base/SIO/organic/collector diode may happen first.



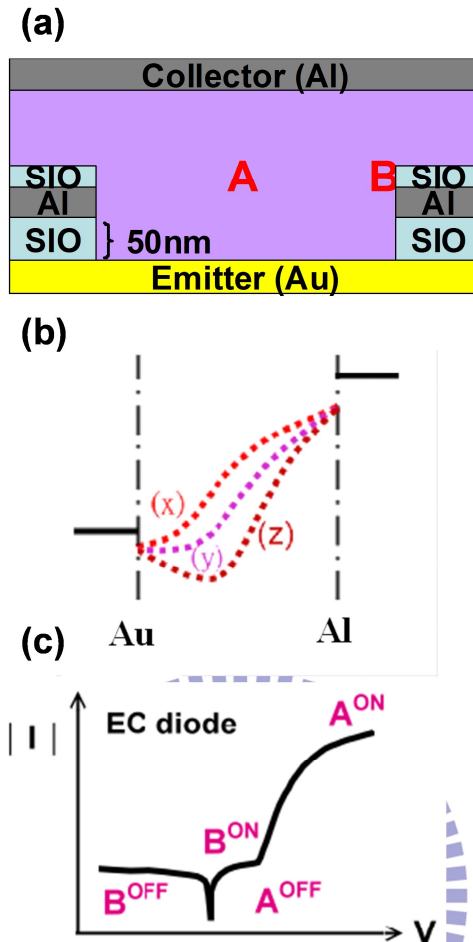


Figure 6.12 (a) The device structure near one opening of polymer SCLT. Position A is at the center of the opening, while position B is near the grid. (b) The potential profile along the emitter–collector path through the opening when V_C is fixed at a negative value. (x), (y), (z) are the potential profile along the path for various conditions. (c) The schematic current–voltage curve of EC diode with the structure Au/P-type/Al. The path through position A in on or off state are denote as A^{ON} or A^{OFF} in the diode IV curve. The state of the path through B is also shown. Because of the proximity to the positive biased grid B path can never be fully turned on as A.

6.3.3.2. C60

The grid control of the current can be further illustrated by looking at the spatial distribution of the current across the opening. For C60, some region near the center of the opening has positive potential for electrons to pass through. Near the edge the effect of the grid is so strong that a potential barrier forms despite of the positive potential of the collector. The current is therefore confined in an area controlled by

the grid potential. As the transistor is in the on state, there is no barrier in all the area. The emitter-collector path through A position at the center and the path through B position (**Figure 6.13(a)**) near the edge of the opening have the potential profiles as the curves (x) and (y) in **Figure 6.13(b)**, respectively. Assuming that the collector current is roughly a superposition of the currents of many small diodes given by the paths through different positions, the small diodes at position A contributing to a high current (A_{ON}) and those at position B are just about to be turned on (B_{ON}), as indicated in **Figure 6.13(c)**. On the other hand as the device is in the off state, the grid potential is negative and there is a potential barrier at the B position as the curve (z) in **Figure 6.13(b)**, and the small diodes there is reverse biased (B_{OFF}). As for A position, if it also has the potential profile like curve (z) in **Figure 6.13(b)**, the off current comes from small diodes at position A will be small. However, if the potential profile is as the curve (y), there will be an undesirable leakage current from the barely-on small diode at A (A_{OFF}). Theoretically an even more negative grid potential can always drive it into curve (z), but in practice breakdown of the base/SIO/C60/emitter diode may happen first.

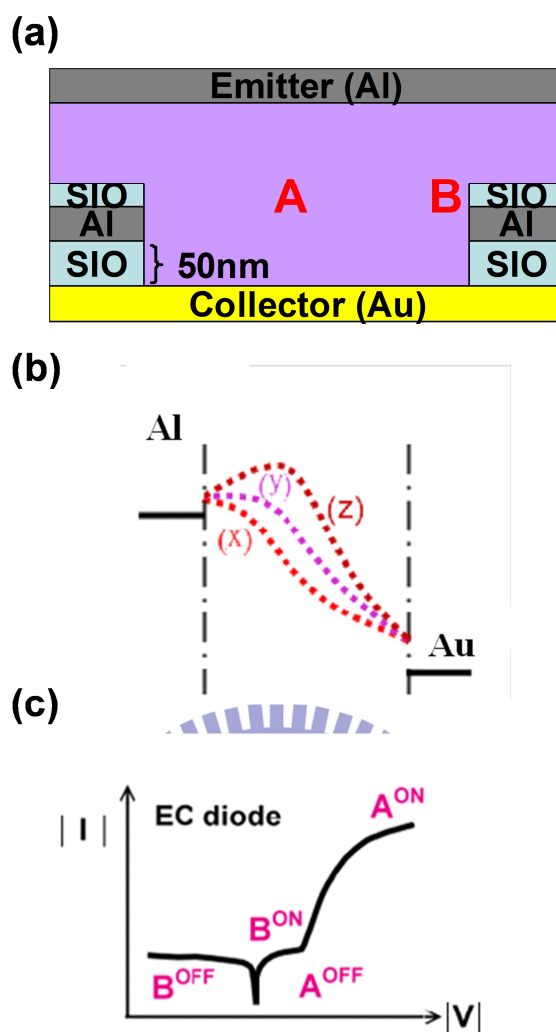


Figure 6.13 (a) The device structure near one opening of polymer SCLT. Position A is at the center of the opening, while position B is near the grid. (b) The potential profile along the emitter–collector path through the opening when V_C is fixed at a positive value. (x), (y), (z) are the potential profile along the path for various conditions. (c) The schematic current–voltage curve of EC diode with the structure Au/C60/Al. The path through position A in on or off state are denote as A^{ON} or A^{OFF} in the diode IV curve. The state of the path through B is also shown. Because of the proximity to the negative biased grid B path can never be fully turned on as A.

To improve output current, pentacene and fullerene (C60) are used to fabricate as SCLTs. The J - V curves for emitter-collector diodes with different organic materials are compared in **Figure 6.14**. Typical parameters are listed in **Table 6.1**. Pentacene and C60 provide higher output current than P3HT for SCLTs from Table 6.1. However, pentacene SCLTs and C60 SCLTs suffer from high leakage current even when base

leakage is as low as in P3HT SCLTs. New leakage phenomena are proposed and discussed.

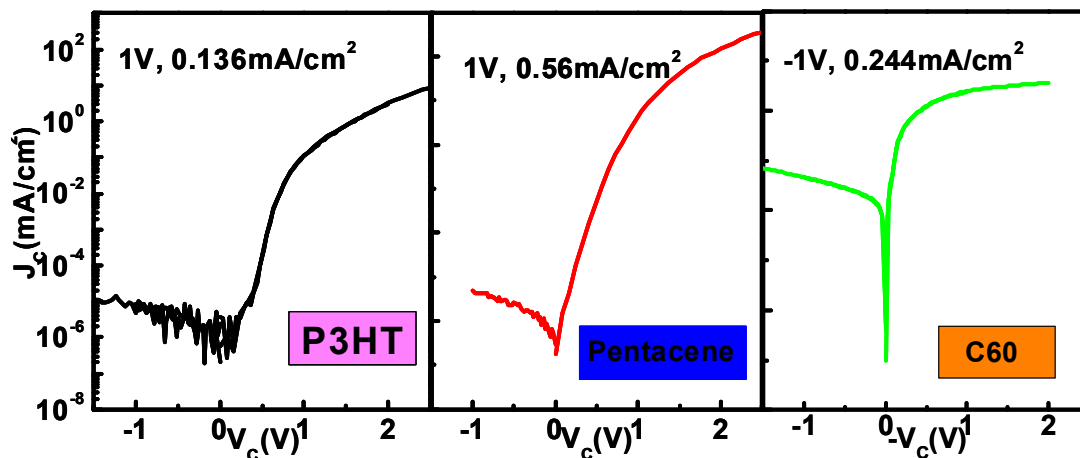


Figure 6.14 Current density – voltage curves for emitter–collector diodes made by P3HT, pentacene, and C60.

Table 6.1 Typical parameters of vertical transistors.

The characteristic of Emitter-Collector Diode			
	V(V)	J(mA/cm ²)	μ_{SCLC} (cm ² V ⁻¹ S ⁻¹)
P3HT	3	17	1.51E-5
Pentacene	4	186.35	2.27E-4
C60	0.8	0.1995	8.35E-6

Table 6.1 Typical parameters of vertical transistors.

6.3.4. Morphology Effect on Grid Structure

Leakage phenomenon is the morphology effect. AFM images of pentacene, C60, and P3HT above grid structure are compared in **Figure 6.15(a)**, **6.15(b)** and **6.15(c)**. Surface profile reveals that the grain structure in pentacene produces deep holes while

C60 and P3HT have rather smooth and dense morphology. Deep holes in pentacene make the top collector metal penetrates into pentacene film and shield the base electric field. As a result, base metal loses ability to turn off the channel.

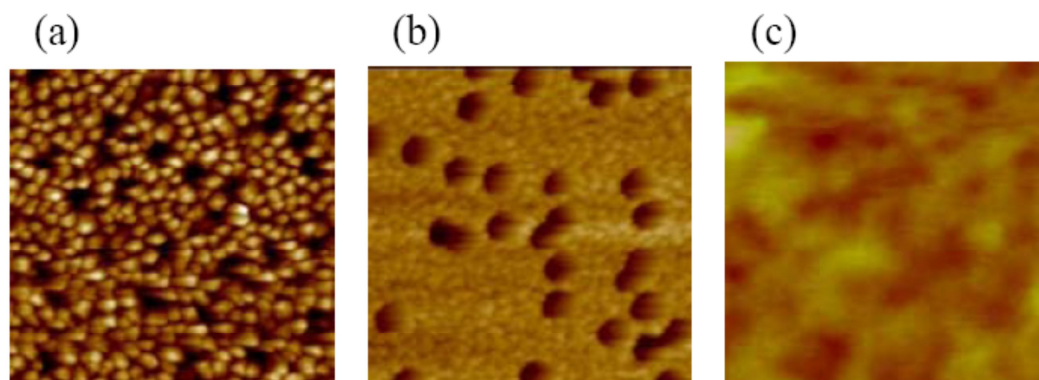


Figure 6.15 AFM images of (a) pentacene, (b) C60, and (c) P3HT above grid structure. The dimension of these images is $3\mu\text{m}\times 3\mu\text{m}$.

6.4. Conclusion

Low operation voltage is realized with space-charge-limited transistor (SCLT). A 1-V P3HT-based SCLT with high On/Off current ratio of 24310 is firstly demonstrated. From the experiment result, the morphology of the organic active layer on grid structure seriously influences the characteristics of SCLT. Also, the AFM images show that the grain structure of pentacene or C60 produces holes and leads to the leakage between collector and base. The developing of vertical transistor work was cooperating with Dr. Yu-Chiang Chao, Dr. Chun-Yu Chen, Shu-Ling Jiang, Chun-Ming Chiang, and Ming-Che Ku.

6.5. Future Work

In order to suppress the leakage, solution-processed materials is the best chose to the vertical transistor with grid structure. Recently, we use the nano-imprint technology to fabricate the grid structure and replace the polystyrene spheres fabrication process.

The related work is cooperating with *Prof. Lon A. Wang's Lab* in National Taiwan University. The process flow is shown in the **Figure 6.16**.

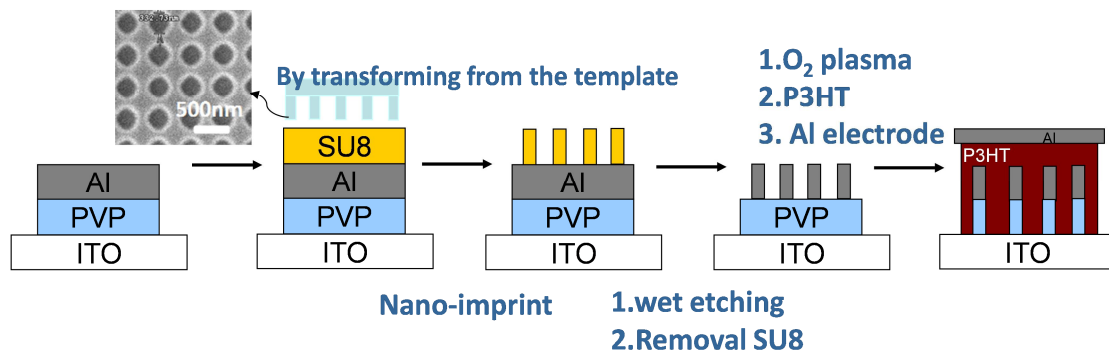


Figure 6.16 The process flow of SCLT by nano-imprint technology.

Figure 6.17 shows the fabrication processes of mold. The PDMS mold is made from *Prof. Lon A. Wang's Lab*.

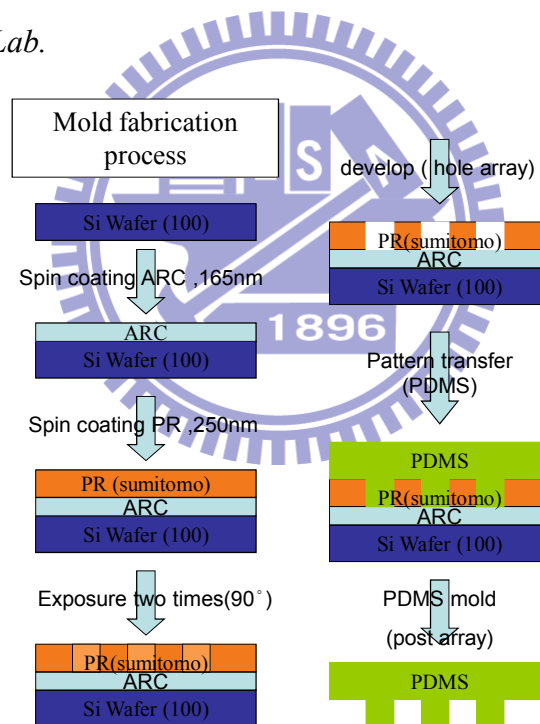


Figure 6.17 The process for developing the PDMS mold.

After developing the PDMS mold, it would imprint on the samples of (photoresist)PR/Al/PVP/ITO substrate. **Figure 6.18(a)** and **Figure 6.18(b)** shows the top view and cross sectional view SEM image of the sample after nano –imprint, respectively. From **Figure 6.18(a)**, we could clearly see the regular hole arrays from

up to down of the sample. However, we could still see the residual PR from **Figure 6.18(b)**.

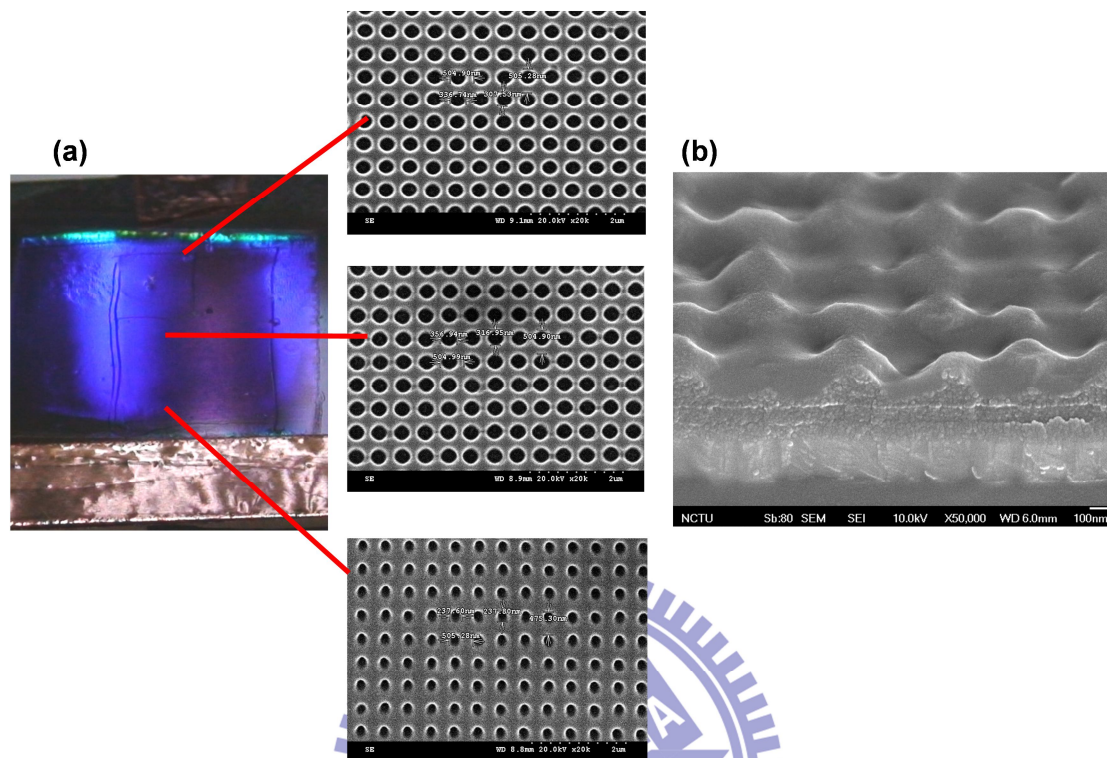


Figure 6.18 The (a) top view and (b) cross sectional view SEM images of the sample after nano-imprint.

Then, the plasma was utilized to etch the residual PR. During the plasma, the power was 150 W while the CF_4 and O_2 flow rate maintains at 25 and 6 sccm, respectively.

Figure 6.19 shows the different etching conditions of cross sectional view SEM images after plasma etching. The residual PR seems to disappear when the plasma etching time increases to 15 sec. However, the structure is seriously damaged when the plasma etching time increases to 50 sec, therefore, the 15 sec plasma etching condition is chosen.

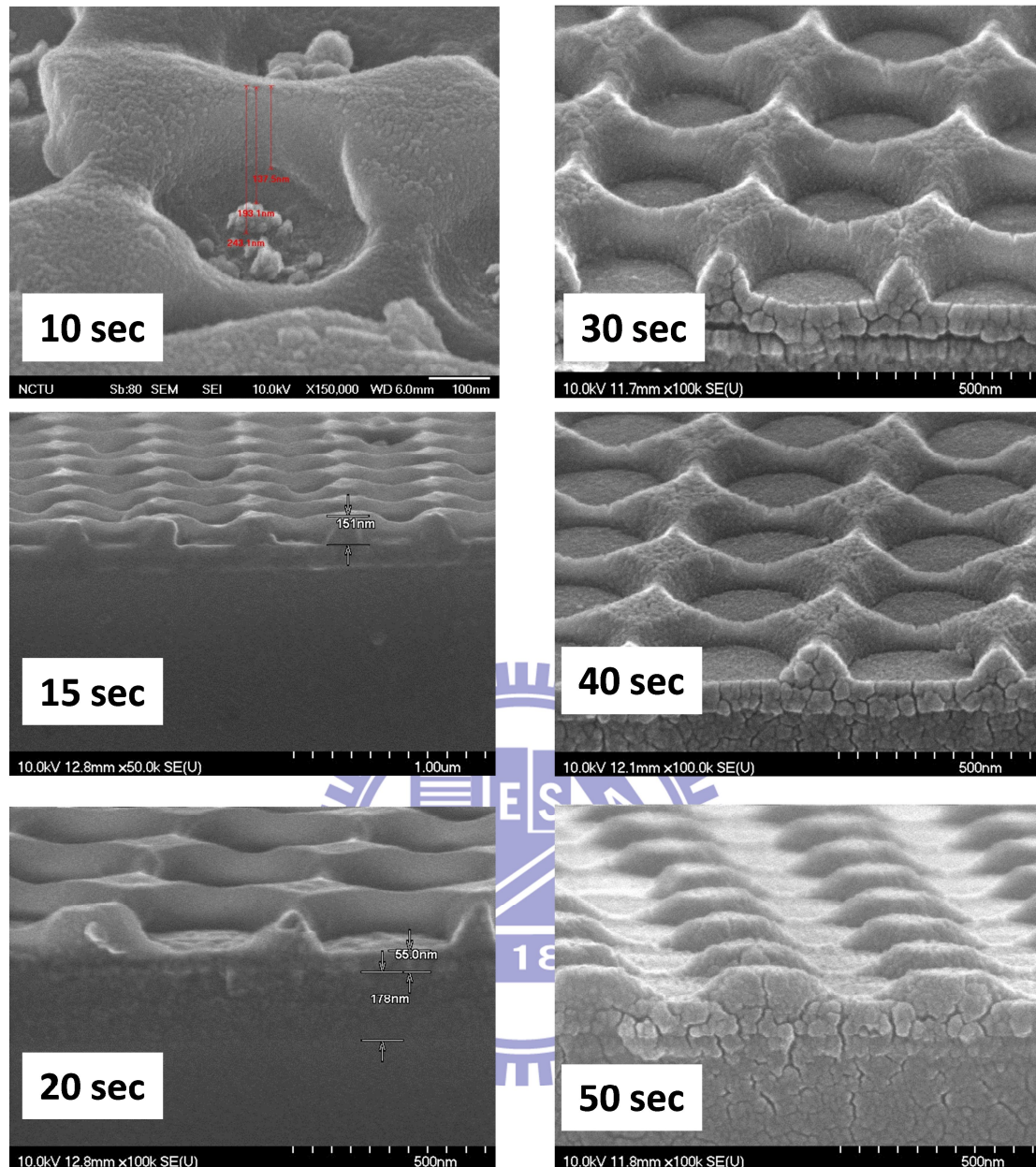


Figure 6.19 The different plasma etching conditions of cross sectional view SEM images.

Next, we utilized the wet etching process to etch the Al without PR coverage sites. The wet etching solution is mixed of H_3PO_4 : HNO_3 : CH_3COOH : H_2O with the ratio as 50:1:14:7. The wet etching conditions is 20, 40, 60 sec. **Figure 6.20** shows the cross sectional view SEM images of different etching time. From the result of wet etching, the Al seems to be removed when the etching time increases to 40 sec. Finally, the oxygen plasma was used to remove the PVP without Al coverage sites. During the

plasma, the power and chamber pressure were 150 W and 3 mtorr while the oxygen flow rate maintains at 40 sccm, respectively. Figure 3.21(d) shows the sample after oxygen plasma etching. From the result, it didn't create well regular opening because of the wet etching time is not enough and still have residual Al on the PVP surface. Therefore, we would increase the wet etching time and have the best condition.

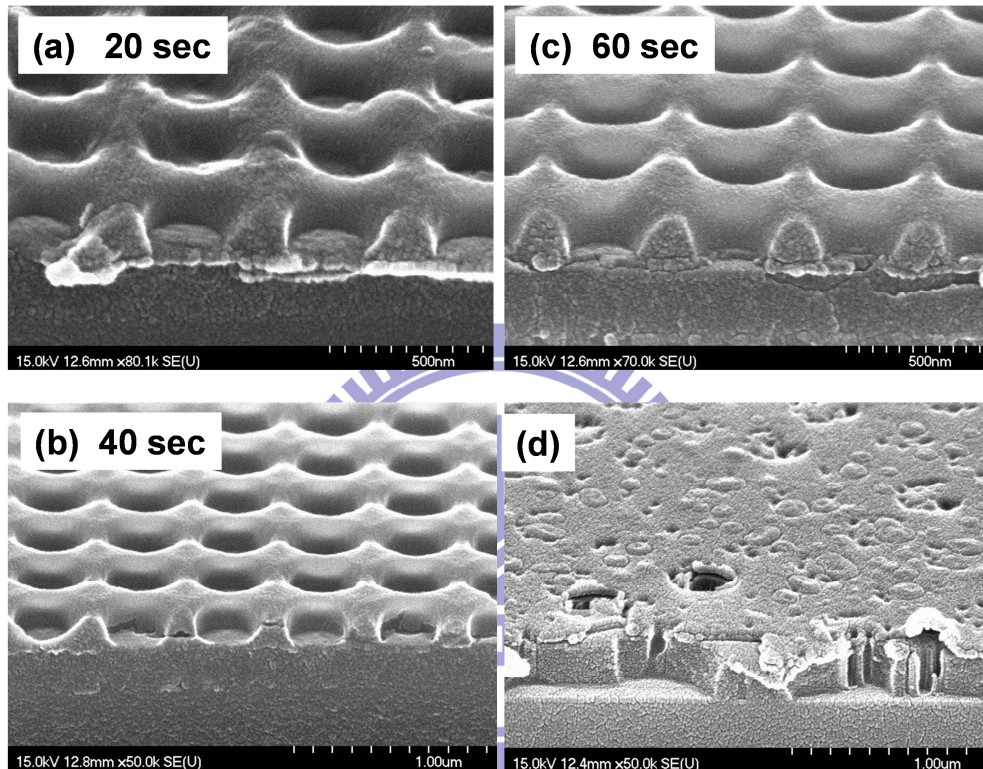


Figure 6.20 (a), (b), (c) shows the cross sectional view SEM images of different wet etching conditions of sample. (d) is the sample cross sectional view SEM images after plasma etching.

References

- [1] W. Shockley, "Transistor electronics: Imperfections, unipolar and analog transistors" *Proc. IRE* 40, 1289, (1952).
- [2] S. A. Roosild, R. P. Dolan, and D. O'Neil, "A unipolar structure applying lateral diffusion" *Proc. IEEE* 51, 1059, (1963).
- [3] K. Kudo, D. X. Wang, M. Iizuka, S. Kuniyoshi, and K. Tanaka, "Schottky gate static induction transistor using copper phthalocyanine films" *Thin Solid Films*

- 331, 51, (1998).
- [4] Y. Yang and A. J. Heeger, "A new architecture for polymer transistors" *Nature* 372, 344, (1994).
- [5] K. Fujimoto, T. Hiroi, and M. Nakamura, "Organic static induction transistors with nano-hole arrays fabricated by colloidal lithography" *e-J. Surf. Sci. Nanotechnol* 3, 327, (2005).
- [6] Y. C. Chao, H. F. Meng, S. F. Horng, and C. S. Hsu, "High-performance solution-processed polymer space-charge-limited transistor" *Org. Electron.* 9, 310, (2008).
- [7] T. Someya, Y. Kato, T. Sekitani, S. Iba, Y. Noguchi, Y. Murase, H. Kawaguchi, and T. Sakurai, "Conformable, flexible, large-area networks of pressure and thermal sensors with organic transistor active matrixes" *Proc. Natl. Acad. Sci. U.S.A.* 102, 12321, (2005).
- [8] L. Ma and Y. Yang, "Unique architecture and concept for high-performance organic transistors" *Appl. Phys. Lett.* 85, 5084, (2004).
- [9] Y. C. Chao, M. H. Xie, M. Z. Dai, H. F. Meng, S. F. Horng, and C. S. Hsu, "Polymer hot carrier transistor with low bandgap emitter", *Appl. Phys. Lett.* 92, 093310, (2008).
- [10] S. S. Cheng, Y. C. Chuang, K. Dhananjay, C. W. Ou, M. C. Wu, C. W. Chu, "Organic Base Modulation Triodes and Their Inverters on Flexible Substrates" *Adv. Mater.* 21, 1860, (2009).
- [11] Y. C. Chao, H. F. Meng, and S. F. Horng, "Polymer space-charge-limited transistor" *Appl. Phys. Lett.* 88, 223510, (2006).
- [12] K. Fujimoto, T. Hiroi, K. Kudo, M. Nakamura, "High-performance vertical-type organic transistors with built-in nanotriode arrays" *Adv. Mater.* 19, 525, (2007).
- [13] K. Sethuraman, S. Ochiai, K. Kojima, and T. Mizutani, "Performance of

poly(3-hexylthiophene) organic field-effect transistors on cross-linked poly(4-vinyl phenol) dielectric layer and solvent effects” *Appl. Phys. Lett.* 92, 183302, (2008).

[14] M. Pope, H. P. Kallmann, and P. Magnante, “Electroluminescence in organic crystals” *J. Chem. Phys.* 38, 2042-2043, (1963).

[15] C. W Tang and S. A. Vanslyke, “Degradation mechanism of small-based organic light-emitting devices” *Science* 283, 1900-1902, (1999).

[16] Z. Chiguarve and V. Dyakonov, “Trap-limited hole mobility in semiconducting poly(3-hexylthiophene)” *Phys. Rev. B* 70, 235207, (2007).



Chapter 7. Summary and Future Work

In this dissertation, the high performance a-IGZO TFT with nano dot doping and the high performance organic (polymer) solution-processed vertical transistors are investigated. Also, the application for organic devices such as photodetector (photodiode and phototransistor) and ammonia gas sensor are also investigated.

For Effective Mobility Enhancement by Using Nanometer Dot Doping in amorphous IGZO Thin-Film Transistors: (*Advanced Materials*, 2011)

In **Chapter 2**, we propose a top-gate self-aligned a-IGZO TFT with nano-meter-scale dotted channel doping. With a simple, low-cost, and lithography-free process, the effective mobility level of TG a-IGZO TFT becomes 19 times higher than that of the control sample and the maximum effective mobility reaches $79 \text{ cm}^2 \text{ V}^{-1} \text{ s}^{-1}$. If the effective intrinsic channel length is used to estimate the mobility inside the intrinsic a-IGZO region, the maximum intrinsic mobility of TG a-IGZO TFT reaches $39.6 \text{ cm}^2 \text{ V}^{-1} \text{ s}^{-1}$ and increases 10 times than controls (STD). The nano dot doping (NDD) structure reduces the effective channel length and lowers the potential barrier in the intrinsic a-IGZO by the neighboring high conductive regions. Increasing the dot concentration leads to a more pronounced barrier lowering effect. According to the percolation conduction model, the decrease of the potential barrier leads to a significant increase of the field-effect mobility in a-IGZO semiconductor. The high mobility and the self-aligned structure of the proposed a-IGZO TFTs with NDD are promising for the development of low cost circuit-like RFID tags, smart cards, and transparent circuits on windows. **Figure 7.1** shows the context for **Chapter 2**.

To improve the reproducibility and the uniformity, an ordered dot-like structure is

required. Nano imprint may be utilized to produce the ordered nano-scale dot-like structure in future works.

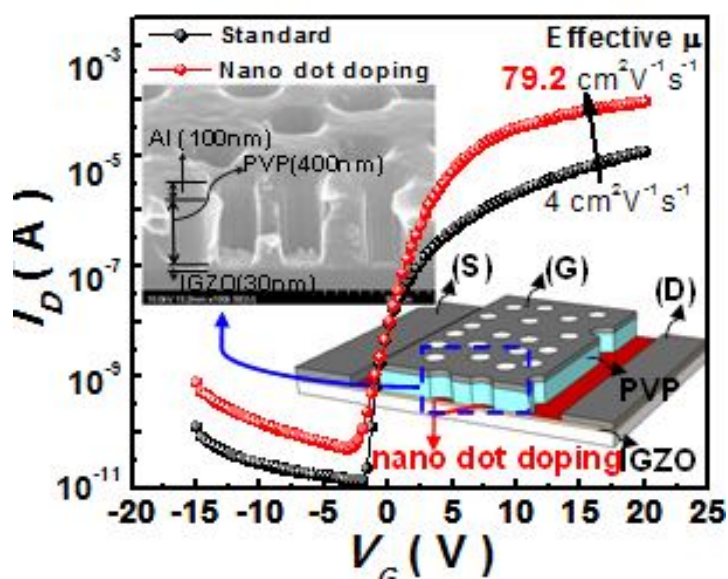


Figure 7.1 The transfer characteristics of TG-STD and TG-NDD. The device structure of TG-NDD and the SEM image of channel region are shown in the inset of Figure 7.1.

For Increasing Organic Vertical Carrier Mobility for the Application of High Speed Bilayered Organic Photodetector: (*Applied Physics Letters*, 2009)

In **Chapter 3**, we report a direct influence of the vertical carrier mobility on the response speed of organic PDs. By using C60 as the acceptor material and pentacene with high deposition rate as the donor material, a high-speed bilayered organic PD is demonstrated for the detection of very-high-frequency (VHF, > 30MHz) light switching signals. The influence of deposition rate on the vertical hole mobility of pentacene on PEDOT:PSS is investigated and explained. The VHF organic PDs facilitate the development of the next-generation information technologies. **Figure 7.2** shows the context for **Chapter 3**.

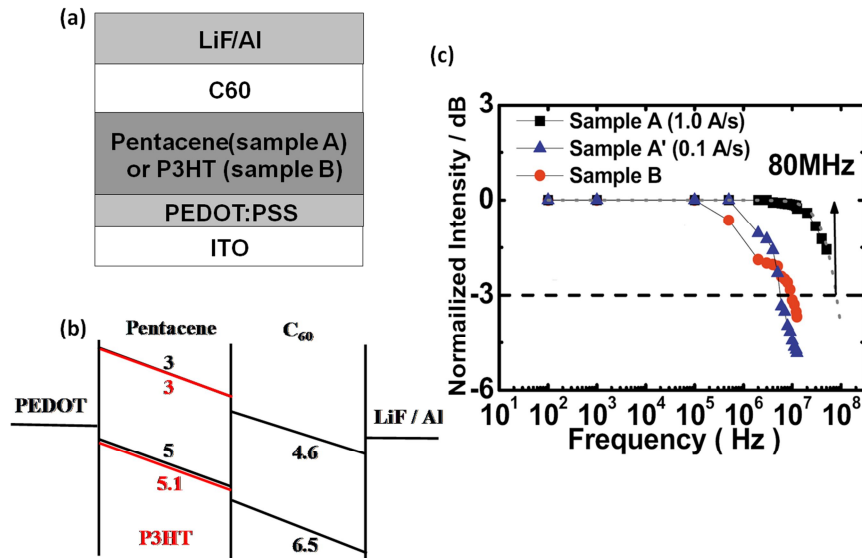


Figure 7.2 Context for Chapter 3. (a) The structure of bilayer photodiode. (b) The band diagram for photodiode under reverse biased voltage. (c) The frequency characteristics of PDs made by pentacene and P3HT.

For Vertical Polymer Phototransistor featuring Photomultiplication due to Base-field Shielding: (*Applied Physics Letters*, 2011)

In **Chapter 4**, we demonstrated a vertical polymer phototransistor, based on the space-charge limited transistor (SCLT). The photoresponse in SCLT was governed by the following steps. First, the SCLT was operated in the *off*-state to provide a current in total darkness. The EC diode was forward biased and the base potential created a potential barrier to impede hole transport. Second, under illumination, excitons were generated in the polymer channel layer. In this study, the channel material was P3HT blended with PCBM at a blending ratio of 1:0.1, to enhance exciton dissociation. Third, after exciton dissociation, electrons flowed toward the base electrode. Electrons accumulated around the base electrode shield of the base field. As a result, the potential barrier was reduced. At the same time, the hole injection from ITO into the channel is enhanced. Finally, with the reduction in the potential barrier and the enhancement of hole injection, a large photocurrent was obtained. **Figure 7.3** shows

the context for **Chapter 4**. In future studies, incorporating more PCBM into P3HT may succeed in enhancing the speed of the base-field shielding, while an electron blocking layer between the collector (aluminum) and active layer would be required to prevent leakage through PCBM.

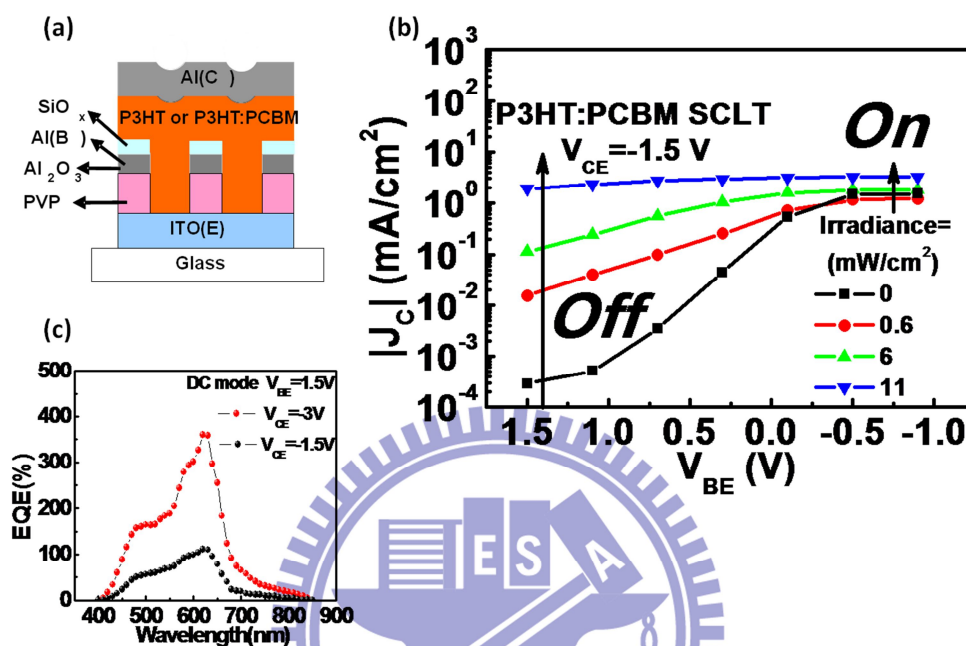


Figure 7.3 Context for Chapter 4. (a) The structure of phototransistor. (b) Transfer characteristics of a P3HT:PCBM SCLT in total darkness and under illumination. The light intensity is from 0 to 11 mW/cm². (c) The EQE of P3HT:PCBM-SCLT.

For Pentacene-based Organic Thin Film Transistors for Ammonia Sensing: (*IEEE Sensors Journal*, 2011)

In **Chapter 5**, high sensitivity ammonia gas sensor is firstly demonstrated by pentacene-based thin film transistor. A pentacene-based OTFT is shown to be highly sensitive for ammonia sensing from 0.5 to 5 ppm, a critical range for the diagnosis of patients with chronic liver diseases and renal failure. This demonstrated that OTFT devices, which can be fabricated by simple and cheap process and exhibited channel length and width as large as several hundreds of microns, are useful as non-invasive biomedical sensors. This is on the contrary to inorganic MOSFET devices that require high fabrication cost and complicated fabrication process and the dimension of the

devices has to be scaled down to the range of nanometers to increase the gas sensing sensitivity. The sensitivity and selectivity of OTFTs as gas sensor can be further improved by the modification of the PMMA dielectric layer, selecting suitable measuring parameters and providing additional local electric field. Due to the simple fabrication processes of the devices, OTFTs are promising to be developed to a portable and disposable gas sensor. **Figure 7.4** shows the context for **Chapter 5**. In the future study, we would change the insulator layer from PMMA to PVP and increase the sensitivity. It is because that we could adjust the OH functional end groups from the ratio between PVP and PMF.

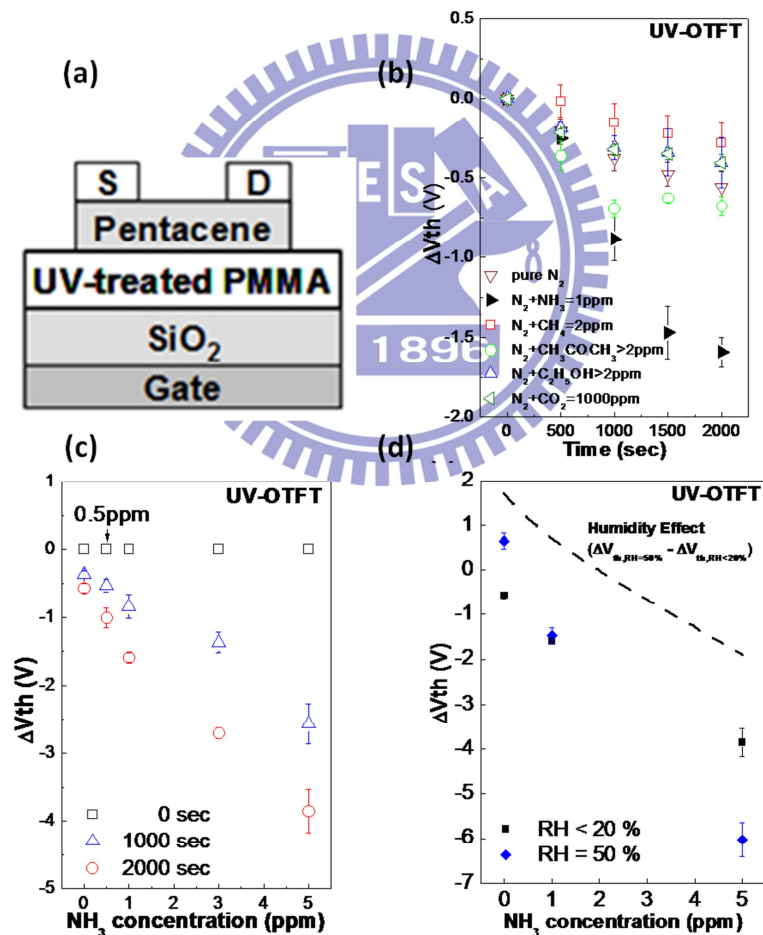


Figure 7.4 Context for Chapter 5. (a) The structure of UV-OTFT. (b) UV-OTFTs were used to determine the variations of ΔV_{th} as a function of sensing time. Ammonia (NH₃), carbon dioxide (CO₂), alcohol (C₂H₅OH), methane (CH₄), and acetone (CH₃COCH₃) were introduced individually into the sensing chamber with 1 atm N₂. (c) Concentration

dependent ammonia sensing response of UV-OTFT. (d) Humidity effect on ammonia sensing using UV-OTFT devices.

For Low Operated Polymer Vertical Transistors with High On/Off Current Ratio: (*IEEE International Electron Device Meeting, 2009*)

In **Chapter 6**, we demonstrated a low operation solution-processed vertical transistor with high on/off current ratio. A 1-V P3HT-based SCLT with high On/Off current ratio of 24310 is firstly demonstrated. From the experiment result, the morphology of the organic active layer on grid structure seriously influences the characteristics of SCLT. Also, the AFM images show that the grain structure of pentacene or C60 produces holes and leads to the leakage between collector and base. In order to suppress the leakage, solution-processed materials is the best chose to the vertical transistor with grid structure.

In the future, we will use the nano-imprint technology to fabricate the grid structure and replace the polystyrene spheres (PS) fabrication process to avoid the accumulation of PS. The related work is cooperating with *Prof. Lon A. Wang's Lab* in National Taiwan University. **Figure 7.5** shows the context for **Chapter 6**.

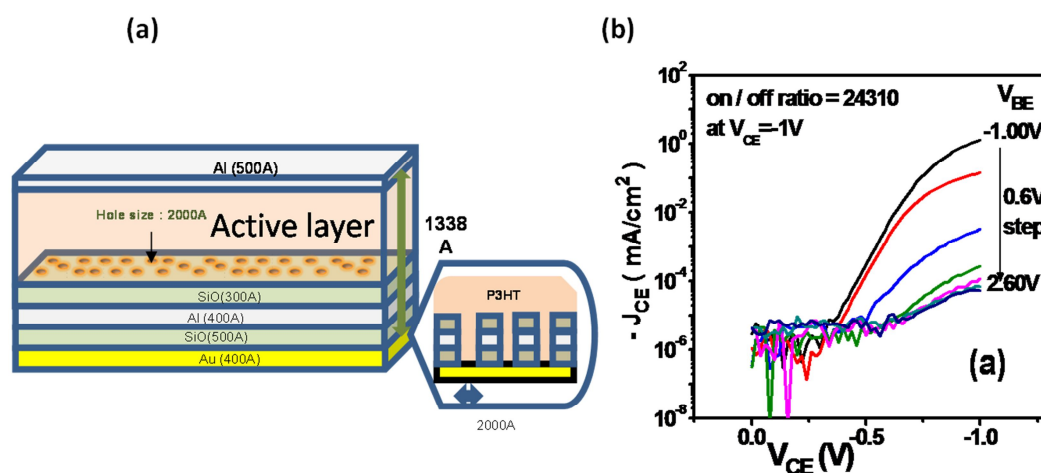


Figure 7.5 Context for Chapter 6. (a)The structure of proposed vertical transistor, (b) the output characteristics of P3HT-based vertical transistor.

Vita

姓名：蔡武衛 (Wu-Wei Tsai)

性別：男

出生日期：1983 年 12 月 29 日

出生地：桃園縣

地址：桃園縣平鎮市廣泰路 201 巷 28 弄 2 號

學歷：

私立長庚大學電子工程學系 (2002 年 9 月~2006 年 6 月)

國立交通大學顯示科技所碩士班 (2006 年 9 月~2007 年 9 月) (逕博)

國立交通大學光電工程所博士班 (2007 年 9 月~2011 年 11 月)

論文題目：

(中文) 低溫氧化物半導體及有機半導體之電晶體及感測器研究

(英文) **Low Temperature Transistors and Sensors based on Oxide Semiconductor and Organic Semiconductor Materials**

Publication lists

Journal:

- [1] Wu-Wei Tsai, Yu-Chiang Chao, En-Chen Chen, Hsiao, Wen Zan*, Hsin-Fei Meng *, and Chain-Shu Hsu, “Increasing organic vertical carrier mobility for the application of high speed bilayered organic photodetector” Appl. Phys. Lett. 95, 213308 (2009).
- [2] Yu-Chiang Chao, Ming-Che Ku, Wu-Wei Tsai, Hsiao-Wen Zan*, Hsin-Fei Meng*, Hung-Kuo Tsai, and Sheng-Fu Horng, “Polymer space-charge-limited transistor as a solid-state vacuum tube triode” Appl. Phys. Lett. 97, 223307 (2010).
- [3] Hsiao-Wen Zan, Wu-Wei Tsai, Yuan-Ren Lo, Yu-Mei Wu, and Yuh-Shyong Yang*, “Pentacene-based organic thin film transistors for ammonia sensing”, accepted by IEEE Sensors Journal, (2011).
- [4] Hsiao-Wen Zan*, Wu-Wei Tsai, Chia-Hsin-Chen, and Chuang-Chuang Tsai, “Effective mobility enhancement by using nanometer dot doping in amorphous IGZO thin-film transistors” accepted by Advanced Materials (2011).
- [5] Hsiao-Wen Zan*, Wu-Wei Tsai, and Hsin-Fei Meng, “Vertical polymer phototransistor featuring photomultiplication due to base-field shielding”, Appl. Phys. Lett. 98, 053305 (2011).

International Conference:

- [1] Kuo-Hsi Yen, Wen-Xin Wu, Wu-Wei Tsai and Hsiao-Wen Zan,

“Pentacene-based organic thin film transistor on ammonia (NH₃) Sensing,” Optics and Photonics Taiwan (OPT), (2007).

[2] Kuo-Hsi Yen, Ruei-Chih Yan, **Wu-Wei Tsai** and Hsiao-Wen Zan, “UV-enhanced photo responsivity on PMMA-OTFTs,” Optics and Photonics Taiwan (OPT), (2007).

[3] Hsiao-Wen Zan, **Wu-Wei Tsai**, Yu-Mei Wu, Kuo-Hsi Yen, Yen-Ren Lo, and Yuh-Shyong Yang, “Enhanced ammonia(NH₃) sensing response of UV-light treated OTFTs”, ECS Transactions (2008).

[4] Yu-Chiang Chao, **Wu-Wei Tsai**, Chun-Yu Cheng, Hsiao-Wen Zan*, Hsin-Fei Meng*, Shu-Ling Jiang, Chun-Ming Chiang, and Ming-Che Ku "A 1-V Operated Polymer Vertical Transistor with High On/Off Current Ratio", IEEE International Electron Device Meeting (IEDM) (2009).

[5] Hsiao-Wen Zan, **Wu-Wei Tsai**, Yu-Mei Wu, Yuan-Ren Lo and Yuh-Shyong Yang, “UV-treated organic thin- film transistors (OTFTs) for ammonia (NH₃) gas sensing”, SNTD, (2009).

[6] Hsiao-Wen Zan*, Hsiu-Wen Hsueh, Shih-Chin Kao, Wei-Tsung Chen, Meng-Che Ku, **Wu-Wei Tsai**, Hsin-Fei Meng and C. C. Tsai, “New Polymer-Capped a-IGZO TFT with High Sensitivity to Visible Light for the Development of Integrated Touch Sensor Array”, SID, (2010).

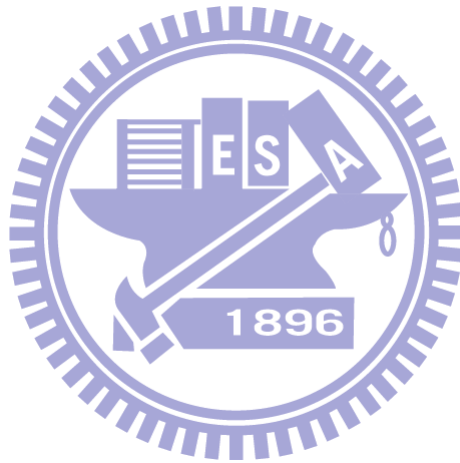
[7]**Wu-Wei Tsai**, Hsiao-Wen Zan, Chia-Hsin Chen, Chuang-Chuang Tsai, and Hsin-Fei Meng, “High Mobility a-IGZO TFT with Nano-Dots Doping”, IDMC, (2011) (Best Student Poster Award)

[8] Hsiao-Wen Zan*, **Wu-Wei Tsai**, Chia-Hsin Chen, Chuang-Chuang Tsai, and Hsin-Fei Meng, “High Performance a-IGZO TFT with Nano-Dots Doping”, SID, (2011).

[9] **Wu-Wei Tsai**, Hsiao-Wen Zan, Chia-Hsin Chen, Chuang-Chuang Tsai,

and Hsin-Fei Meng, “High Performance a-IGZO TFT with Nano-Dots Doping”, IEEE INEC, (2011).

[10] **Wu-Wei Tsai**, Hsiao-Wen Zan, Chia-Hsin Chen, Chuang-Chuang Tsai, and Hsin-Fei Meng, “High Mobility a-IGZO TFT with Nano-Dots Doping”, ICANS 24 (2011)



Patents

[1] Taiwan patent. 冉曉雯，孟心飛，蔡武衛，趙宇強，垂直式光電元件及其製法，專利申請中，100108872 中華民國. 發明專利, (pending).

[2] US patent. Hsiao-Wen Zan, Hsin-Fei Meng, Wu-Wei Tsai, and Yu-Chiang Chao, VERTICAL ELECTRO-OPTICAL COMPONENT AND METHOD OF FABRICATING THE SAME, US Patent Number: 13/111,205, United States, Type: Invention, (pending).

[3] Taiwan patent. 冉曉雯，蔡娟娟，孟心飛，蔡武衛，陳家新，具有電晶體的半導體元件及其製法，專利申請中，100106145 中華民國. 發明專利, (pending).

[4] PRC patent. 冉曉雯，蔡娟娟，孟心飛，蔡武衛，陳家新，具有電晶體的半導體元件及其製法，專利申請中：201110097385.4 中華人民共和國. 發明專利, (pending).

[5] KR patent. Hsiao-Wen Zan, Chuang-Chuang Tsai, Hsin-Fei Meng, Wu-Wei Tsai, and Chia-Hsin Chen, SEMICONDUCTOR COMPONENT HAVING A TRANSISTOR AND METHOD OF FABRICATING THE SAME, KR Patent Number: 10-2011-0041644, Republic of Korea, Type: Invention, (pending).